



U.S. Department of
Transportation

**Federal Railroad
Administration**

Tank Car Reliability Design and Analysis

Office of Research
and Development
Washington, DC 20590

NOTICE

This document is disseminated under the sponsorship of the Department of Transportation in the interest of information exchange. The United States Government assumes no liability for its contents or use thereof.

NOTICE

The United States Government does not endorse products or manufacturers. Trade or manufacturers' names appear herein solely because they are considered essential to the objective of this report.

REPORT DOCUMENTATION PAGE			<i>Form Approved</i> <i>OMB No. 0704-0188</i>
Public reporting burden for this collection of information is estimated to average 1 hour per response, including the time for reviewing instructions, searching existing data sources, gathering and maintaining the data needed, and completing and reviewing the collection of information. Send comments regarding this burden estimate or any other aspect of this collection of information, including suggestions for reducing this burden, to Washington Headquarters Services, Directorate for Information Operations and Reports, 1215 Jefferson Davis Highway, Suite 1204, Arlington, VA 22202-4302, and to the Office of Management and Budget, Paperwork Reduction Project (0704-0188), Washington, DC 20503.			
1. AGENCY USE ONLY (Leave blank)	2. REPORT DATE March 2007	3. REPORT TYPE AND DATES COVERED	
4. TITLE AND SUBTITLE Tank Car Reliability Design and Analysis		5. FUNDING NUMBERS	
6. AUTHOR(S) David Pecknold, Huseyin Sehitoglu, Christopher P.L. Barkan, Sandeep Kibey, One-Chul Lee			
7. PERFORMING ORGANIZATION NAME(S) AND ADDRESS(ES) University of Illinois at Urbana-Champaign Department of Civil and Environmental Engineering 205 N. Mathews Urbana, IL 61801		8. PERFORMING ORGANIZATION REPORT NUMBER	
9. SPONSORING/MONITORING AGENCY NAME(S) AND ADDRESS(ES) U.S. Department of Transportation Federal Railroad Administration Office of Research and Development Washington, DC 20590		10. SPONSORING/MONITORING AGENCY REPORT NUMBER DOT/FRA/ORD-07/05	
11. SUPPLEMENTARY NOTES COTR: Francisco Gonzalez			
12a. DISTRIBUTION/AVAILABILITY STATEMENT This document is available to the public through the National Technical Information Service, Springfield, VA 22161.		12b. DISTRIBUTION CODE	
13. ABSTRACT (Maximum 200 words) This report presents the results of the Federal Railroad Administration project DTFR DV-00-G-60019 (Tank Car Reliability Design and Analysis), carried out in the Department of Civil and Environmental Engineering and the Department of Mechanical and Industrial Engineering at the University of Illinois at Urbana-Champaign. The overall objective of the project was to propose and develop new and improved rational procedures for assessing the structural integrity of stub sill tank cars, in order to provide higher levels of assurance against the occurrence of structural failure of a car that could lead to an accident. This research specifically focuses on procedures for establishing safe inspection intervals to detect the presence of fatigue cracks in the stub sill assembly before they grow to critical size.			
14. SUBJECT TERMS Tank car, stub sill, fatigue crack growth, damage tolerance analysis, finite element analysis		15. NUMBER OF PAGES 100	
		16. PRICE CODE	
17. SECURITY CLASSIFICATION OF REPORT Unclassified	18. SECURITY CLASSIFICATION OF THIS PAGE Unclassified	19. SECURITY CLASSIFICATION OF ABSTRACT Unclassified	20. LIMITATION OF ABSTRACT

NSN 7540-01-280-5500

Standard Form 298 (Rev. 2-89)
Prescribed by ANSI Std. Z39-18
298-102

METRIC/ENGLISH CONVERSION FACTORS

ENGLISH TO METRIC

LENGTH (APPROXIMATE)

- 1 inch (in) = 2.5 centimeters (cm)
- 1 foot (ft) = 30 centimeters (cm)
- 1 yard (yd) = 0.9 meter (m)
- 1 mile (mi) = 1.6 kilometers (km)

AREA (APPROXIMATE)

- 1 square inch (sq in, in²) = 6.5 square centimeters (cm²)
- 1 square foot (sq ft, ft²) = 0.09 square meter (m²)
- 1 square yard (sq yd, yd²) = 0.8 square meter (m²)
- 1 square mile (sq mi, mi²) = 2.6 square kilometers (km²)
- 1 acre = 0.4 hectare (he) = 4,000 square meters (m²)

MASS - WEIGHT (APPROXIMATE)

- 1 ounce (oz) = 28 grams (gm)
- 1 pound (lb) = 0.45 kilogram (kg)
- 1 short ton = 2,000 pounds (lb) = 0.9 tonne (t)

VOLUME (APPROXIMATE)

- 1 teaspoon (tsp) = 5 milliliters (ml)
- 1 tablespoon (tbsp) = 15 milliliters (ml)
- 1 fluid ounce (fl oz) = 30 milliliters (ml)
- 1 cup (c) = 0.24 liter (l)
- 1 pint (pt) = 0.47 liter (l)
- 1 quart (qt) = 0.96 liter (l)
- 1 gallon (gal) = 3.8 liters (l)
- 1 cubic foot (cu ft, ft³) = 0.03 cubic meter (m³)
- 1 cubic yard (cu yd, yd³) = 0.76 cubic meter (m³)

TEMPERATURE (EXACT)

$$[(x-32)(5/9)]\text{ }^{\circ}\text{F} = y\text{ }^{\circ}\text{C}$$

METRIC TO ENGLISH

LENGTH (APPROXIMATE)

- 1 millimeter (mm) = 0.04 inch (in)
- 1 centimeter (cm) = 0.4 inch (in)
- 1 meter (m) = 3.3 feet (ft)
- 1 meter (m) = 1.1 yards (yd)
- 1 kilometer (km) = 0.6 mile (mi)

AREA (APPROXIMATE)

- 1 square centimeter (cm²) = 0.16 square inch (sq in, in²)
- 1 square meter (m²) = 1.2 square yards (sq yd, yd²)
- 1 square kilometer (km²) = 0.4 square mile (sq mi, mi²)
- 10,000 square meters (m²) = 1 hectare (ha) = 2.5 acres

MASS - WEIGHT (APPROXIMATE)

- 1 gram (gm) = 0.036 ounce (oz)
- 1 kilogram (kg) = 2.2 pounds (lb)
- 1 tonne (t) = 1,000 kilograms (kg) = 1.1 short tons

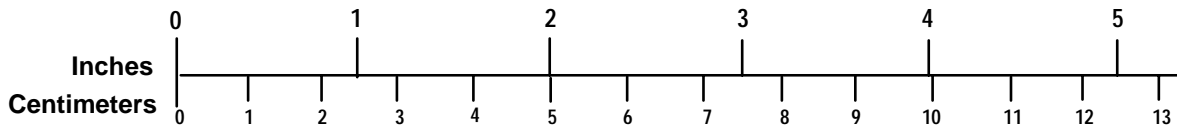
VOLUME (APPROXIMATE)

- 1 milliliter (ml) = 0.03 fluid ounce (fl oz)
- 1 liter (l) = 2.1 pints (pt)
- 1 liter (l) = 1.06 quarts (qt)
- 1 liter (l) = 0.26 gallon (gal)
- 1 cubic meter (m³) = 36 cubic feet (cu ft, ft³)
- 1 cubic meter (m³) = 1.3 cubic yards (cu yd, yd³)

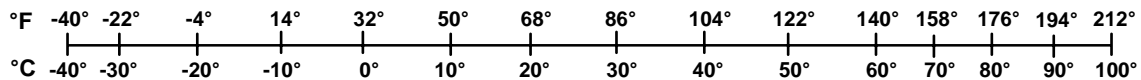
TEMPERATURE (EXACT)

$$[(9/5)y + 32]\text{ }^{\circ}\text{C} = x\text{ }^{\circ}\text{F}$$

QUICK INCH - CENTIMETER LENGTH CONVERSION



QUICK FAHRENHEIT - CELSIUS TEMPERATURE CONVERSION



For more exact and or other conversion factors, see NIST Miscellaneous Publication 286, Units of Weights and Measures. Price \$2.50 SD Catalog No. C13 10286

Updated 6/17/98

Contents

Illustrations	v
Tables	viii
Executive Summary	1
1. Background.....	3
2. Elements of Current DTA Procedure	5
2.1 Elastic FE Analysis of Tank Car	5
2.2 Fatigue Crack Growth Calculations	5
2.3 Fracture Mechanics Model.....	8
3. Proposed Multi-Level Fatigue Life Assessment Procedure	11
3.1 Areas Selected for Investigation.....	11
4. Development of the Level 2 Procedures	15
4.1 Surface Crack Growth and Trajectory Studies.....	15
4.2 Load Redistribution Effects (Elastic FE Analyses with Embedded Through and Surface Cracks)	21
5. Sample Fatigue Life Calculations for Level 2a Procedure.....	43
5.1 Crack Growth Comparisons: DTA versus Level 2a Procedure	43
6. FE Study on Plasticity and Crack Closure Effects for Through Cracks.....	45
6.1 Alternative Crack Growth Models	45
6.2 FE Models of Slanted and Deflected Through Cracks.....	49
6.3 Closure Behavior of Slanted and Deflected Cracks: FE Results.....	50
6.4 Development and Improved Crack Growth Model.....	57
6.5 Two-Dimensional Elasto-Plastic FE Analysis of Tank Car Stub Sill Model.....	58
7. Summary and Conclusions	67
8. References	69
Appendix A. Detailed FE Study on Plasticity and Crack Closure Effects for Through Cracks..	73
Abbreviations and Acronyms	89

Illustrations

Figure 1. FE model of stub sill tank car showing (magnified) deformed shape under vertical coupler loading.	6
Figure 2. Hot spot (von Mises) stresses in stub sill under vertical coupler loading.	7
Figure 3. Crack growth curve (schematic).	8
Figure 4. Apparent fracture toughness as affected by constraint (schematic).	9
Figure 5. Remote fatigue loads with different degrees of bending.	15
Figure 6. Surface crack geometry.	16
Figure 7. Shape of surface crack at breakthrough (according to Raju Newman [4,5] solution in NASGRO). Shape at breakthrough is sensitive to initial crack size and shape and depends significantly only on the DOB in the hot spot stress distribution.	17
Figure 8. Surface length of crack at breakthrough (according to Raju Newman [4,5] solution in NASGRO). Length at breakthrough is insensitive to initial crack size and shape and depends significantly on the DOB in the hot spot stress distribution.	18
Figure 9. Evolution of surface crack shape (termed crack trajectory) for different initial shape determined using NASGRO.	19
Figure 10. Stub sill substructures: Geometry, dimensions, and plan view.	23
Figure 11. Hot spot stresses in intact stub sill substructure under vertical coupler loading.	24
Figure 12. Hot spot stress distributions in intact stub sill substructure, with 24-in and 48-in overhangs, for 100 kip vertical coupler load. DOB = 0.50.	25
Figure 13. FE model of stub sill substructure, showing 5-in long embedded through crack in sill at base of shoe.	26
Figure 14. Von Mises stress in stub sill substructure with 5-in long embedded through crack in sill at base of head brace.	27
Figure 15. Stub sill substructure with embedded surface crack in sill top plate. Deformed shape (magnified) under vertical coupler load.	29
Figure 16. Stub sill substructure with embedded surface crack. Von Mises stress under vertical coupler load. The refined mesh contains the crack.	30
Figure 17. SIFs for stub sill substructure with embedded through cracks (from 1-in to 5-in long) in sill top plate. Vertical coupler load = 100 kips.	31
Figure 18. Through thickness distribution of SIFs for stub sill substructure with embedded through cracks in sill top plate. Vertical coupler load = 100 kips. Crack lengths vary from 1 in to 5 in.	32
Figure 19. SIFs for stub sill substructure with embedded surface cracks in sill top plate. Vertical coupler load = 100 kips.	33

Figure 20. SIFs (FE and Raju Newman [4,5]) for stub sill substructure over full range from surface to through crack regime. Vertical coupler load = 100 kips. Discontinuity exists between Raju Newman surface crack SIF and through crack SIF at Crack Tip c when crack breaks through.	35
Figure 21. Change in crack stress regime as through crack grows in stub sill top plate. Equivalent means stress σ_m calculated from computed SIFs. Vertical coupler load = 100 kips. Crack lengths vary from 1 in to 5 in.....	37
Figure 22. Equivalent far field DOB in stub sill substructure with embedded through cracks in sill top plate. Calculated from computed SIFs. Vertical coupler load = 100 kips. Crack lengths vary from 1 in to 5 in.	38
Figure 23. Schematic representation of a cruciform specimen for biaxial fatigue testing (after McClung [6]).	39
Figure 24. Crack growth rates for different biaxiality ratios and maximum stresses based on data of Brown and Miller for a 304 Stainless Steel (after McClung [6]). Top correlates with ΔK ; bottom correlates with ΔK_{eff}	40
Figure 25. Normalized crack opening stresses as a function of maximum stress for three different biaxiality ratios (after McClung [6])......	41
Figure 26. Crack growth curves for stub sill substructure under repeated 100 kip vertical coupler load ($R = 0$). Comparison between current DTA and proposed procedure. Both use the same Paris Law for crack growth.....	44
Figure 27. Slanted crack (left) and deflected crack (right).	49
Figure 28. (a) Geometry 1: slanted crack, (b) Geometry 2: crack deflection after stabilization, and (c) Geometry 3: crack deflection before stabilization. (L^* denotes the stabilization crack length.).....	51
Figure 29. Normalized Mode I opening levels for a 45° slanted fatigue crack for two different R ratios, plane stress (all lengths are in mm).....	52
Figure 30. Effect of crack orientation on stable Mode I opening levels $R = -1$, plane stress. L_0 is the initial crack length (all lengths are in mm).	53
Figure 31. Mode I opening levels for a deflected crack. Deflection occurs after stabilization (all lengths are in mm).	55
Figure 32. Mode I opening levels for a deflected crack. Deflection occurs before stabilization (all lengths are in mm).	55
Figure 33. The effect of friction coefficient on opening levels for a 45° slanted crack, plane stress, $R = -1$. Results show that for lower friction coefficients, the crack opening levels are lower (all lengths are in mm).....	56
Figure 34. FE mesh for tank car stub sill (all lengths are in mm) A relatively coarse mesh has been used for faster computation, requiring a large remote stress $S_{max}/\sigma_0 = 0.8$ to ensure that crack tip plasticity is captured accurately for reliable estimates of crack opening levels.	59

Figure 35. Variation of J integral at the stationary and moving crack tip as the fatigue crack grows away from the hot spot. All lengths are in mm. The J integral values correspond to a hypothetical stress level of $S_{max}/\sigma_0 = 0/8$ and do not reflect actual values for fatigue cracks in tank car stub sills. 61

Figure 36. Mode I opening levels for (a) crack growing towards and (b) crack growing away from the hot spot in the tank car stub sill model. All lengths are in mm. 62

Figure 37. FE estimates of effective SIF for fatigue crack growing towards the hot spot in the stub sill model. The estimates are significantly higher than the values expected for actual tank car stub sill cracks. This is due to the large remotely applied stress $S_{max}/\sigma_0 = 0.8$. All lengths are in mm. 63

Figure 38. Computed estimates of crack growth rates for (a) crack growing towards and (b) crack growing away from the hot spot in the stub sill model. The selected Paris Law constants C and m correspond to commercial steel. The crack growth rates predicted here do not reflect actual crack propagation rates in tank car stub sills. All lengths are in mm. 64

Figure 39. Life prediction for the stub sill as a function of crack length. The above life prediction provides a comparison between the crack growth rate for a crack growing away from the hot spot and for a crack growing towards the hot spot. The above values of crack length (a) and number of cycles (N) do not correspond to predicted values for actual fatigue cracks in tank car stub sills. 65

Tables

Table 1. Crack aspect ratios (a/c) for embedded surface cracks (a/T = crack depth, $2c_i/T$ = initial surface crack strength).....	28
Table 2. Parameters for sample fatigue lift calculations.....	43

Executive Summary

This report presents the results of the Federal Railroad Administration (FRA) project DTFR DV-00-G-60019 (Tank Car Reliability Design and Analysis), carried out in the Department of Civil and Environmental Engineering and the Department of Mechanical and Industrial Engineering at the University of Illinois at Urbana-Champaign (UIUC).

The overall objective of the project was to propose and develop new and improved rational procedures for assessing the structural integrity of stub sill tank cars, in order to provide higher levels of assurance against the occurrence of structural failure of a car that could lead to an accident.

This research specifically focuses on procedures for establishing safe inspection intervals to detect the presence of fatigue cracks in the stub sill assembly before they grow to critical size. As a result of the research reported here, a new multi-level framework for inspection is proposed. Supporting analytical work is also reported.

1. Background

The need for the development of rational procedures for assessing the structural integrity of tank cars used for transportation of hazardous materials, leading to higher levels of assurance against catastrophic accidents, has been recognized for some time.

In 1987, the U.S. Department of Transportation articulated a need to ensure that small defects in tank cars be properly identified and repaired or monitored [1]. In the final report on the 1992 Dragon, Mississippi propane tank car accident, the National Transportation Safety Board (NTSB) recommended [2] that FRA, with the Research & Special Programs Administration (RSPA), develop and promulgate requirements for the periodic testing and inspection of rail tank cars to ensure the detection of flaws before they reach a critical size. NTSB recommended establishing inspection intervals that take into account the following considerations: the defect size detectable by the inspection method used, the stress level, and the crack propagation characteristics of the structural component, using a damage tolerance approach. The resulting regulations (HM-201) published in September 1995 [3] prescribed the use of nondestructive inspection and allowed owners to use damage tolerance analysis principles to establish inspection items, methods and intervals.

Tank car stub sills, however, were not included under the HM-201 Final Rule. Therefore, beginning in 1995, FRA, the Association of American Railroads (AAR), the Rensselaer Polytechnic Institute (RPI), and the Chemical Manufacturers Association co-sponsored a project led by Southwest Research Institute (SwRI), working with the Tank Car Stub Sill Working Group, to develop specific damage tolerance analysis (DTA) methodology for use by tank car owners and builders. The objective was to determine inspection intervals for the various stub sill tank cars in their fleets.

The most significant early result of the SwRI-led project was the completion of one or two DTAs for specific stub sill tank car designs by each tank car builder, leading to derived inspection intervals ranging from 2 to 13 years. Based on their field experience, most of the tank car builders believe these intervals to be unrealistically low. This was generally attributed to several acknowledged conservative assumptions incorporated in the SwRI-developed DTA methodology.

Subsequently, as a part of the Tank Car Safety Project, the Transportation Technology Center, Inc., with FRA funding, performed a full-scale damage tolerance test of a single tank car on the Simuloader to provide data for the critical evaluation of the technologies incorporated in the specific DTA methodology developed by SwRI.

Several important results emerged from the Simuloader test: (1) the finite element (FE) analysis of the tank car, which identified local hot spot stresses at the locations of the fatigue cracks that resulted from the application of coupler loads, was not consistent with experimental measurements for some coupler loading conditions; (2) the calculated rate of growth of the fatigue cracks, based on the recommended crack growth models, generally exceeded the observed growth rates, even after correcting the FE hot spot stresses to more closely agree with

test observations; and (3) some fatigue cracks were observed to grow and then later arrest. This latter observation is relevant to the anecdotal evidence of the tank car builders that cracks, significantly longer than the critical length according to DTA and which had arrested without causing catastrophic failure, have been observed in field inspections of tank cars.

As a result of these initial efforts, SwRI prepared a path forward white paper “Future Directions for Tank Car Stub Sill Damage Tolerance Analysis,” outlining several possible improvements in the initial version of DTA. This white paper was based on discussions held at a September 1998 meeting of analysts who had conducted the first round of DTA analyses for the tank car builders. The SwRI white paper identified some of the same issues that had been cited in the initial UIUC proposal to FRA (July 15, 1998) as potential areas of improvement in the current DTA methodology. That initial UIUC proposal eventually led to the current project, Tank Car Reliability Design and Analysis.

The immediate objective of the project has therefore been to explore, evaluate, and, if warranted, further develop some of these potential improvements in the initial version of DTA, keeping in mind the necessity to arrive at a DTA methodology that is feasible for practical use.

The next section briefly outlines the basic elements of the current (SwRI) DTA procedure to provide a point of reference for describing the work carried out in this project.

2. Elements of Current DTA Procedure

The current (SwRI) DTA analysis procedure consists of several distinct, and essentially independent, analysis modules, which the following describes.

2.1 Elastic FE Analysis of Tank Car

An elastic FE analysis of the complete tank car, without any embedded fatigue cracks, establishes areas of high stress (hot spots) where fatigue cracks are likely to initiate and provides local stress distributions (hot spot stresses) for use in the crack growth analysis. Stress distributions are obtained for each coupler loading condition (Buff, Draft, Vertical Coupler Down, Vertical Coupler Up). Figure 1 shows the FE model of a typical stub sill tank car subjected to a Vertical Coupler Down (VCD) loading. Figure 2 shows local hot spot stresses in the head brace under the same VCD loading. The development of the FE model of the tank car is by far the most time consuming and expensive part of the DTA procedure.

The effect of the growing (surface or through) crack on the stress distribution in the stub sill is not accounted for in this global stress analysis.

2.2 Fatigue Crack Growth Calculations

A separate uncoupled (from the FE analysis) fatigue crack growth calculation at each fracture critical location uses the NASGRO software. The input stresses are obtained from the hot spot stress distributions calculated from the FE analysis in step 1. Figure 3 displays a typical crack growth curve (schematic), showing crack length versus number of load cycles (expressed here in terms of over-the-road (OTR) miles). The crack growth curve starts from an assumed initial size and terminates at the critical length. A factor of safety of 2 is recommended as indicated in the figure.

2.2.1 Coupler Loading

The load schedule Stub Sill Spectrum 10,000 miles (SSS10) that was synthesized from recorded load data by SwRI contains the load histories that are used in the DTA crack growth calculations. One schedule corresponds to 10,000 OTR miles and is simply repeated in the analysis until a crack reaches critical size. Several different coupler loading conditions are included (Buff, Draft, Vertical Coupler Up, VCD), and load data is also classified as to whether the tank car was full or empty, although this detail proved difficult, if not impossible, to account for in NASGRO. Comparative crack growth calculations using NASGRO have shown that the VCD loading condition typically accounts for approximately 95 percent of the growth of fatigue cracks in critical locations around the head brace in the stub sill.

The initial surface crack size (surface length and depth) used in the NASGRO calculations are currently assumed (surface length = 0.125 in, depth = 0.0125 in). The smaller the initial (detectable) crack size, the longer the remaining fatigue life. The initial crack size should actually be determined by the probability of detection of a given crack size with the non-destructive evaluation technology being used.

The specific crack growth model in NASGRO, recommended for DTA, uses the simple Paris law, which neglects several important factors, such as crack closure arising from local plasticity effects and constraint (multiaxial stress effects).

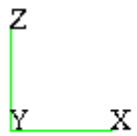
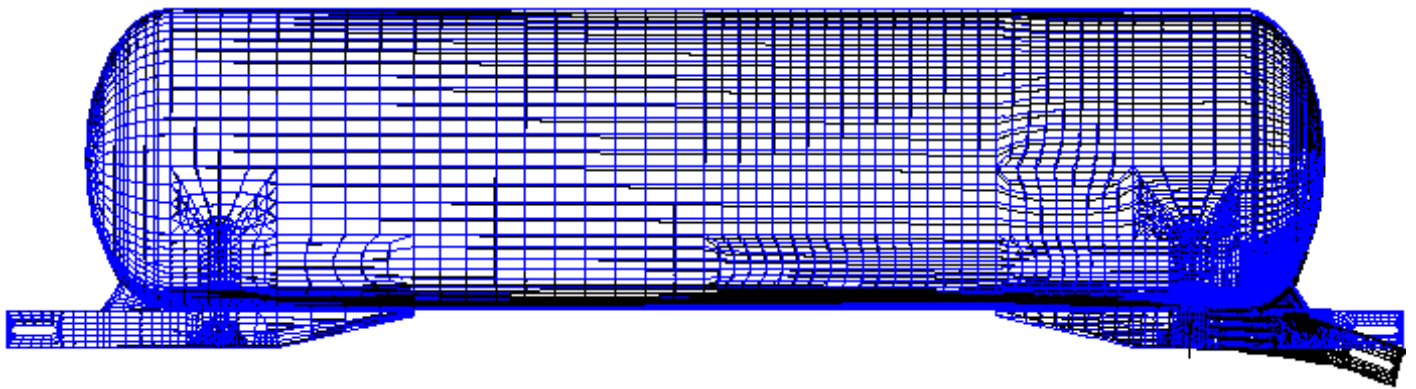


Figure 1. FE model of stub sill tank car showing (magnified) deformed shape under vertical coupler loading.

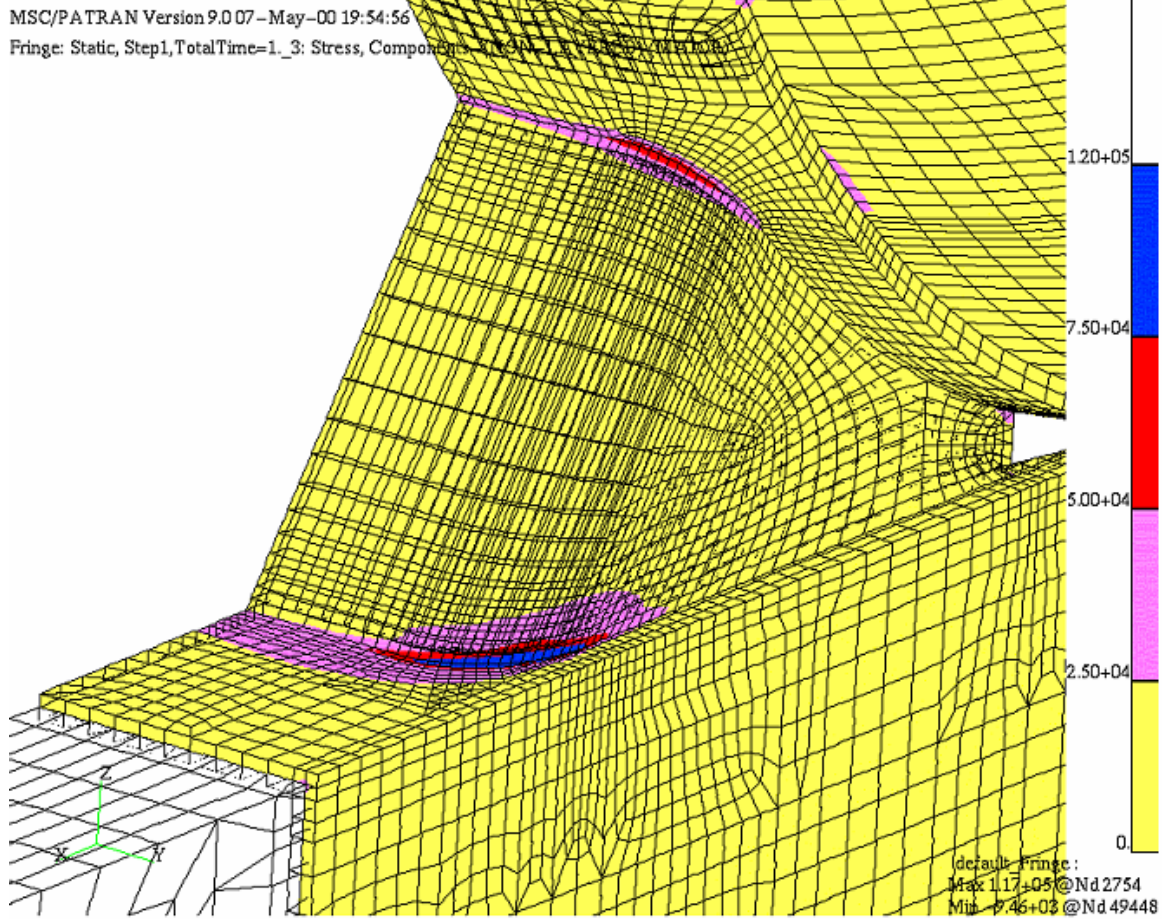


Figure 2. Hot spot (von Mises) stresses in stub sill under vertical coupler loading.

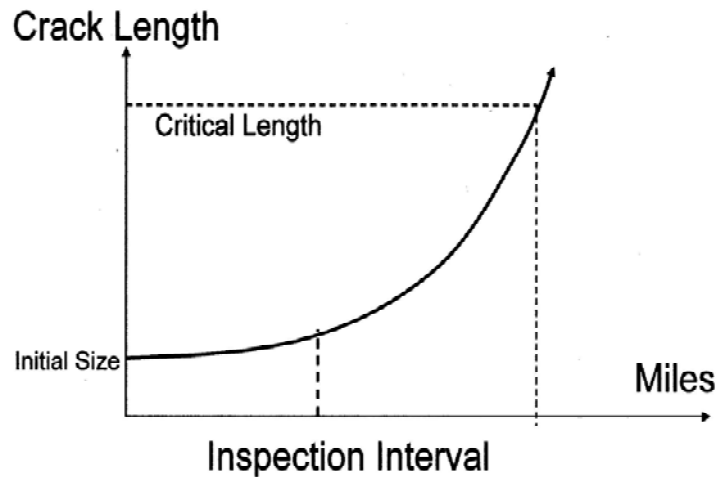


Figure 3. Crack growth curve (schematic).

The original hot spot stresses, determined in the absence of the crack, are used in NASGRO to drive the crack growth. This assumption is accurate only for very small cracks. The stress intensity factors (SIFs), in reality, are affected by the presence of the growing crack.

In DTA analyses performed to date, most of the stub sill fatigue life is spent as a growing surface crack, and relatively little life remains after the crack breaks through. This, however, depends on the applicable value of fracture toughness K_C (currently recommended by SwRI for tank car steels as $110 \text{ ksi } \sqrt{\text{in}}$). For a larger value of fracture toughness, which may actually be the case, more fatigue life would exist in the through crack regime.

2.3 Fracture Mechanics Model

The SIF for the through crack in the sill is determined from a fracture mechanics model that assumes the crack is planar and that it is acted upon by a remote uniaxial stress field (the original local hot spot stresses).

Most importantly, the material fracture toughness that is used to define failure is always measured on compact specimens with no consideration of constraint effects. Figure 4 (schematic) illustrates the well-known fact that the apparent material fracture toughness that would be observed in a test depends on the local stress field around the crack tips. The right side of Figure 4 illustrates the standard compact specimens used in materials testing. A thin plate (plane stress) specimen with a central crack, shown on the left of the figure, would exhibit a higher apparent fracture toughness because of the more extensive plastic deformation around the crack tips. A similar centrally cracked plane stress specimen, but with a remotely applied biaxial stress, would yield a different value of apparent fracture toughness, less than the uniaxial stress condition but greater than the compact specimen. The remote stress applied parallel to the crack is an example of the elastic T-stress and can be used as an approximate measure of constraint.

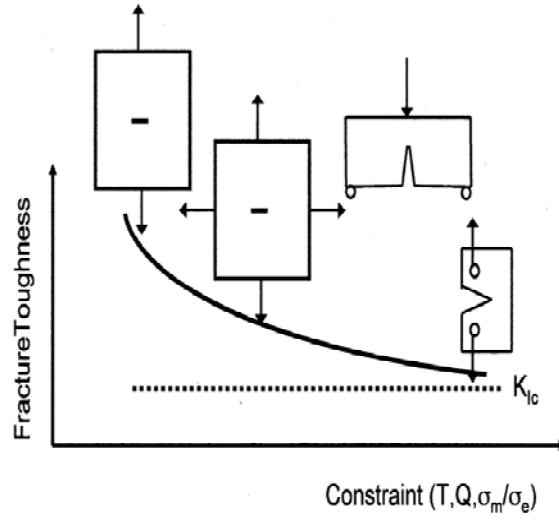


Figure 4. Apparent fracture toughness as affected by constraint (schematic).

3. Proposed Multi-Level Fatigue Life Assessment Procedure

3.1 Areas Selected for Investigation

The previous section discussed the main assumptions and simplifying approximations inherent in the current DTA procedure, which lead, in general, to conservative results, i.e., they tend to reduce the predicted (calculated) fatigue life.

The simplifications fall into three main categories: (a) structural modeling and analysis of the stub sill, (b) fatigue crack growth calculation, and (c) determination of the stub sill critical crack length (as a function of fracture toughness) at which failure is deemed to occur.

Improvements, leading to a more accurate (and less conservative) assessment of stub sill fatigue life, appear to be possible in each of these three categories. Of the areas of possible improvement in the initial version of DTA, the following two appeared to be the most fruitful for investigation for possible inclusion in DTA:

1. The effect of load redistribution, due to a growing crack, on the local near-tip stress regime. Directly determine crack SIFs that take growing crack size into account to drive the crack growth analysis. This was approached by developing an efficient methodology to introduce a series of embedded fatigue cracks into the FE structural models of the tank car stub sill.
2. The effect of plasticity and crack closure on crack growth rates. Replace the simple Paris law with a more accurate crack growth law that takes these effects into account. This was approached by a detailed FE modeling study of fatigue crack growth taking plasticity effects into account.

Subsequent sections present the details of the project work in these areas. Some of the other potential areas of improvement in DTA that have previously been identified and discussed will require future additional study and, in some cases, significant additional materials testing of tank car structural steels.

3.2 Summary of Proposed Procedure

The research team proposes consideration of a multi-level procedure for establishing safe inspection intervals in which tank car builders/owners can trade off the cost of more frequent inspections against the time and expense of conducting more accurate engineering evaluations of the fatigue life associated with specific stub sill tank car designs.

The following describes a possible system in which the accuracy (and complexity and cost) of the fatigue life evaluation increases from level to level, and excessive conservatism is simultaneously reduced, thus increasing the required inspection interval.

Classification of Proposed Multi-Level Procedure

- *Level 0. Standard Minimum (Default). (Inspection interval to be determined.)*
 - No special engineering evaluations or analyses of fatigue life
- *Level 1. Current DTA Evaluation Procedure.*
 - Elastic FE analysis of the tank car without embedded fatigue cracks, to establish hot spot stresses
 - Uncoupled fatigue crack growth analysis (NASGRO) using Paris Law without crack closure or constraint effects
 - Critical crack length determined using simple fracture mechanics model, and material fracture toughness K_{IC} measured on compact specimens with no consideration of constraint effects
- *Level 2a. Proposed Evaluation Procedure.*
 - Elastic FE analysis of the tank car containing snapshots of embedded fatigue cracks (surface (part through) cracks and through cracks) to establish SIFs that properly reflect load redistribution effects
 - Uncoupled fatigue crack growth analysis using SIFs from FE analysis and Paris Law without crack closure or constraint effects
 - Critical crack length determined from K_{IC} measured on compact specimens as in Level 1
- *Level 2b. Extension of Proposed Evaluation Procedure.*
 - Elastic FE analysis of the tank car as in Level 2a
 - Uncoupled fatigue crack growth analysis using SIFs from FE analysis as in Level 2a, with a crack growth law that reflects closure (plasticity) effects and multiaxial stress state (constraint)
 - Critical crack length determined from K_{IC} measured on compact specimens as in Levels 1 and 2a
- *Level 2c. Further Extension of Proposed Evaluation Procedure.*
 - Elastic FE analysis of the tank car as in Levels 2a and 2b
 - Uncoupled fatigue crack growth analysis as in Level 2b
 - Critical crack length determined from K_I that reflects constraint effects
- *Level 3. Coupled Nonlinear Evaluation Procedure (Future).*
 - Elastoplastic FE analysis of the tank car with embedded fatigue cracks
 - Coupled fatigue crack growth analysis with crack propagating in the FE model of the tank car

- Critical crack length determined from K_I that reflects constraint effects as in Level 2c

The Level 3 procedure is not currently viable for practical evaluation of fatigue life, although it is a topic of current research at several universities. Commercial software (e.g., ZENCRACK) is also becoming available for this type of analysis.

4. Development of the Level 2 Procedures

This project has focused on developing the necessary elements of the Level 2a and 2b procedures outlined above, which are believed to be practically viable procedures for fatigue life evaluation, and which are more accurate and realistic, and less conservative, than the current DTA procedure.

4.1 Surface Crack Growth and Trajectory Studies

4.1.1 Shape and Size of Surface Cracks at Breakthrough

A series of fatigue crack growth calculations were first carried out using NASGRO, along with the SSS10 load spectrum, to study how surface crack shapes evolve as they grow through the thickness of the sill top plate, before eventually becoming through cracks and continuing to grow until they reach critical size.

Figure 5 illustrates the remote fatigue loading assumed in the NASGRO crack growth simulations.

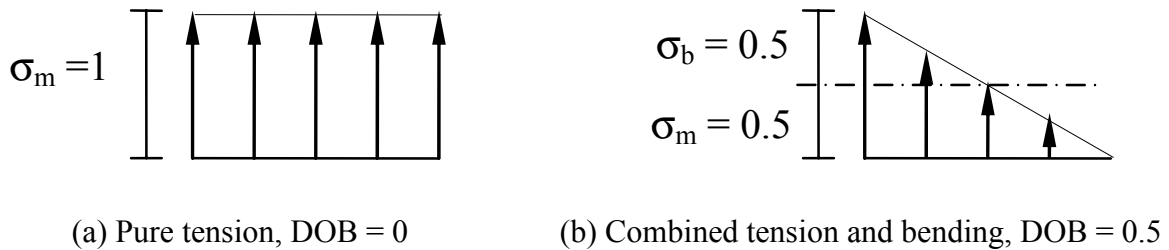


Figure 5. Remote fatigue loads with different degrees of bending.

The degree of bending (DOB) defines the shape of the (linear) through-thickness distribution of stress acting on the crack ($DOB = \frac{\sigma_b}{\sigma_b + \sigma_m}$), where σ_b = value at the top surface of the linearly varying bending stress, and σ_m = uniform (average) stress in the plate). DOB = 0 corresponds to a constant through-thickness stress distribution; DOB = 0.5 corresponds to a triangular distribution of stress, with tension stress = $\sigma_b + \sigma_m$ at the top surface and zero at the bottom; and DOB = 1 corresponds to a pure flexural distribution, with equal magnitudes of tension at the top surface and compression at the bottom surface. DOB values greater than 0.5 are not expected to produce significant crack growth.

Figure 6 illustrates the notation describing the semi-elliptical surface crack geometry, where a = crack depth and $2c$ = crack surface length.

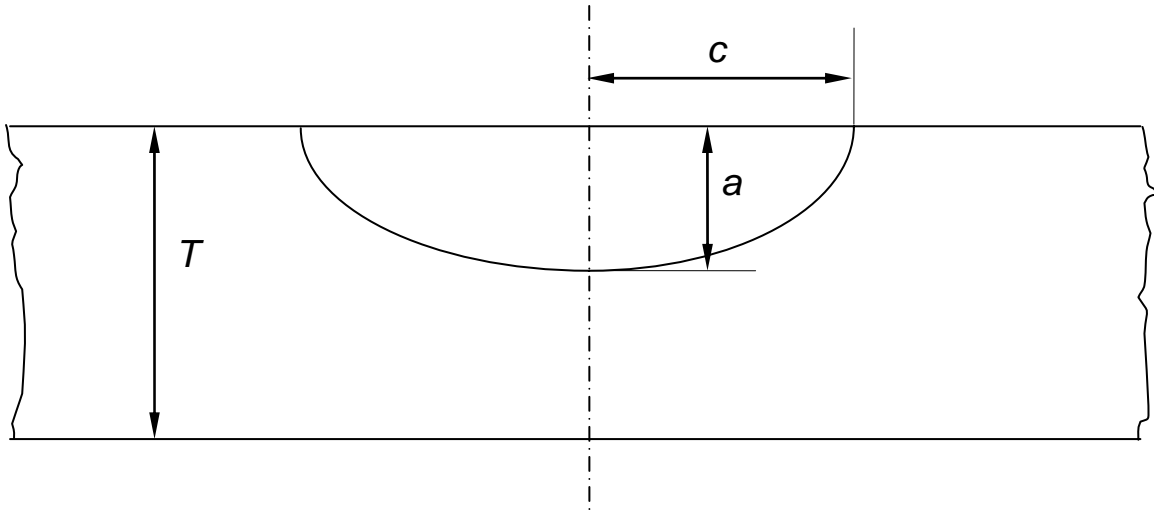


Figure 6. Surface crack geometry.

Figure 7 shows, for different initial crack shapes and crack sizes (a = current crack depth, $2c$ = current surface crack length, T = plate thickness), the final shape of the semi-elliptical surface crack at the point when the crack tip just reaches the bottom surface of the sill plate (i.e., breakthrough), as a function of DOB.

The top illustration in Figure 7 includes the effect of a local weld toe notch correction suggested by SwRI, based on an empirical/numerical solution (Lawrence and Ho); the bottom illustration excludes this notch correction. Figure 8 shows the same data presented in a different way (i.e., as the surface length of the crack at breakthrough, as a function of DOB, for the same range of initial crack shapes and sizes).

Figures 7 and 8 demonstrate the important finding that the final shape (i.e., the surface length) of the crack is affected significantly only by DOB and not by reasonable variations in initial crack shape and size, even for relatively deep initial cracks (i.e., $a_i/c_i = 0.4, 0.5$).

4.1.2 Evolution of Surface Crack Shape During Growth Through Plate Thickness

A second series of fatigue crack growth calculations were then carried out using NASGRO to determine how the shape (a/c) of a surface crack evolves as it grows and penetrates through the depth of the plate, as well as what parameters significantly affect this shape evolution. This has important implications for the possibility of developing a practical stress analysis procedure for an improved DTA, one that includes recognition of the presence of embedded cracks in the stub sill. For this second series of crack growth calculations, only vertical coupler loads were used, and the weld toe notch correction was not considered.

Figure 9(a) shows the evolution of crack shape (a/c) for DOB = 0.50 and initial surface length $2c_i/T = 0.25$ (i.e., the initial surface length of the crack is 0.25 times the plate thickness), for initial crack shapes $a_i/c_i = 0.2, 0.4, 0.5$. Interestingly, the crack at first grows more rapidly through the depth, and, then as the tip penetrates into a region of lower stress (because of the

triangular stress distribution with $DOB = 0.5$), the depth-wise growth slows down, and the surface growth becomes more rapid. It is evident that the crack trajectories are virtually identical for these different initial shapes. Figure 9(b) shows the same information for a longer initial surface length $2c_i/T = 0.50$ (i.e., 0.50 times the plate thickness). The crack trajectory is again independent of the initial crack shape. The families of crack trajectory curves in Figures 9a and 9b are different for the two different values of initial surface length ($2c_i/T = 0.25$ and 0.50), but the two trajectories actually merge together at about $a/T = 0.75$ and follow a common path to $a/T = 1.0$ (breakthrough), so that the final value of crack shape a/c at breakthrough is the same irrespective of initial surface length, as already seen in Figures 7 and 8.

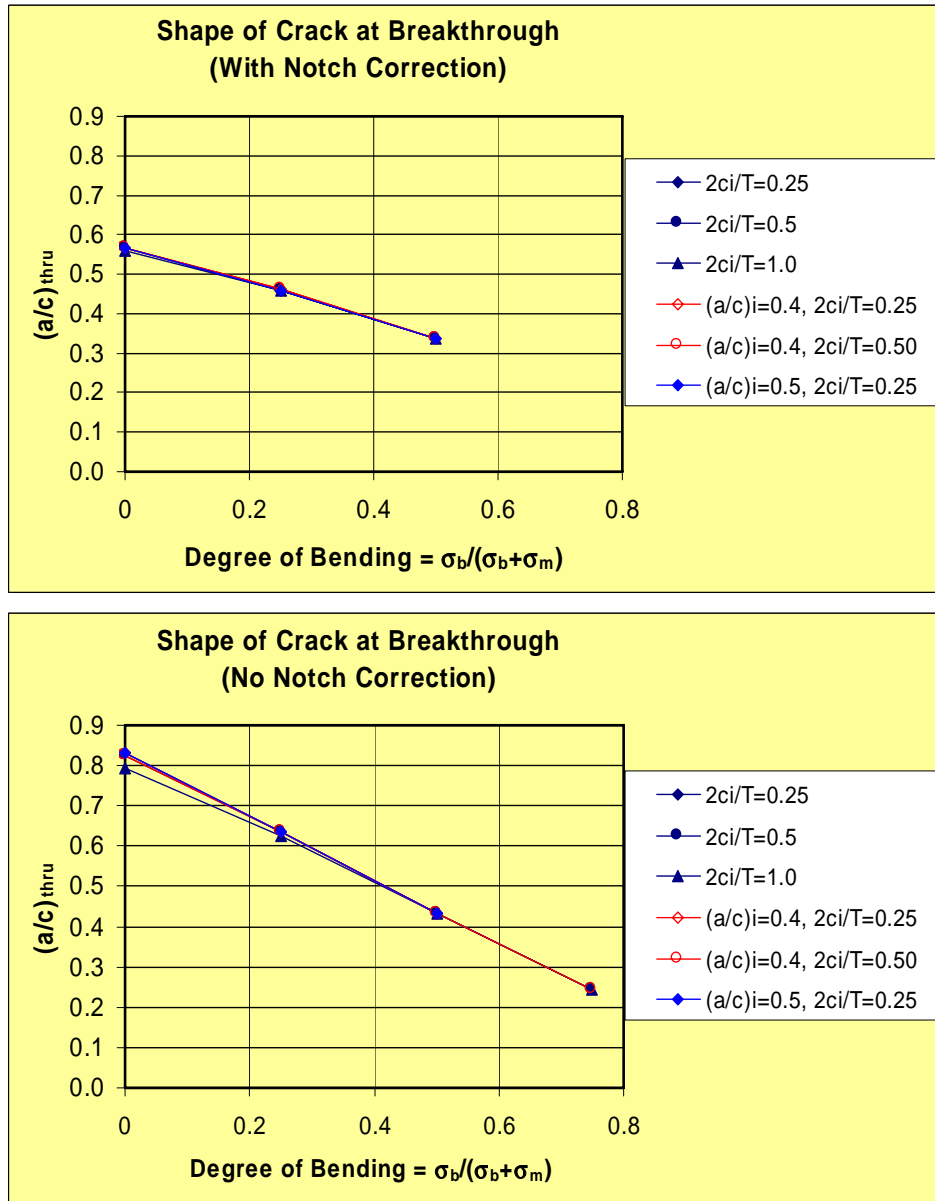


Figure 7. Shape of surface crack at breakthrough (according to Raju Newman [4,5] solution in NASGRO). Shape at breakthrough is sensitive to initial crack size and shape and depends significantly only on the DOB in the hot spot stress distribution.

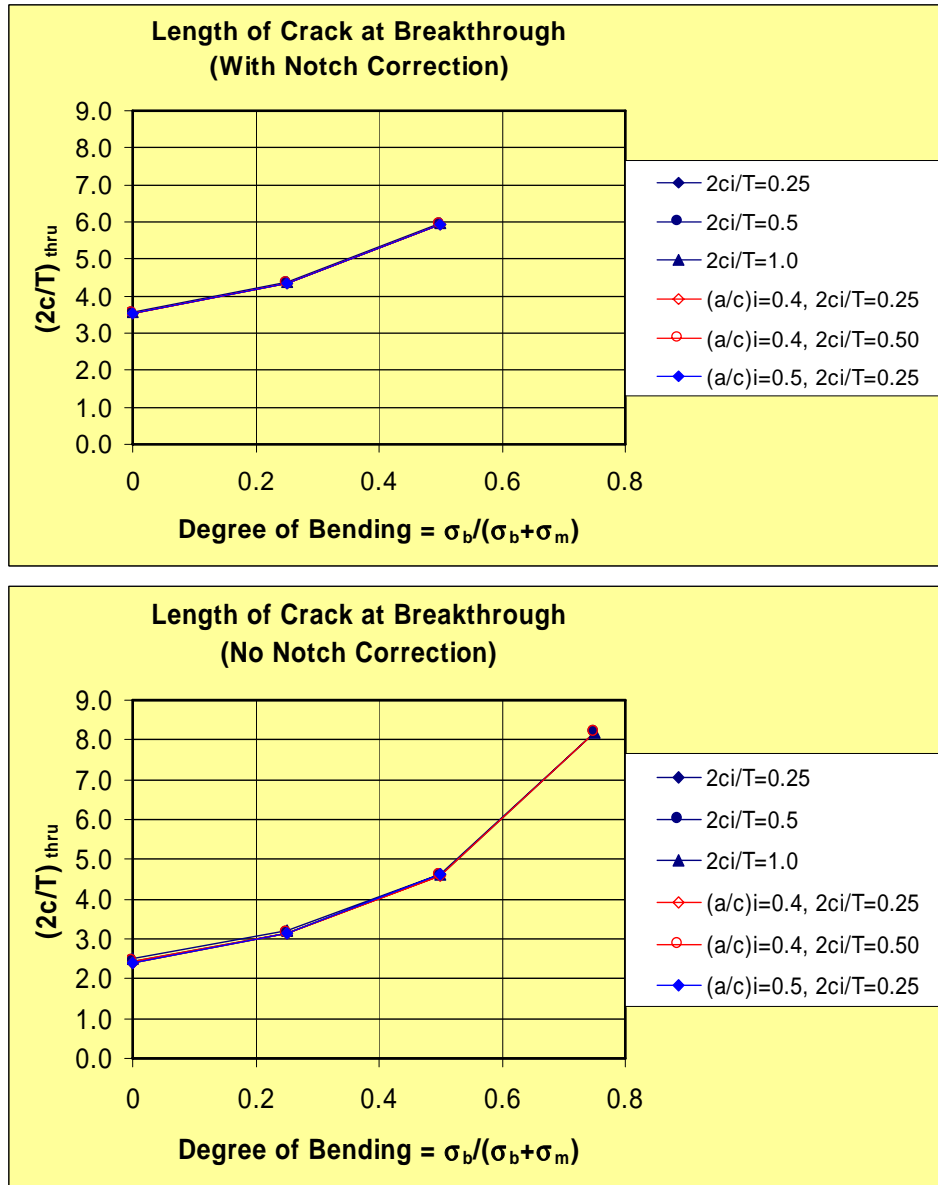
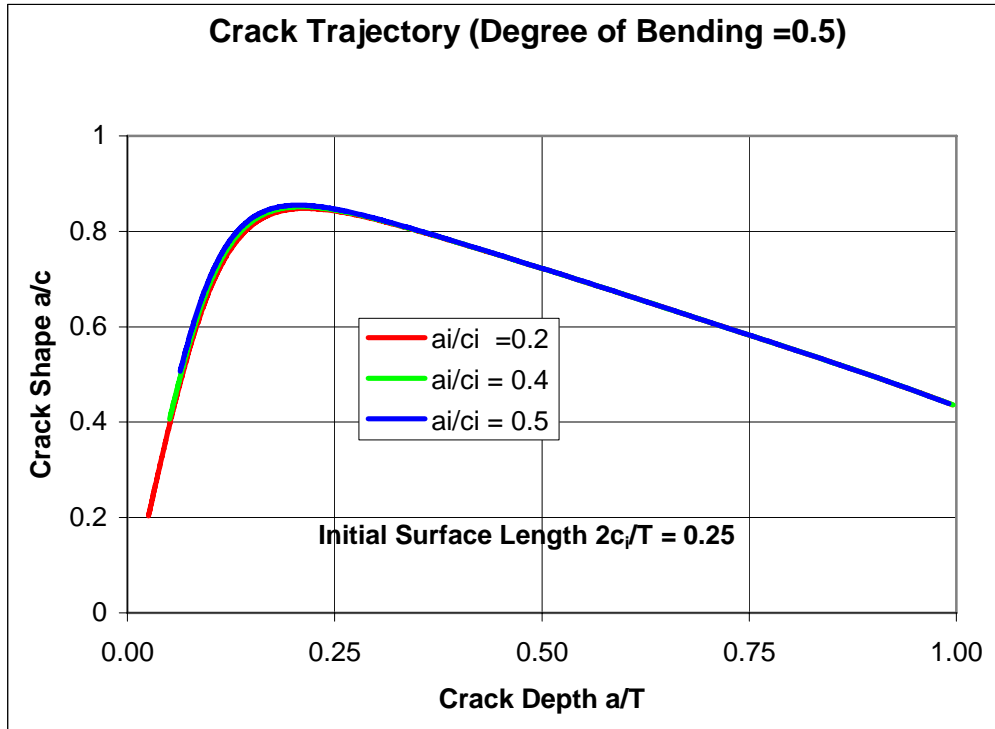
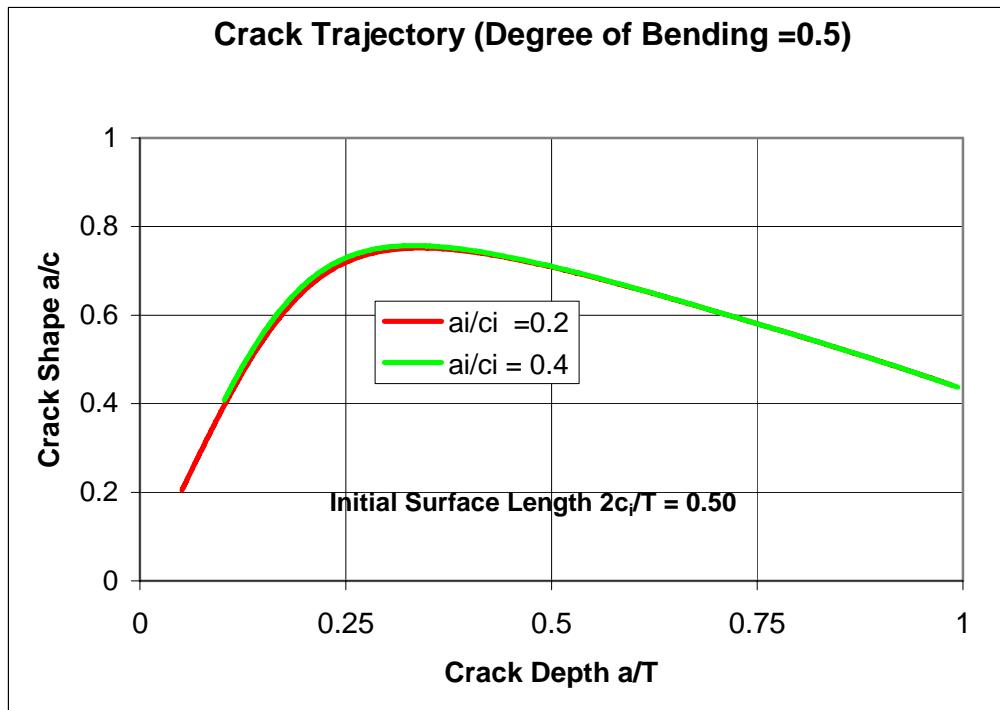


Figure 8. Surface length of crack at breakthrough (according to Raju Newman [4,5] solution in NASGRO). Length at breakthrough is insensitive to initial crack size and shape and depends significantly on the DOB in the hot spot stress distribution.



9(a). Initial surface length of crack is 0.25 times the plate thickness.



9(b). Initial surface length of crack is 0.50 times the plate thickness.

Figure 9. Evolution of surface crack shape (termed crack trajectory) for different initial shapes determined using NASGRO.

Figure 9 demonstrates the important further finding that, for a given DOB and initial crack surface length, the changing shape of the crack as it grows through the depth is independent of the initial crack shape.

These findings make possible the development of a practical structural modeling approach that takes account of the presence of a growing crack on the local crack stress regimes.

4.1.3 Use of Trajectory Information in FE Analysis of Stub Sill with Embedded Cracks

As previously described, in the current DTA procedure (Level 1), a detailed FE stress analysis of the tank car is performed, and local areas of high stress (hot spots) are determined. For the purposes of crack growth calculation in the Level 1 procedure, these local stresses are then used in a crack growth model in NASGRO as if they were far field (uniaxial) stresses acting on the crack. This is probably reasonably accurate when the crack is a very small surface crack, but it is likely a very conservative approximation when the crack has grown significantly.

In the proposed Level 2a procedure, a detailed FE stress analysis of the tank car is first performed as in the current DTA procedure to determine potential fatigue crack locations. Elastic FE models containing a few embedded (surface and through) cracks are then analyzed to directly determine SIFs in lieu of hot spot stresses, for each surface and through crack configuration, for use in the Paris Law crack growth calculation.

Surface crack trajectories can be pre-computed using NASGRO, for different DOBs and initial crack surface lengths. The appropriate series of FE models containing snapshots of the embedded cracks, which are to be analyzed, are then determined in the following way:

1. The initial FE analysis of the intact tank car determines the relevant DOB (as in the current DTA).
2. Given the prescribed detectable initial crack surface length (which is related to probability of detection issues), several embedded surface cracks of different depths (and corresponding surface lengths determined from the crack trajectory for the appropriate DOB) are incorporated in the tank car FE model (the initial FE model should be designed so that substructures containing explicit crack models can be embedded in it). Surface cracks with depths a/T (T = plate thickness) of 0.25, 0.50, and 0.75 might be modeled.
3. SIFs at the maximum crack depth and surface locations are calculated from FE analysis. Interpolation can be carried out to determine SIFs at intermediate crack depths, or analyses can be performed at additional a/T values if desired or needed (the Raju Newman solution at a very small crack depth can be included in the interpolating scheme).
4. The Paris Law is then used to carry out the crack growth analysis, using the interpolated SIFs up to breakthrough.

5. Crack growth simulation after breakthrough is continued in the same way by using embedded through cracks of different lengths up to the critical length. As a guide, the critical length can be estimated as is currently done, using the material fracture toughness obtained from compact specimens together with a simplified fracture mechanics model.

In the current DTA using NASGRO, a table of SIFs at the crack tips is pre-computed for a range of crack depths a and lengths $2c$, using an approximate solution for surface cracks (Raju Newman), which was originally derived as a simplified analytical curve fit to a series of FE solutions. This approximate solution, used in conjunction with the hot spot stresses determined for the intact stub sill, would be expected to be accurate only for quite small surface cracks. The finding that a unique crack shape can be predetermined for each given crack depth, given the DOB and initial surface length, means that only a small manageable number of FE analyses of the stub sill with embedded cracks need to be carried out.

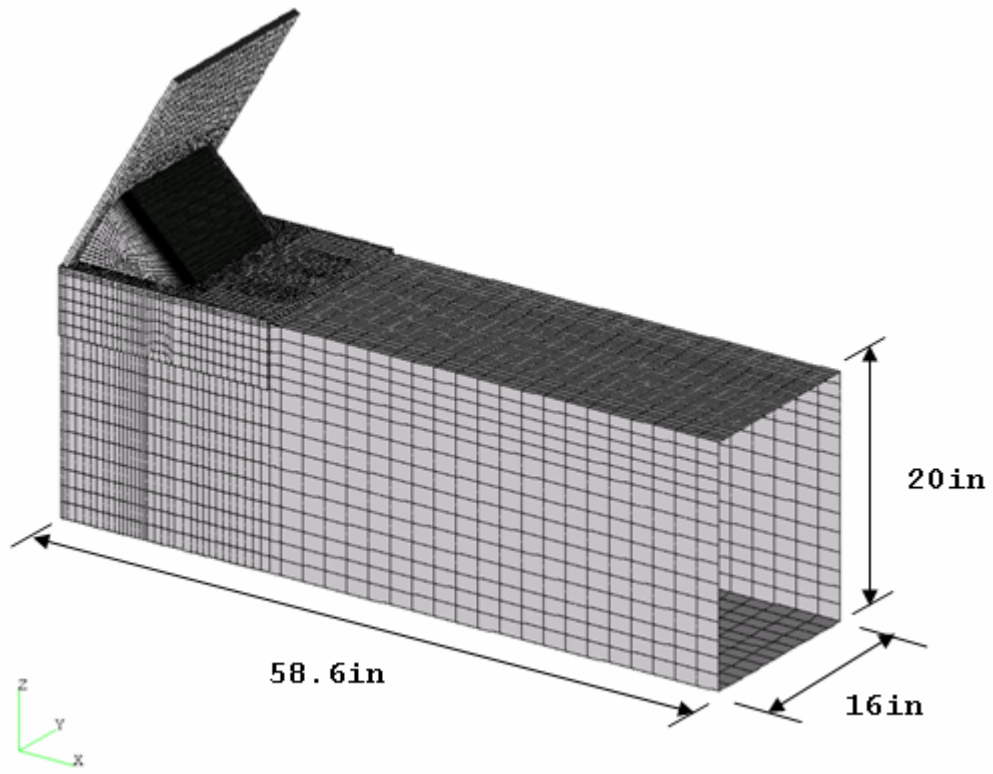
Once the SIFs have been determined as a function of crack depth a/T (for surface cracks) or crack length ($2c/T$) for through cracks, the crack growth calculations can be carried out using either the Paris Law (Level 2a) or a modified crack growth model that incorporates crack closure and constraint effects (Level 2b).

4.2 Load Redistribution Effects (Elastic FE Analyses with Embedded Through and Surface Cracks)

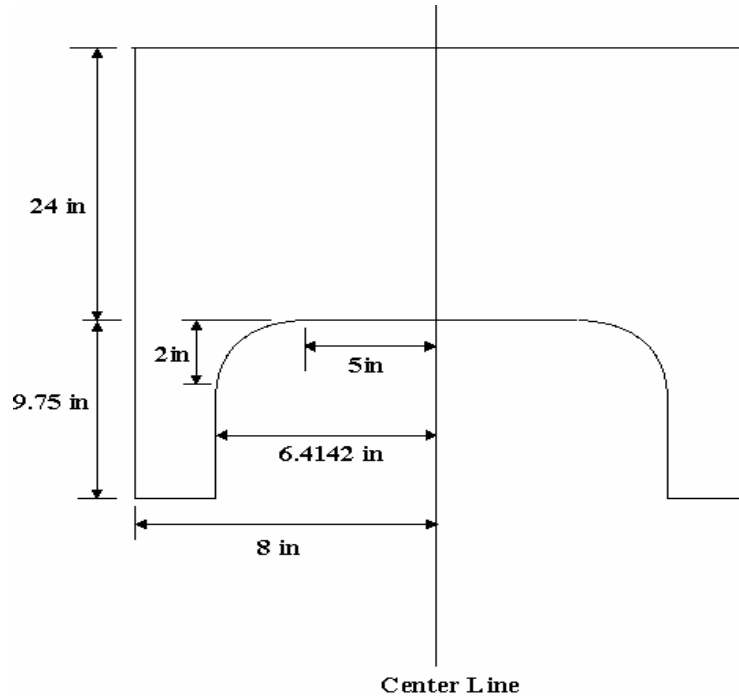
In order to investigate the feasibility of the proposed procedure, a hypothetical stub sill substructure was used, as described next.

4.2.1 FE Model of Stub Sill Substructure

The stub sill substructure shown in Figures 10a and 10b was designed to carry out the calculations of the Level 2a procedure for illustrative purposes.



10(a). Stub sill substructure. Geometry and dimensions. Sill top plate $\frac{1}{2}$ -in thick.



10(b). Stub sill substructure. Plan view (not to scale) of stub sill top plate showing head brace footprint. Hot spot under vertical coupler loading is located on the curved portion of the footprint.

Figure 10. Stub sill substructures: Geometry, dimensions, and plan view.

The sill plates are 0.5-in thick, and the head brace is angled at 45 degrees. Different overhang lengths were used to change the general stress level due to a vertical coupler load. The FE model used three-dimensional 20-node elements with 2 elements through the plate thickness in the area around the head brace and 8-noded shell elements further out in the sill towards the coupler. In the fracture critical locations around the head brace footprint, a more refined local mesh containing surface crack or through crack models was inserted as appropriate and tied to the global mesh using constraint equations in ABAQUS. The vertical coupler loading was applied as a (downward) distributed load to the (vertical) web plates at the free end of the sill.

Figure 11 shows the hot spot stress contours in the intact stub sill (without embedded cracks) under vertical coupler loading. This information is used to locate areas of potential crack growth and to determine the DOB in those areas.

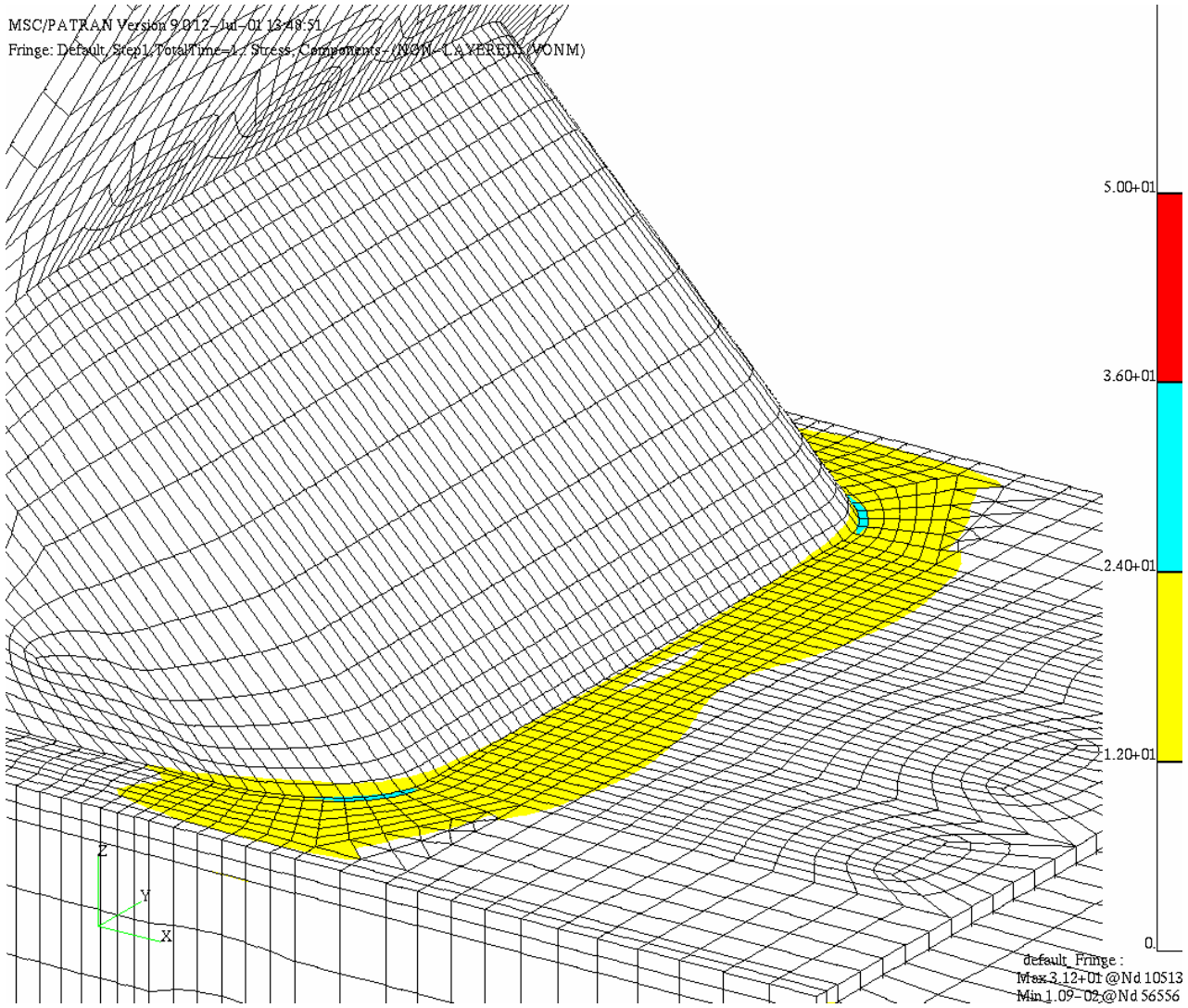


Figure 11. Hot spot stresses in intact stub sill substructure under vertical coupler loading.

Figure 12 shows the hot spot stresses at the corner hot spot, determined using the stress extrapolation and smoothing procedure currently used in DTA. The DOBs are very close to 0.50 in both cases. For the 24-in overhang, $DOB = 0.533$, indicating a small compressive stress at the bottom surface of the top plate. For the 48-in overhang, $DOB = 0.501$, a nearly exact triangular stress distribution.

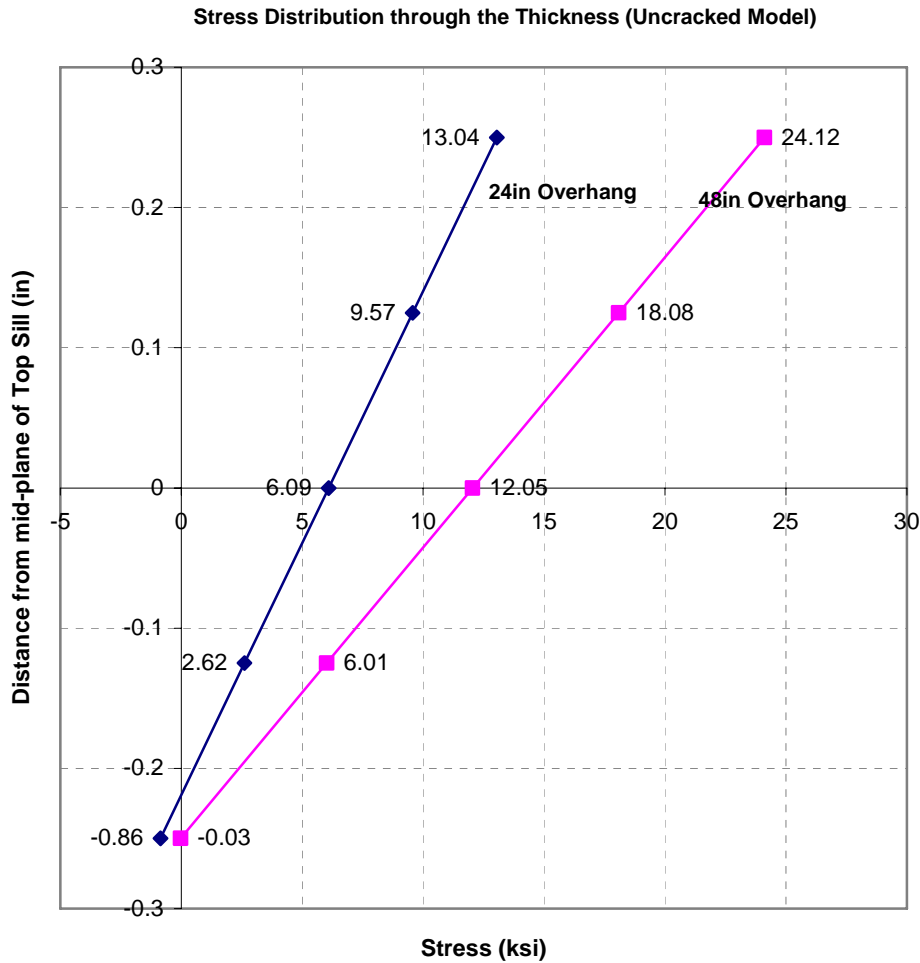


Figure 12. Hot spot stress distributions in intact stub sill substructure, with 24-in and 48-in overhangs, for 100 kip vertical coupler load. $DOB = 0.50$.

4.2.2 FE Models of Stub Sill Substructure with Embedded Cracks

Through Cracks. Figure 13 shows the stub sill FE model containing an embedded 5-in long through crack in the sill top plate. Through cracks with lengths of 1 in, 2 in, 3 in, 4 in, and 5 in were modeled. The cracks extended from the corner of the stub sill (the end of the straight segment of the head brace footprint) towards the center of the sill.

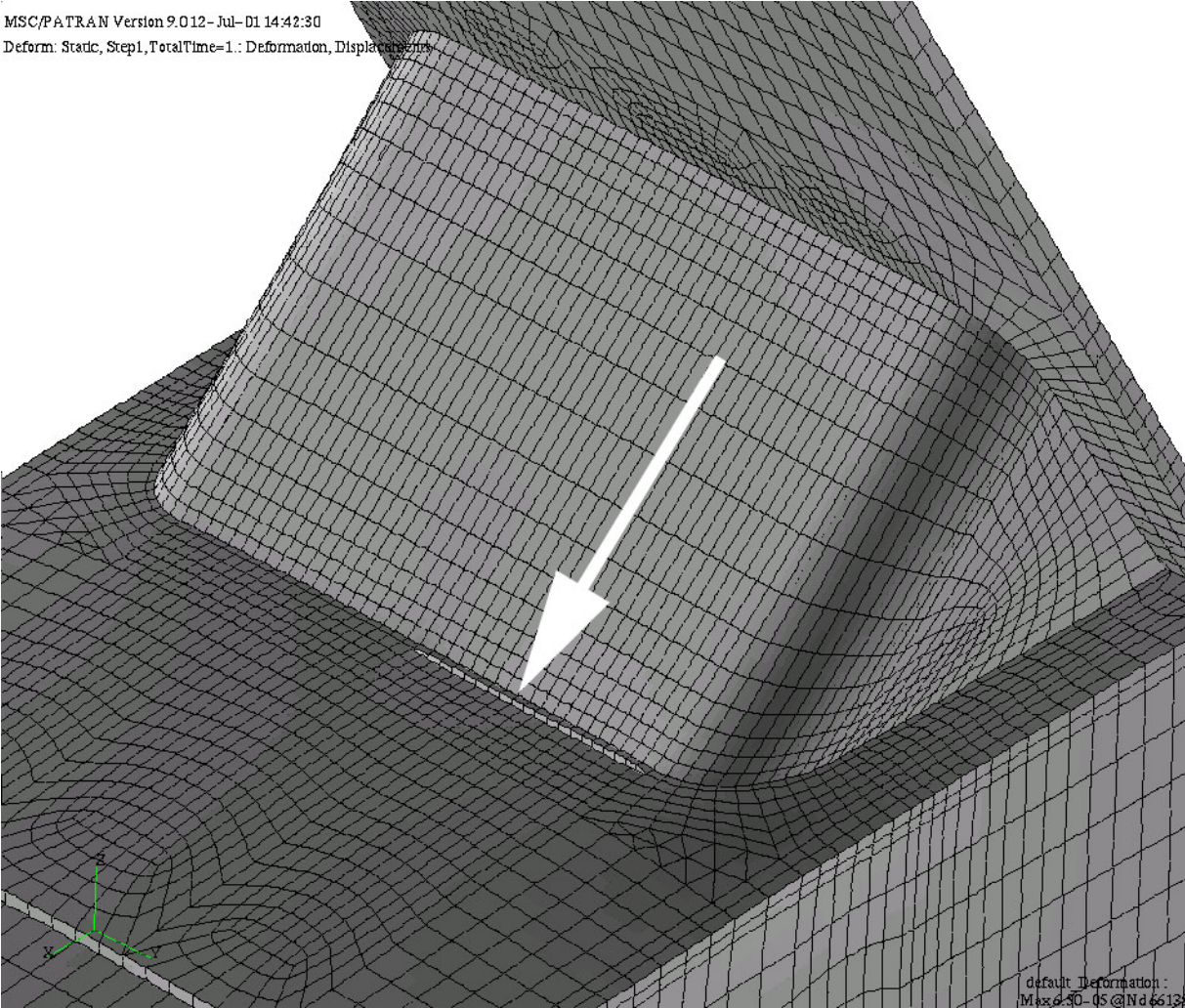


Figure 13. FE model of stub sill substructure, showing 5-in long embedded through crack in sill at base of shoe.

Figure 14 shows the von Mises stresses in the stub sill substructure with a 5-in through crack under a 100 kip vertical coupler load.

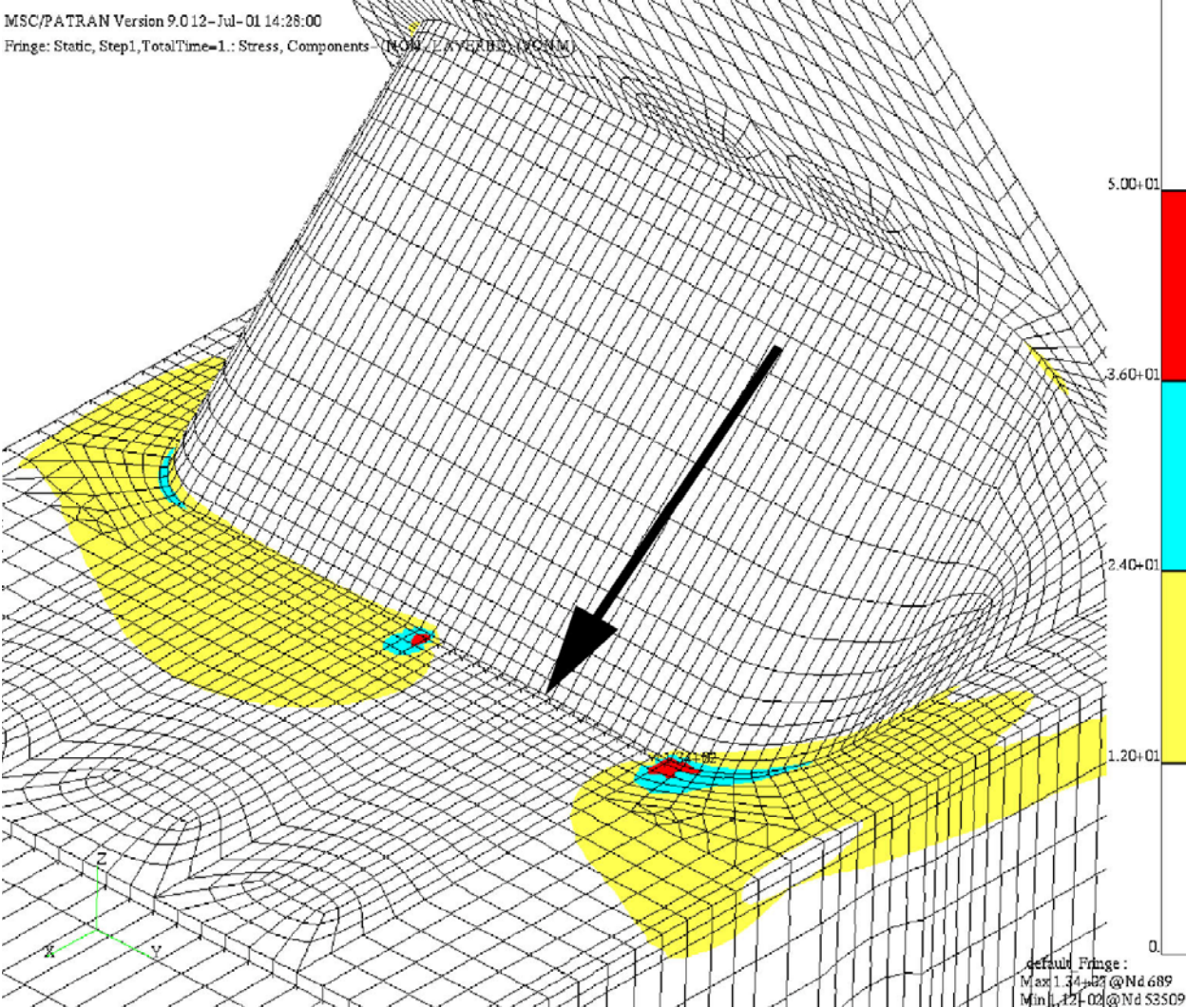


Figure 14. Von Mises stress in stub sill substructure with 5-in long embedded through crack in sill at base of head brace.

Surface Cracks. Surface cracks with crack depths $a/T = 0.25, 0.50,$ and 0.75 were modeled and embedded in the stub sill substructure model. The surface length ($2c$) for each crack depth was determined from the crack trajectory information (shown in Figure 9) for initial crack lengths $2c_i/T = 0.25$ (i.e., an 1/8-in long initial crack), 0.50 and 1.0 , and $DOB = 0.5$. The surface crack geometries used to generate the embedded surface crack snapshots are as follows (see Figure 6):

Table 1. Crack aspect ratios (a/c) for embedded surface cracks ($a/T =$ crack depth, $2c_i/T =$ initial surface crack strength).

	Initial Surface Crack Length $2c_i/T$		
a/T	<i>0.25</i>	<i>0.50</i>	<i>1.0</i>
<i>0.25</i>	0.85	0.725	0.45
<i>0.50</i>	0.725	0.725	0.65
<i>0.75</i>	0.60	0.60	0.60

Figure 15 shows the stub sill FE model containing an embedded surface crack in the sill top plate. The figure shows the refined local mesh inside the coarser global mesh.

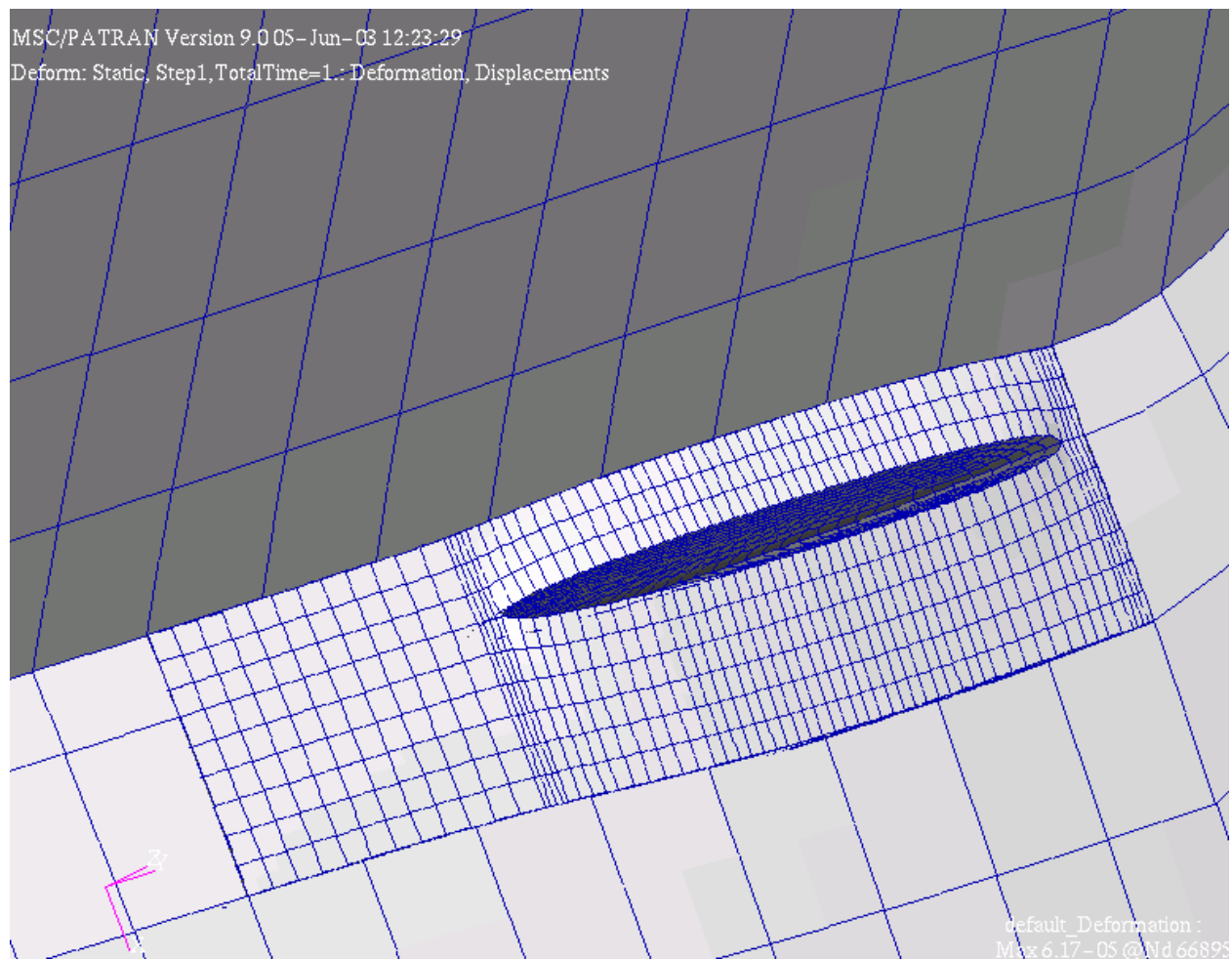


Figure 15. Stub sill substructure with embedded surface crack in sill top plate. Deformed shape (magnified) under vertical coupler load.

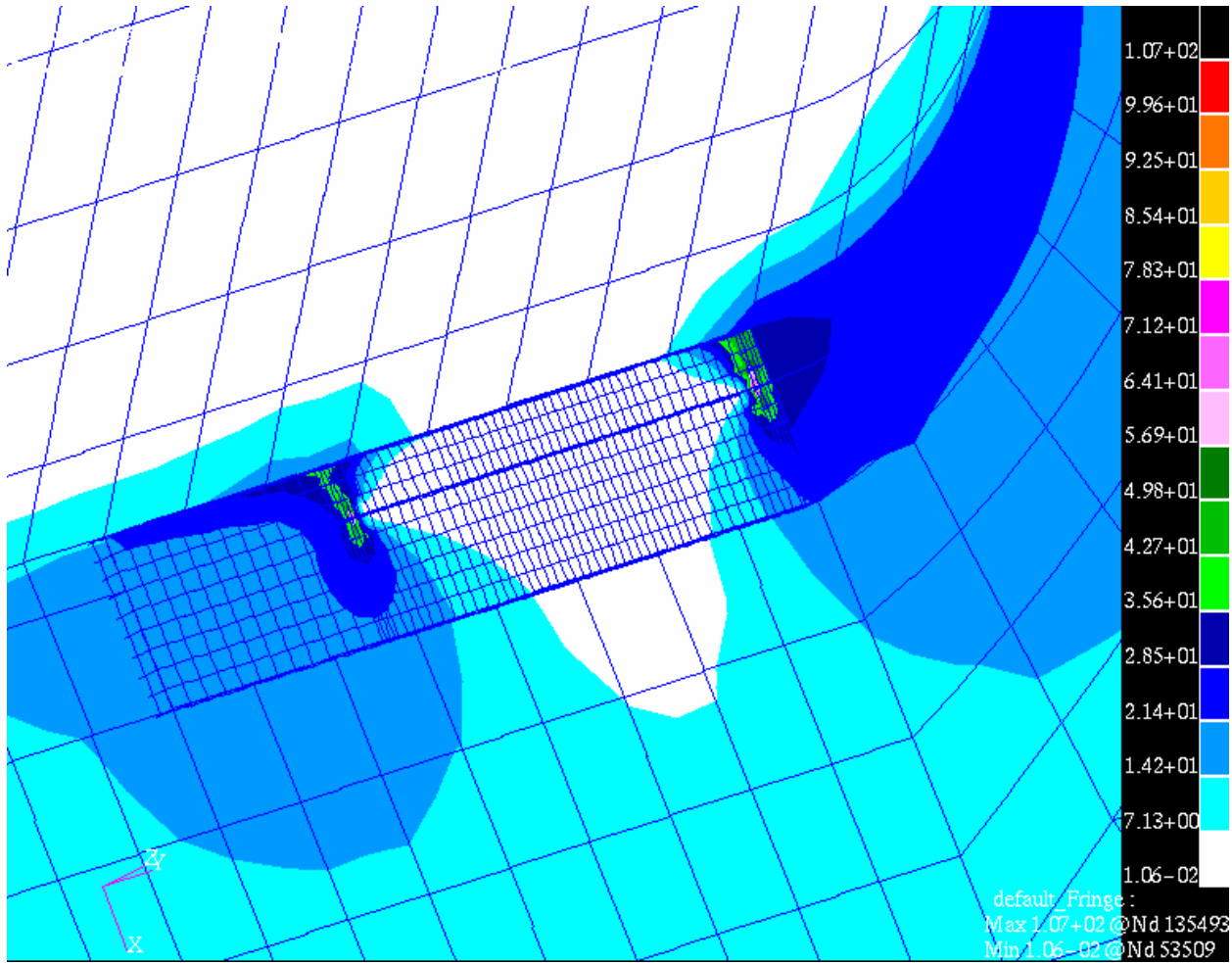


Figure 16. Stub sill substructure with embedded surface crack. Von Mises stress under vertical coupler load. The refined mesh contains the crack.

Figure 16 shows the von Mises stresses in the stub sill substructure with an embedded surface crack under a vertical coupler load. The figure shows the refined local mesh in the area around the surface crack.

4.2.3 SIFs for Embedded Cracks

Through Cracks. For each embedded through crack model, J integral values were computed using the domain integration utility in ABAQUS and converted to SIFs ($J = K_I^2/E'$, where $E' = E$ for plane stress and $E' = E/(1-\nu^2)$ for plane strain). The average of the plane strain and plane stress values was used.

Because the remote stress field varies through the thickness of the top plate, the SIFs at the tips of the through cracks also vary through the thickness. The SIFs are larger at the top surface; they are also larger at the head brace corner than at the center of the sill.

Figure 17 shows the SIFs at the top surface of the sill top plate for through cracks for a 100 kip vertical coupler load. Figure 18 shows the variation of SIFs through the thickness of the sill top plate as the through cracks grow.

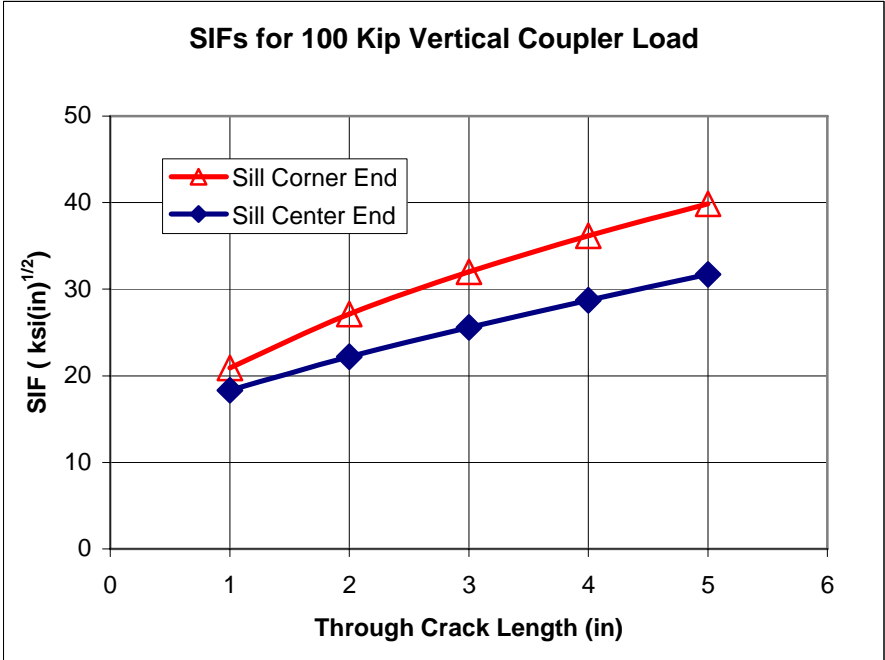


Figure 17. SIFs for stub sill substructure with embedded through cracks (from 1-in to 5-in long) in sill top plate. Vertical coupler load = 100 kips.

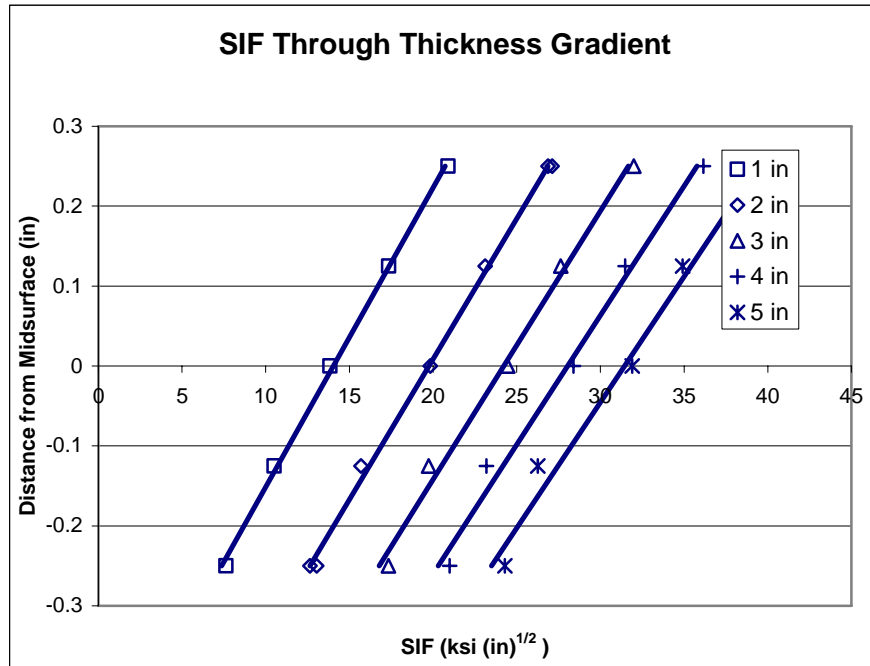


Figure 18. Through thickness distribution of SIFs for stub sill substructure with embedded through cracks in sill top plate. Vertical coupler load = 100 kips. Crack lengths vary from 1 in to 5 in.

In NASGRO, the mean (through thickness) values are used to drive the through crack growth. The same assumption is used here to calculate crack growth rates.

Surface Cracks. For each embedded surface crack model, J integral values are again computed using the domain integration utility in ABAQUS and converted to SIFs as with the through cracks. Figure 19(a) shows the FE SIF K_a at crack tip a (see Figure 6) for each crack depth along the predetermined trajectories (Table 1) for initial crack lengths $2c_i/T = 0.25, 0.50, \text{ and } 1.0$ (i.e., 0.125 in, 0.25 in, and 0.50 in). Figure 19(b) shows the FE SIF K_c at the crack tip on the surface (Crack Tip c, Figure 6) for each crack depth along the predetermined trajectories for the same range of initial crack lengths $2c_i/T$.

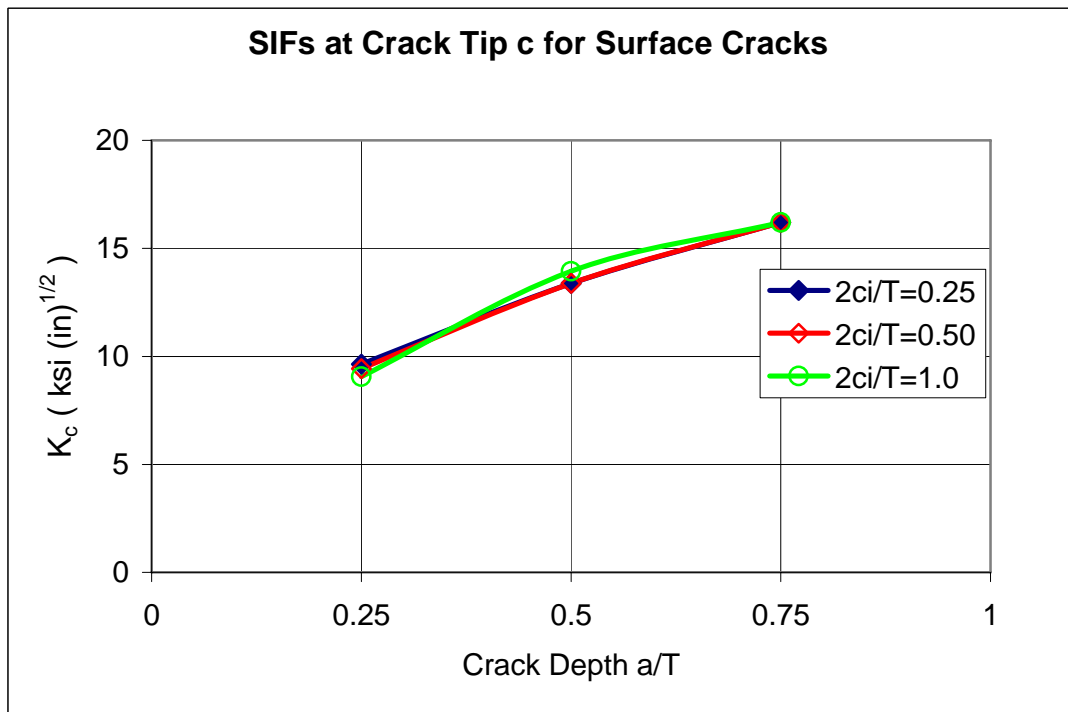
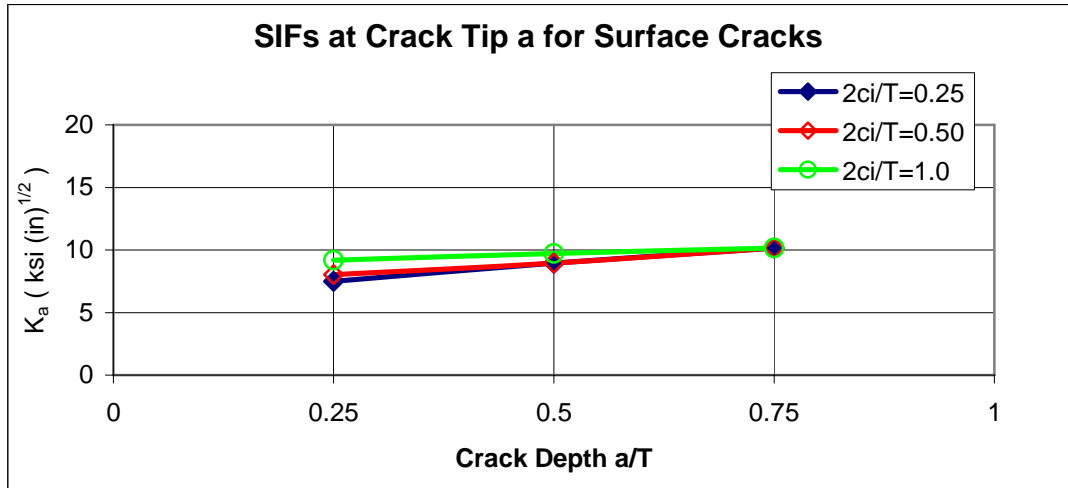


Figure 19. SIFs for stub sill substructure with embedded surface cracks in sill top plate. Vertical coupler load = 100 kips.

Of course, in the FE model with embedded surface cracks, the SIFs will, in general, be different at the two surface locations (higher at the corner, lower at the crack tip nearer the sill top plate center line). In the current DTA procedure, the crack is assumed to grow symmetrically. Therefore, in the simulations reported here, the higher of the two surface SIFs calculated from the FE embedded crack model is reported and used in the subsequent crack growth calculations.

Comparison of FE Stress Intensity Factors with Raju Newman SIFs. For an initial crack size $2c_i/T = 0.25$ (i.e., an 1/8-in crack), Figures 20(a) and 20(b) compare the SIFs K_a and K_c over the full range of crack surface lengths $2c/T$ from surface to through crack, determined by FE analysis of the cracked stub sill substructure with the corresponding values computed according to the Raju Newman solution [4,5] using the hot spot stress distribution

Even when the crack is only quarter-through, the Raju Newman SIF K_a is about 1.24 times the embedded FE SIF, which leads to much more rapid growth of the surface crack (about twice as fast), because the SIF is raised to a power of 3.15 in the current version of the Paris Law used in DTA. This is a strong indication that even when the surface crack is still quite small, the Raju Newman/hot spot stress approach is likely to be very conservative.

The apparent inaccuracy of the Raju Newman SIF values is not a problem with the Raju Newman solution per se, even though it is admittedly an approximate curve fit. Rather the inaccuracy results from its use in combination with the hot spot stress distribution for the uncracked structure.

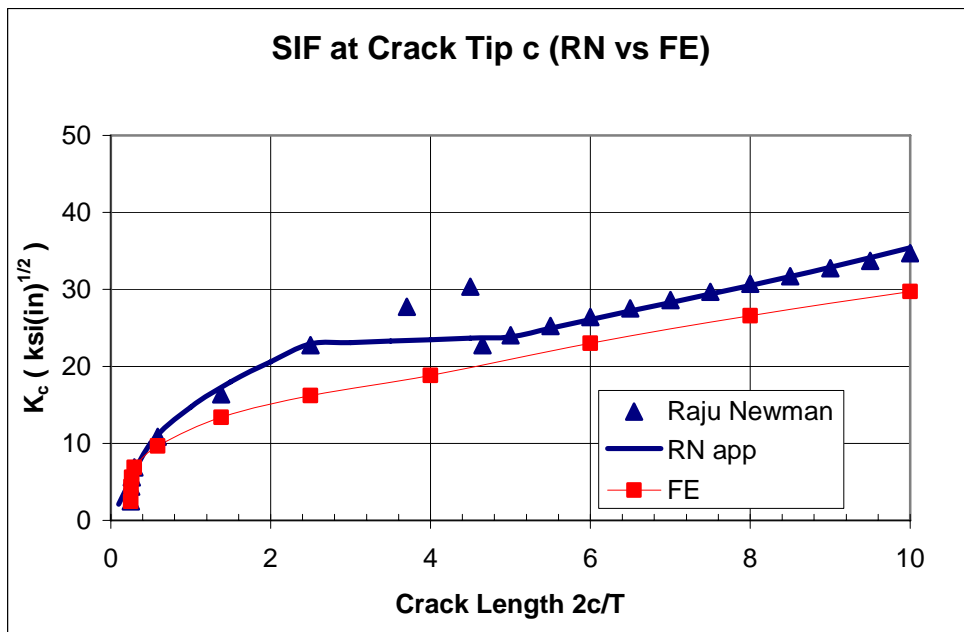
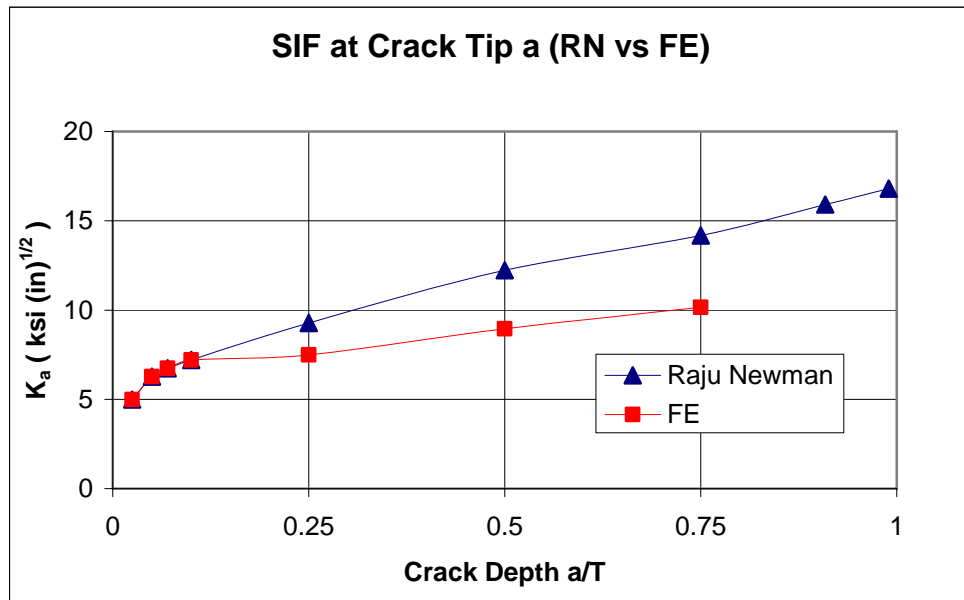


Figure 20. SIFs (FE and Raju Newman [4,5]) for stub sill substructure over full range from surface to through crack regime. Vertical coupler load = 100 kips. Discontinuity exists between Raju Newman surface crack SIF and through crack SIF at Crack Tip c when crack breaks through.

4.2.4 Equivalent Far Field Stresses on Growing Through Cracks: Interpretation of Load Redistribution Effects

One way of interpreting the reduction in the general stress level acting on the through crack as it grows is to convert the computed SIFs to equivalent far field stresses that would produce those SIFs. This was done by simply calculating an equivalent stress $\sigma = K / (\pi c)^{1/2}$ (where c is the half-length of the through crack) at each location through the thickness. From these equivalent stress values, a mean stress σ_m , a bending stress σ_b , and an equivalent DOB were computed. This interpretation of the data in terms of equivalent far field stresses provides insight into the effect of the growing crack on the local stress redistribution in the sill top plate.

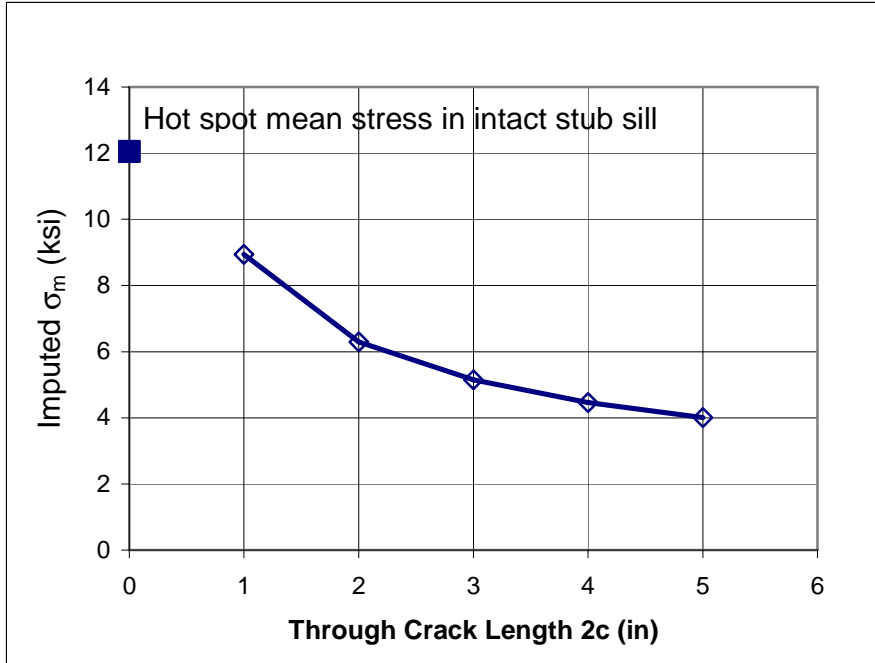
Figure 21(a) shows the reduction of mean equivalent stress as the through crack grows. The figure also shows the hot spot mean stress in the intact stub sill. Figure 21(b) shows the same data, normalized by the hot spot mean stress.

Figure 22 shows the DOB computed from these equivalent far field stresses. The DOB reduces as the crack grows, but it does not completely disappear as assumed in NASGRO.

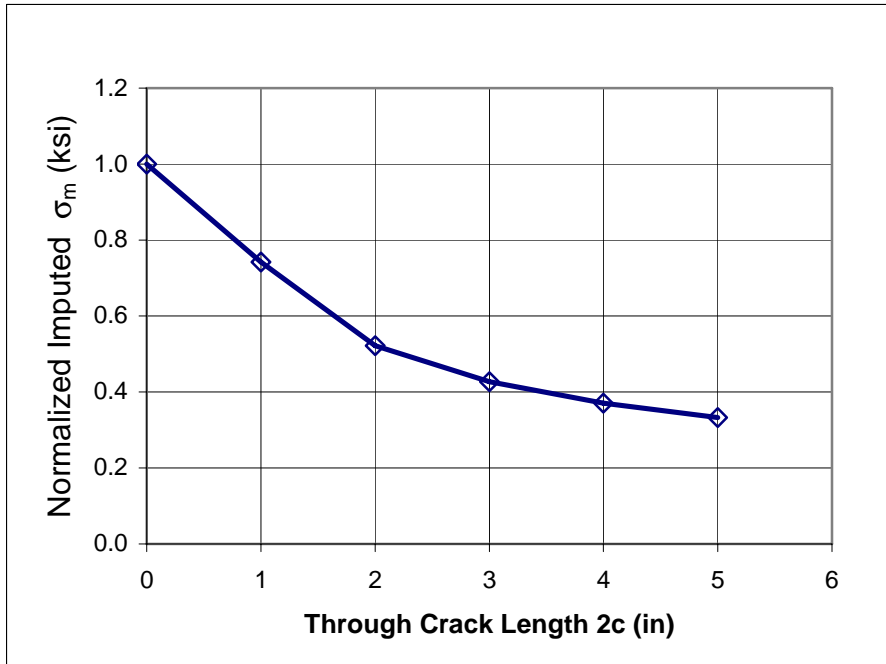
In the current DTA procedure, at breakthrough the surface crack is assumed to instantaneously transition to a through crack with vertical crack fronts and to continue growing with vertical crack fronts. As a result, the original hot spot mean stress is used to drive through crack growth in NASGRO. It is obvious from these results that the bending effect does not actually disappear (though it does reduce) even for a through crack with initially vertical crack fronts. The growth rates would, as a result, be different at different locations through the thickness of the plate (faster at the top surface), and the crack fronts would not be likely to remain vertical.

4.2.5 Plasticity Effects and Elastic T-Stress

Apparent fracture toughness. As has been mentioned already, it has been known for some time that apparent fracture toughness is affected by the degree to which plastic deformation at the crack tip is confined in a test specimen. Thus a compact tension specimen has a lower apparent fracture toughness than a thin plate with a central crack. For a given material, the actual critical crack length would be smaller for the compact specimen than for the plate. This effect is often termed constraint, and it can be characterized in several different ways. For the purposes of the Level 2 procedures, the elastic T-stress is a convenient way of doing so. The T-stress is simply the stress acting parallel to the crack surface, and it can be easily determined in the course of the elastic FE (with embedded crack) stress analyses of the tank car.



21(a). Equivalent far field mean stress σ_m as through crack grows in stub sill.



21(b). Normalized equivalent far field mean stress σ_m as through crack grows in stub sill.

Figure 21. Change in crack stress regime as through crack grows in stub sill top plate. Equivalent means stress σ_m calculated from computed SIFs. Vertical coupler load = 100 kips. Crack lengths vary from 1 in to 5 in.

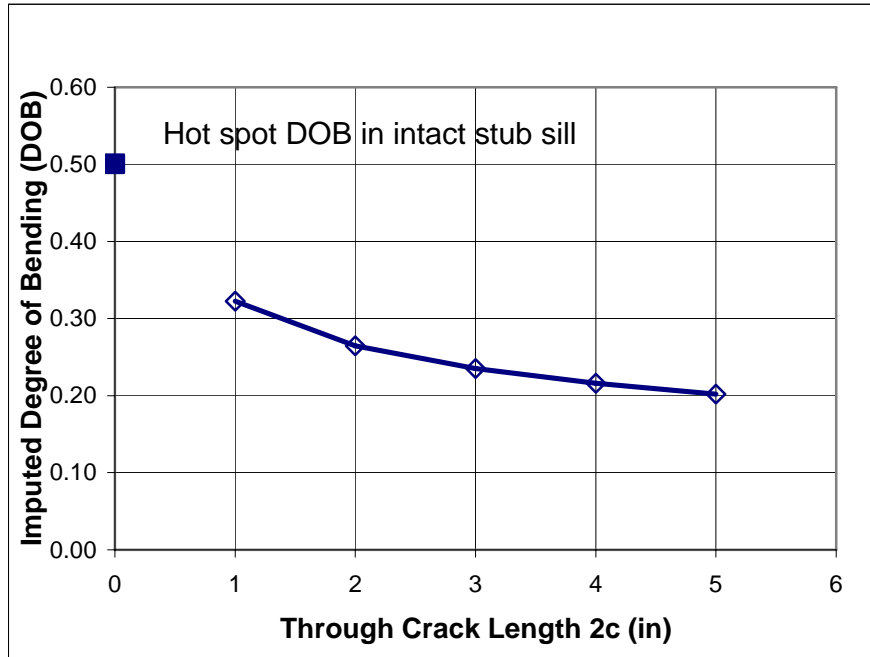


Figure 22. Equivalent far field DOB in stub sill substructure with embedded through cracks in sill top plate. Calculated from computed SIFs. Vertical coupler load = 100 kips. Crack lengths vary from 1 in to 5 in.

Crack growth rate. Crack-tip plasticity effects are ignored in the current Level 1 procedure. Significant crack-tip plastic deformation means that a certain level of tensile stress (the opening stress S_{op}) must be applied to the crack before it opens on ensuing cycles. Thus the effective SIF ΔK is reduced, leading to slower crack growth than predicted by the simple Paris Law. McClung [6] reviewed and analyzed biaxial test data on cruciform specimens (Figure 23) of austenitic stainless steel, low-carbon structural steel, and a high-strength steel (HY100). The data show higher Mode I crack growth rates (Figure 24 (top)) when a compressive (biaxial) stress acts parallel to the crack and lower growth rates when a tensile stress (biaxial) acts parallel to the crack. It appears that these different growth rates are due to differences (caused by stress biaxiality) in crack closure behavior arising from plasticity effects (Figure 25). At least approximately, the different growth rates might be accounted for by recognition of crack opening stress in an effective SIF ΔK_{eff} for use in the crack growth model. McClung [6] used a detailed elastoplastic FE simulation of incremental crack growth to determine opening stress levels as a function of S_{max}/σ_0 (Figure 25) for three different biaxiality ratios λ (as defined in Figure 23). He found that for reasonably high applied cyclic stress levels ($S_{max}/\sigma_0 > 0.4$), the opening stress level was sensitive to biaxiality ratio (or equivalently, elastic T-stress). When these opening stress levels were used to determine ΔK_{eff} values, the experimental growth rate curves for the different biaxiality ratios showed much better agreement (Figure 24 (bottom)). If this simple correction fully captured the effect of stress biaxiality, however, all the crack growth curves would collapse into a single curve in Figure 24 (bottom).

A comprehensive series of elastoplastic FE analyses of straight and deflected through cracks, with modeling of crack surface contact, and with $DOB = 0$ (i.e., no through thickness stress gradient) were carried out to quantify crack closure effects. Some of these results have been reported in a journal article (*Finite Element Modeling of Fatigue Crack Closure in Inclined and Deflected Cracks*, by S. Kibey, H. Sehitoglu, and D. Pecknold, *International Journal of Fracture*) [7].

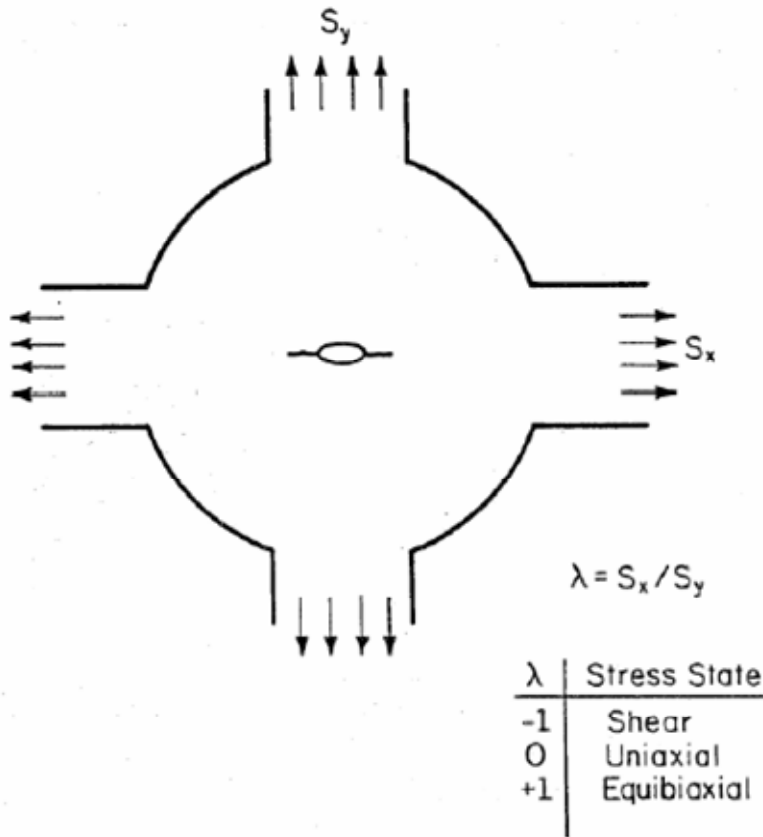


Figure 23. Schematic representation of a cruciform specimen for biaxial fatigue testing (after McClung [6]).

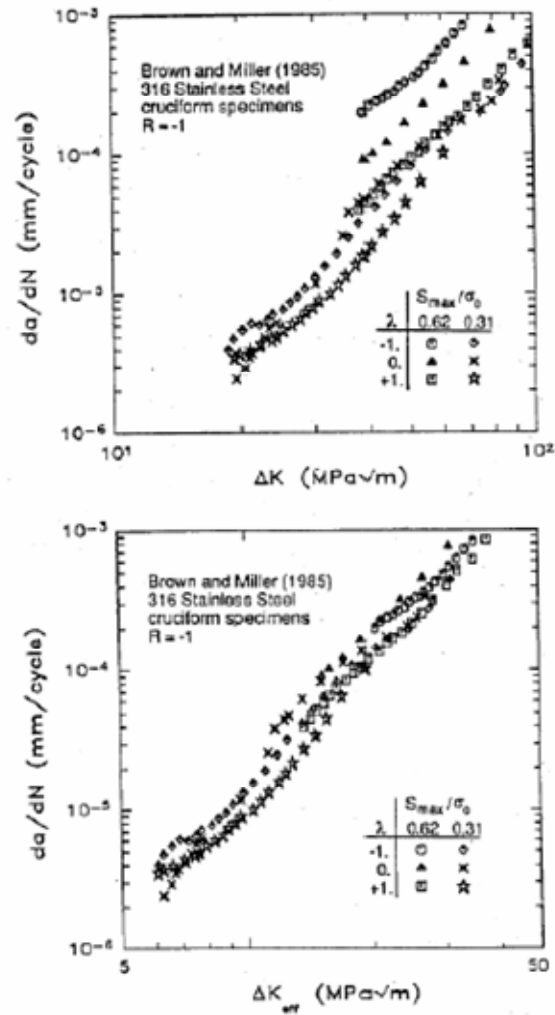


Figure 24. Crack growth rates for different biaxiality ratios and maximum stresses based on data of Brown and Miller for a 304 Stainless Steel (after McClung [6]). Top correlates with ΔK ; bottom correlates with ΔK_{eff} .

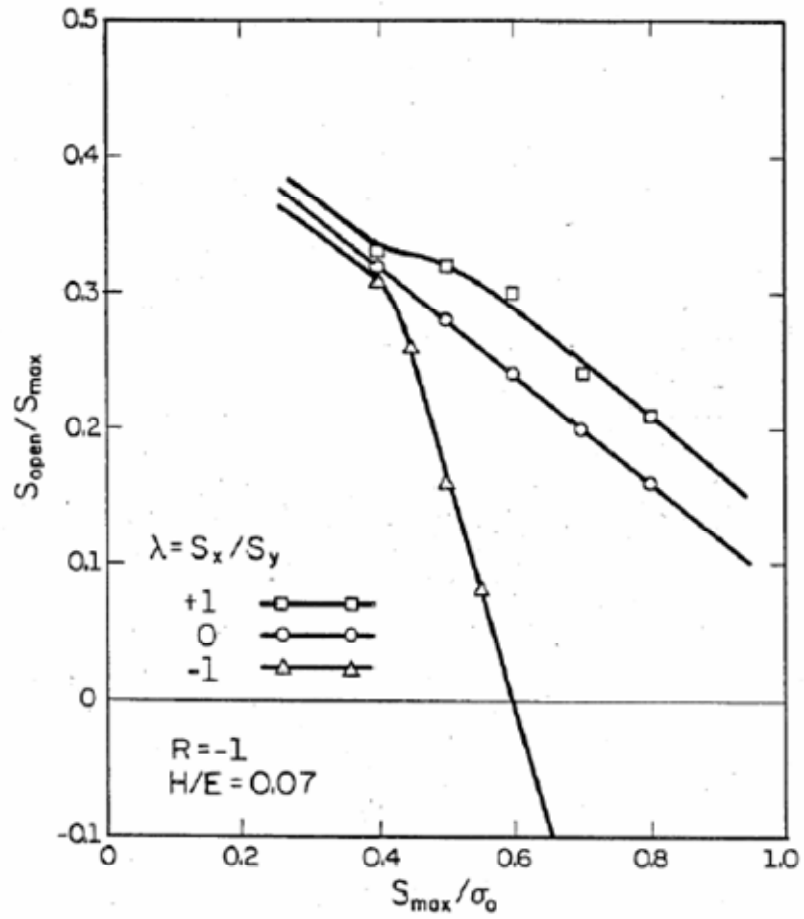


Figure 25. Normalized crack opening stresses as a function of maximum stress for three different biaxiality ratios (after McClung [6]).

5. Sample Fatigue Life Calculations for Level 2a Procedure

The SIFs that were determined from the series of FE analyses of the stub sill substructure with embedded surface cracks and through cracks were used to carry out crack growth calculations for a repeated 100 kip ($R = 0$) vertical coupler load. Similar calculations were carried out using the Raju Newman SIFs [45,46] contained in NASGRO for comparative purposes. The basic Paris Law relation ($da/dN = C(\Delta K)^n$) (i.e., without crack closure) was used to describe crack growth in both cases.

5.1 Crack Growth Comparisons: DTA versus Level 2a Procedure

For very shallow surface cracks, the Raju Newman empirical relation [45,46] should be reasonably accurate, so it can be used to provide SIFs for the embedded FE procedure at small values of a/T . In this sample fatigue life calculation, the Raju Newman SIFs were used in the range $0 < a/T < 0.25$.

Figure 19 shows the SIFs at the a-tip and the c-tip as a function of a/T , in the surface crack regime. As the depth a/T increases, the shape of the crack varies continuously according to the crack trajectory shown in Figure 9. After the surface crack breaks through, it is assumed to grow symmetrically as a through crack with vertical faces. Although the actual through thickness gradient of the SIFs (Figure 18) shows that this is unlikely, it is the same simplifying approximation that is used in NASGRO. Figure 20 shows the SIFs in the through crack regime, as a function of crack length $2c/T$.

The Paris Law $da/dN = C(\Delta K)^n$ with no crack closure modifications was used to compute the crack growth curves for the current DTA and the proposed Level 2a procedure. The following parameters were used:

Table 2. Parameters for sample fatigue lift calculations.

Paris Law Parameters	n	3.15
	C	5.81×10^{-10}
Initial Crack Size		
Length $2c_i/T$	0.25	($2c_i = 0.125$ in)
Shape a_i/c_i	0.20	
Depth a_i/T	0.025	($a_i = 0.0125$ in)

Figure 26 shows the resulting crack growth responses for the current DTA and the proposed Level 2a procedure. The predicted fatigue life according to the proposed procedure is 1.67 times longer than that predicted using the Raju Newman SIFs [4,5] contained in NASGRO.

An additional increase in predicted fatigue life can be expected if crack closure effects are accounted for in the crack growth law (as proposed in the Level 2b procedure). These two suggested modifications to the current DTA procedure can be implemented independently. The embedded FE modeling can be used without improvements in the crack growth law, as in the sample fatigue life calculation reported here. Equally, a modified crack growth law can be incorporated into the current procedure without using FE embedded crack models.

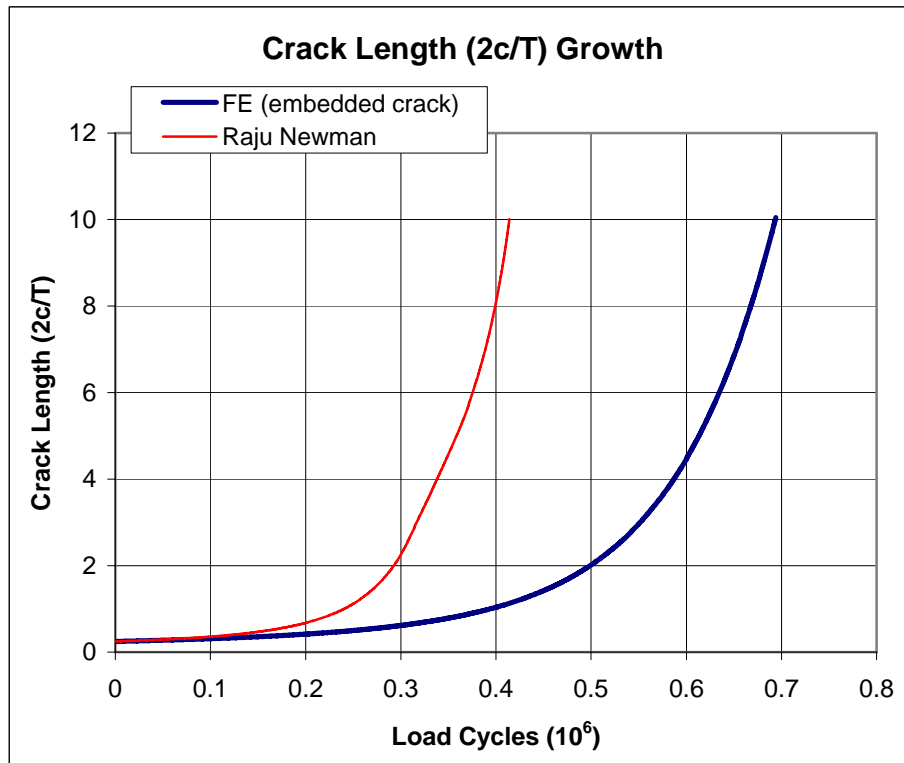


Figure 26. Crack growth curves for stub sill substructure under repeated 100 kip vertical coupler load ($R = 0$). Comparison between current DTA and proposed procedure. Both use the same Paris Law for crack growth.

6. FE Study on Plasticity and Crack Closure Effects for Through Cracks

It has been well established that fatigue crack closure significantly affects the growth rate of fatigue cracks in metals. If the phenomenon of crack closure and its consequences on fatigue crack propagation are neglected, the predicted crack growth rates might significantly deviate from the actual rates in the components in service. Crack closure models have been widely accepted as the most accurate means of analytically determining crack growth rates in metals subjected to constant or variable amplitude fatigue loading.

This section examines closure effects for straight cracks, inclined cracks, and deflected cracks (the Appendix presents the complete study, but this section summarizes it).

Section 7.5 examines closure effects for a curved crack for the following reasons. As is evident in Figures 2 and 11, the hot spot in the sill top plate for vertical coupler loading is located on the curved segment of the head brace footprint. All of the fatigue crack growth modeling, including the proposed UIUC procedure, as well as the current DTA procedure, contemplates only planar fatigue cracks, whether they be surface or through cracks.

The significant question as to whether a fatigue crack initiating at the hot spot will tend to grow around the curve and extend further parallel to the longitudinal axis of the sill has not been previously addressed. The elastoplastic FE studies reported here provide significant insight into the growth of deflected (i.e., non-planar) cracks and curved cracks.

6.1 Alternative Crack Growth Models

This section discusses some of the analytical, empirical, or numerical models developed to simulate fatigue crack growth taking into account crack closure phenomenon. The DTA approach suggested by SwRI [8] recommends the use of the NASGRO equation [9] given by:

$$\frac{da}{dN} = C \left[\frac{1-f}{1-R} \Delta K \right]^n \frac{\left(1 - \frac{\Delta K_{th}}{\Delta K} \right)^p}{\left(1 - \frac{K_{max}}{K_c} \right)^q} \quad (1)$$

where f denotes the crack opening function for plasticity induced crack closure (PICC). The parameters p , q , n , and C are fitting parameters. However, owing to the lack of verifiable sets of data to determine these empirical parameters, the SwRI report [8] recommended a simplified version of equation (1) for tank car stub sills, by setting p and q equal to zero and not considering crack closure in analysis ($f=0$). Consequently, the current DTA model recommended for tank cars is given by:

$$\begin{aligned} \frac{da}{dN} &= C(\Delta K)^n \quad \text{for } R \geq 0 \\ \frac{da}{dN} &= CK_{max}^n \quad \text{for } R < 0 \end{aligned} \quad (2)$$

After the discovery of the phenomenon of crack closure by Elber [10], many researchers incorporated fatigue crack closure concepts to predict crack growth rates. Bell and Wolfman [11] developed a mathematical model to determine the crack opening stress in order to correlate the predicted crack growth behavior to observed behavior for several simple loading spectra. Their model was incorporated into the Air Force crack growth computer program CRACKS II. De Koning [12] developed an empirical crack closure model accounting for load interaction effects and constraint effects (plane stress, plane strain, etc), used to predict effects of crack acceleration and retardation under variable amplitude loading. This empirical model is fundamentally a modification of Dugdale's strip yield model [13] and forms the basis of the computer program CORPUS used by the National Aerospace Laboratory, NLR, in the Netherlands. A similar computer program ONERA developed by Baudin et al. [14] is also based on an empirical crack closure model. Aliaga et al. [15] suggested a crack closure model designed to predict crack growth rates under short loading spectra. This model forms the basis of computer program PREFAS and can account for the effect of R ratio and retardation effects. It does not, however, take into account the effect of compressive loads, loading history, and variations in the loading history at different crack lengths. The most widely used crack closure model is Newman's model [16]. This model is based on Dugdale's model but modified to incorporate the plastically deformed material in the wake of the fatigue crack. The residual deformation behind the crack tip results in premature closure of the crack faces when the remote load is still tensile, thus reducing the effective load range over which the fatigue crack is open. The reduced effective stress intensity range, ΔK_{eff} , is then used to compute the crack growth rate. The effective stress intensity range, ΔK_{eff} , is defined as:

$$\Delta K_{eff} = (S_{max} - S'_0) \sqrt{a \pi F_j} \quad (3)$$

where S_{max} denotes the maximum applied stress and S'_0 denotes the remote applied stress at which the crack is completely open. Newman expressed the crack opening stress as a function of the stress ratio R , remote stress level S_{max}/σ_0 , and the constraint factor α [17].

$$S'_0 = f\left(R, \frac{S_{max}}{\sigma_0}, \alpha\right) \quad (4)$$

The constraint factor α indicates the state of stress ahead of the crack tip. It is taken as 1 for plane stress and 3 for plane strain. These equations are used in computer code FASTRAN-II to make fatigue crack growth and fatigue life predictions [18] under constant amplitude and variable amplitude loadings. Newman's model takes into account the effect of load ratio R , the loading history for different crack lengths, and the stress state ahead of the crack tip; the model is able to predict short crack and long crack behavior. This model assumes that crack growth data for a given material can be reduced to a single curve for all stress ratios. This is achieved by using different values of α as a fitting parameter to correlate the crack growth rate against ΔK_{eff} for various load ratios.

Another crack growth life prediction computer code is AFGROW developed by Harter [19] in 1999. Similar to FASTRAN, AFGROW also incorporates a crack closure model to determine crack growth rates. The closure model used in AFGROW, however, is significantly different

from Newman's model. Unlike FASTRAN, the closure model in AFGROW does not assume that the crack growth rate for a given material will reduce to a single curve. The opening stress level is determined in AFGROW using a parameter called closure factor C_f , which is defined as:

$$C_f = \frac{K_{op}}{K_{max}} \quad (5)$$

The dependence of C_f on load ratio R is given by:

$$C_f = 1 - [(1 - C_{f0})(1 + 0.6R)(1 - R)]$$

where C_{f0} is the value of C_f at $R = 0$.

The closure factor is used to determine the effective stress intensity range, ΔK_{eff} , which facilitates computation of the crack growth rate. A comparison of the fatigue life predicting capabilities of FASTRAN- II and AFGROW is made in [20].

The National Aeronautical & Space Administration's fatigue crack growth computer program NASGRO [9, 21] incorporates several retardation models which account for the effects of overloads. The Generalized Willenborg model deals with the retardation effect of overloads by using an effective stress ratio, R_{eff} , instead of an actual stress ratio within the crack growth equation. The effective stress intensity ratio is defined as:

$$R_{eff} = \frac{K_{min} - K_R}{K_{max} - K_R} \quad (6)$$

where K_R is the residual stress intensity.

The Walker-Chang Willenborg model [21] is a modification of the Generalized Willenborg model, by taking into account the acceleration of a fatigue crack due to negative loads. Reference [22] contains details of this model. In addition to these models, NASGRO includes a strip yield model based on Newman's model that accounts for the effects of PICC on crack growth rates. The implementation of this model is similar to that in FASTRAN-II. The crack-opening stress is expressed as a function of R ratio, load ratio, and constraint factor, as given in equation (4). The curve-fits for crack opening stress are obtained from experimental data or FE analyses for constant amplitude loadings. Based on these curve fits, it is possible to collapse the crack growth data as a function of ΔK_{eff} to a single curve for various load ratios. This model is therefore able to predict the effect of stress level and load ratio on crack growth rate, but it cannot account for the retardation or acceleration effects due to overloads or underloads.

The fatigue crack growth prediction codes and the associated crack closure models discussed above fundamentally assume PICC as the only mechanism of closure. These models ignore the role of other known closure mechanisms like roughness induced crack closure (RICC), oxide induced crack closure, and transformation induced crack closure. RICC arises in situations when the roughness of the crack surface is comparable to the crack opening displacements and where

significant Mode II displacements occur. Cracks growing in near threshold regime in planer slip materials and coarse-grained materials are likely to have micro-level non-flat surfaces; and the growth behavior of such cracks is influenced by the contact interaction and relative sliding between faces. RICC is the dominant closure mechanism in such fatigue cracks. Suresh [23] proposed a geometric model for closure resulting from crack surface roughness. Llorca [24] developed a finite difference model to investigate the interaction between rough crack surfaces and the effect of crack deflection on the extent of RICC in fatigue cracks. These models, however, ignore the effect of plasticity and friction on crack closure. Sehitoglu et al. [25, 26] developed a model for RICC by incorporating statistical descriptions of the asperities. Crack opening stresses were determined by analyzing the interaction between rough fracture surfaces using contact mechanics principles, and the dependence of crack opening stress on surface roughness, R ratio, asperity density, shake down pressure (which reflects effect of friction), stress level, and crack length was established.

Another closure mechanism of interest and relevance is sliding mode crack closure (SMCC) [27], typically observed in mixed-mode propagation of fatigue cracks. Fatigue cracks growing under mixed-mode conditions remain closed for a significant part of the fatigue cycle (in contrast to Mode I), but the crack faces undergo relative sliding, leading to a reduction in the nominal SIF due to friction and abrasion under mixed-mode conditions. This effect is termed as SMCC. Carlson and Beevers [28] suggested an analytical model for fatigue crack closure under mixed-mode (Mode I + II) conditions and examined the effect of asperity angle, fraction between contacting crack faces and Mode II displacements on Mode I and Mode II SIFs. This work represented the first attempt to quantify closure under mixed-mode conditions. Brown et al. [29] developed a physical model to quantify SMCC observed cyclic Mode II loading conditions and later extended this model to SMCC in mixed-mode (I+II) loading conditions [30], with dominantly Mode II conditions. They used this model to explain the near threshold fatigue crack propagation behavior of structural steels under mixed-mode conditions.

It is essential to investigate and understand the fatigue crack closure behavior of cracks growing under mixed-mode conditions, which in turn will facilitate more accurate predictions of crack growth rates. It is important to realize that the closure models available in NASGRO fail to account for important retardation factors like crack path deflection, effect of friction and contact interaction between crack surfaces, and closure resulting from these factors. Further work needs to be done to improve understanding of the role played by PICC and SMCC in fatigue crack growth rates under mixed-mode conditions.

In recent years, much emphasis has been placed on FE modeling to investigate closure in fatigue cracks. The previous research at UIUC on fatigue crack closure carried out by Sehitoglu et al. used a specialized code that was initially developed by Lalor and Sehitoglu [31], subsequently modified by Sehitoglu and McClung [32, 33], and further modified by Kadioglu, Sehitoglu, and Gall [34]. This elastic-plastic FE model assumes crack plane symmetry and therefore cannot be extended to model crack deflection and closure arising out of it.

The current research examines crack closure in slanted and deflected through cracks. The objective is to gain more insight into the effect of non-planar crack geometry on premature crack face contact and its consequences on crack growth rates. Slanted and deflected cracks are

allowed to propagate under local mixed-mode conditions when subjected to remote Mode I cyclic loading. The resulting closure is due to a combination of PICC and sliding occurring due to the tangential sliding between crack faces as the crack propagates. Consequently, the effects of crack geometry, friction, and contact interaction between crack faces, stress level, and R ratio on crack opening levels is investigated.

6.2 FE Models of Slanted and Deflected Through Cracks

A two-dimensional elastic-plastic FE model has been developed using ABAQUS [35] to analyze fatigue crack closure in cracks that deviate from their original path. The phenomenon of closure in such cracks involves not only the PICC mechanism but also the relative sliding between the crack faces and the frictional effects arising out of such relative sliding. Thus, it becomes essential to incorporate the effect of both plasticity and frictional nonlinearities on closure behavior of a fatigue crack. Fatigue cracks, in general, can start growing in a particular direction and then deflect to grow in a different direction. This research refers to such cracks as deflected cracks. It is also possible that some fatigue cracks may grow at an angle relative to the remote load. The research team uses the term slanted crack or inclined cracks to describe these cracks. Figure 27 illustrates a slanted and a deflected crack subjected to Mode I remote loading but which exhibits local mixed-mode behavior.

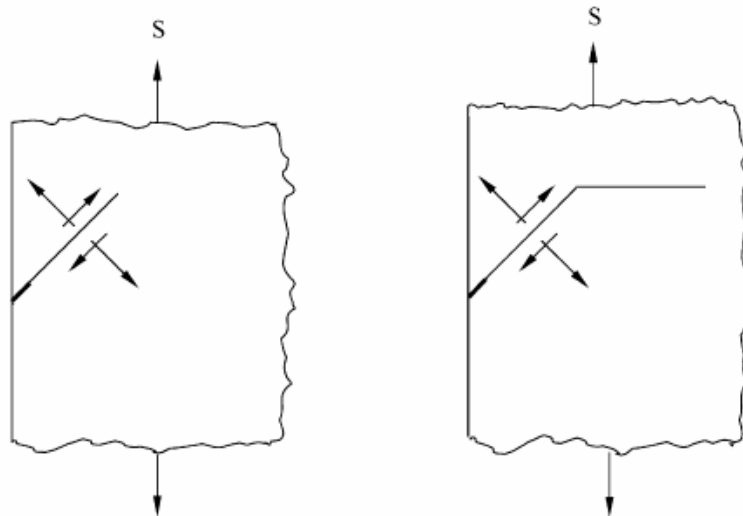


Figure 27. Slanted crack (left) and deflected crack (right).

The material is modeled to follow a bilinear stress-strain relationship. It exhibits linear elasticity below its initial yield strength $\sigma_0 = 480$ MPa. Young's Modulus is assumed to be $E = 200$ GPa, and Poisson's ratio is assumed to be $\nu = 0.30$. The material follows the von Mises yield criterion with linear kinematic hardening to capture the Bauschinger effect associated with reversed yielding. The hardening modulus H is assumed to be constant equal to $0.01E$, which is typical of low hardening steels and several aluminum alloys. Plane stress conditions have been assumed. Closure results for straight cracks under plane strain conditions have been reported elsewhere

[36, 37]. Hence, this research does not consider plane strain conditions in any of the FE simulations.

The extent of closure occurring in fatigue cracks can be quantified with ΔK_{eff} , and the dependence of ΔK_{eff} on various parameters can be expressed as:

$$\Delta K_{eff} = f\left(\frac{S_{max}}{\sigma_0}, R, \frac{H}{E}, \frac{\bar{\sigma}}{\sigma_H}, \mu, a, \text{Geometry}, \text{Microstructure}, \text{constraint}\right) \quad (7)$$

This study investigates the effect of applied stress S_{max} / σ_0 on the closure behavior of slanted and deflected fatigue cracks. The term geometry in equation (7) implies both geometry of the specimen (single edge notch tension (SENT), compact tension (CT), etc.) and the geometry of the crack (crack orientation and crack path). The research specifically addresses the latter (i.e., the effect of crack orientation and crack path on crack closure). This is achieved by investigating the crack closure behavior of slanted and deflected cracks with certain predetermined orientations. The R-ratio effect is investigated by considering two different R ratios: $R = 0$ and $R = -1$. Further, the effect of friction (μ) on crack closure is incorporated in the analysis by accounting for friction between the crack faces in the FE model.

6.3 Closure Behavior of Slanted and Deflected Cracks: FE Results

The following sections present the results for crack opening behavior based on FE analyses. The effect of the following parameters on stable crack opening levels are considered: applied stress level S_{max} / σ_0 , load ratio R , crack orientation relative to the applied loading θ , crack path deflection, and friction μ between crack faces. The following sections also examine Mode I crack opening levels for SENT specimens with edge cracks subjected to constant amplitude fatigue loading.

The Appendix gives comprehensive results involving interactions with Mode II behavior (crack sliding).

Kibey et al. [7] gives the details of mesh development, crack advance scheme, and mesh refinements; these are not repeated here. As mentioned previously, an important objective of this research is to examine the effect of crack orientation and crack path on PICC. To this end, the following specimen geometries were considered.

6.3.1 SENT Specimen Geometries

Geometry 1: A SENT specimen with an initial edge crack inclined at an angle of 45° to the direction of applied loading in Mode I. The fatigue crack is allowed to propagate along the 45° direction without deviating from its path. This geometry facilitates determination of stable opening levels for a fatigue crack oriented at 45° (Figure 28(a)).

Geometry 2: A SENT specimen with an edge crack inclined at an angle of 45° to the direction of applied loading, which is initially allowed to propagate in the 45° direction long enough to attain stable opening levels, and subsequently allowed to deflect and grow perpendicular to the Mode I

loading (Figure 28 (b)). In other words, Geometry 2 depicts the case of crack deflection after stabilization. The length of the slanted part of the crack exceeds the minimum required crack length to attain stabilization (denoted by L^*).

Geometry 3: A SENT specimen with an edge crack inclined at an angle of 45° to the direction of applied loading, which is initially allowed to propagate in the 45° direction. The crack, however, is allowed to deflect and grow perpendicular to the applied loading before stable opening levels are attained (Figure 28(c)). This is the case of deflection before stabilization. In this case, the length of the slanted part of the crack is less than L^* .

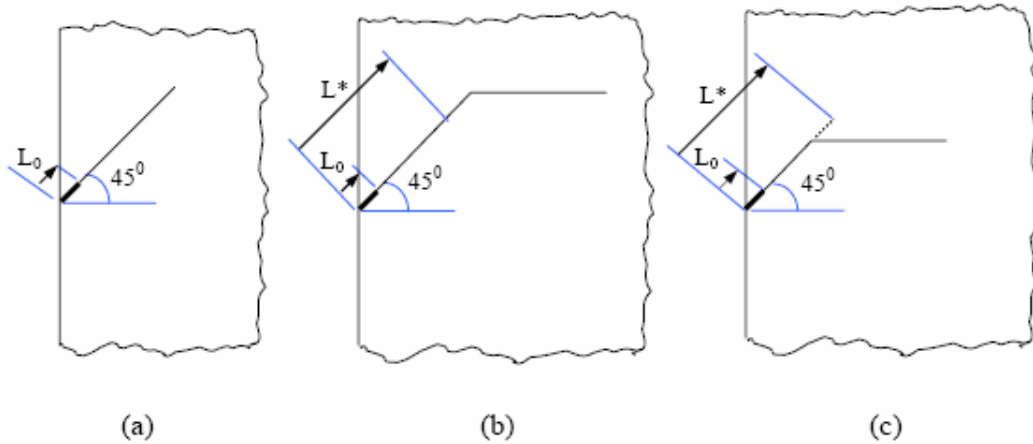


Figure 28. (a) Geometry 1: slanted crack, (b) Geometry 2: crack deflection after stabilization, and (c) Geometry 3: crack deflection before stabilization. (L^* denotes the stabilization crack length.)

While Geometry 1 helps to determine the effect of crack orientation on Mode I and Mode II opening levels, Geometries 2 and 3 provide insight into the effect of crack path on crack opening levels.

6.3.2 Effect of Applied Stress Level S_{max}/σ_0 and R Ratio on Crack Opening Levels

To examine the effect of maximum stress on Mode I opening levels, a SENT specimen with an edge crack oriented at $\theta = 45^\circ$ relative to load direction (Geometry 1) was subjected to constant amplitude fatigue loading with four different stress levels S_{max}/σ_0 : 0.6, 0.7, 0.8, and 0.9. The dependence of opening levels on R ratio was examined by considering two different values of R: 0 and -1. Figure 29 shows the Mode I crack opening level, normalized by maximum applied stress in the cycle, as a function of normalized crack length. Consider the Mode I opening level shown in Figure 29. Normalized opening stress significantly decreases with increasing maximum stress for both $R = 0$ and $R = -1$. This trend in the stable opening levels has been seen in all numerical and analytical models available in the literature. These include the early efforts of Newman [39], Shiratori et al. [40], Fuhring and Seeger [41], and Budiansky and Hutchinson [42]. The later works of Newman [17, 18, 43], Sehitoglu [44], Ibrahim et al. [45], Lalor and Sehitoglu [31], and McClung and Sehitoglu [32, 33] confirmed this phenomenon. Such

dependence of stable opening levels on maximum stress is not obvious. It might be thought that higher applied stress implies higher inelastic deformation in the wake of the crack, which should then result in increased closure—an argument not supported by the results. McClung and Sehitoglu [32, 33] explained this apparent anomaly by comparing the crack opening displacements of the fatigue crack with that of a stationary crack of the same length subjected to the same maximum stress. This comparison gives a first estimate of residual deformations. The fatigue crack opening is seen as a competition between residual deformation and the ideal crack opening displacement at maximum load. McClung and Sehitoglu [32,33] were able to clarify this apparently anomalous behavior. Figure 29 reflects a trend consistent with the above explanation.

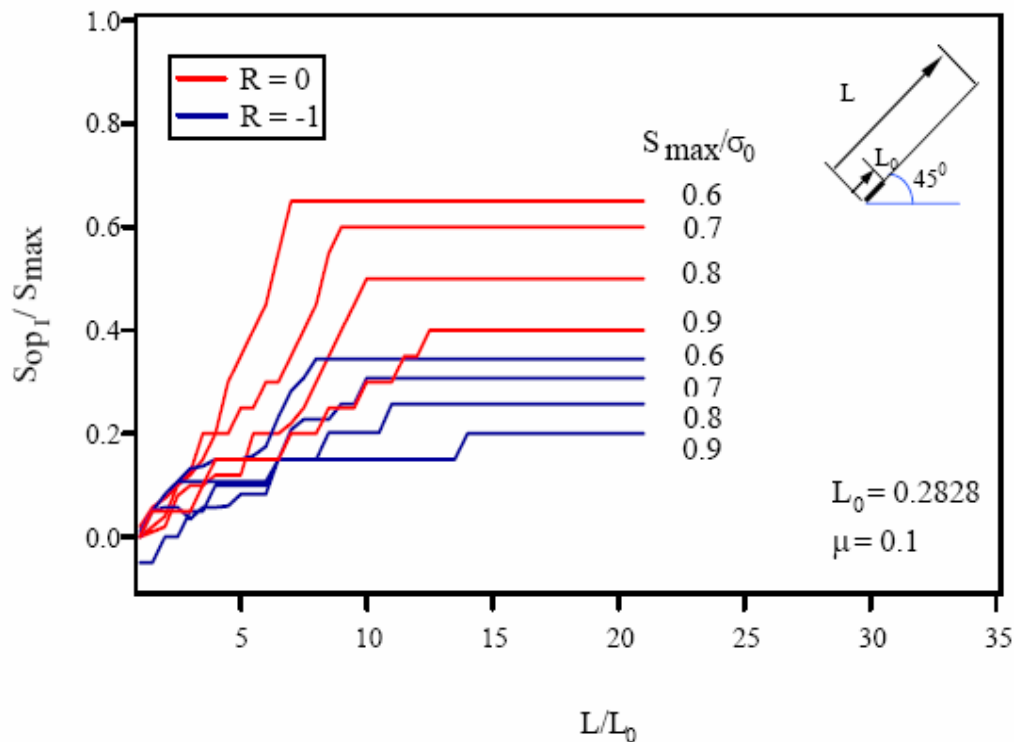


Figure 29. Normalized Mode I opening levels for a 45° slanted fatigue crack for two different R ratios, plane stress (all lengths are in mm).

6.3.3 Effect on Crack Orientation

Figure 30 shows the crack opening levels for two crack orientations: a 45° inclined fatigue crack and a straight crack growing in pure Mode I. It is seen that the stable crack opening level for a 45° slanted crack is significantly higher than that for a straight crack subjected to the same maximum stress. Further, note that the difference in the stable opening level of the two crack geometries increases with increase in maximum stress. Figure 30 clearly suggests that an increase in the crack angle will lead to an increase in the Mode I crack opening level. Similar findings have been reported in the recent past by researchers working on inclined cracks. Wei

and James [46] estimated Mode I crack opening levels for crack angles ranging from 0° to 60° for $R = 0.05$. Their results are in agreement with the trend shown in Figure 30. Parry et al. [47] reported a similar dependence of Mode I opening levels on crack angle, although their research focused on both PICC and RICC.

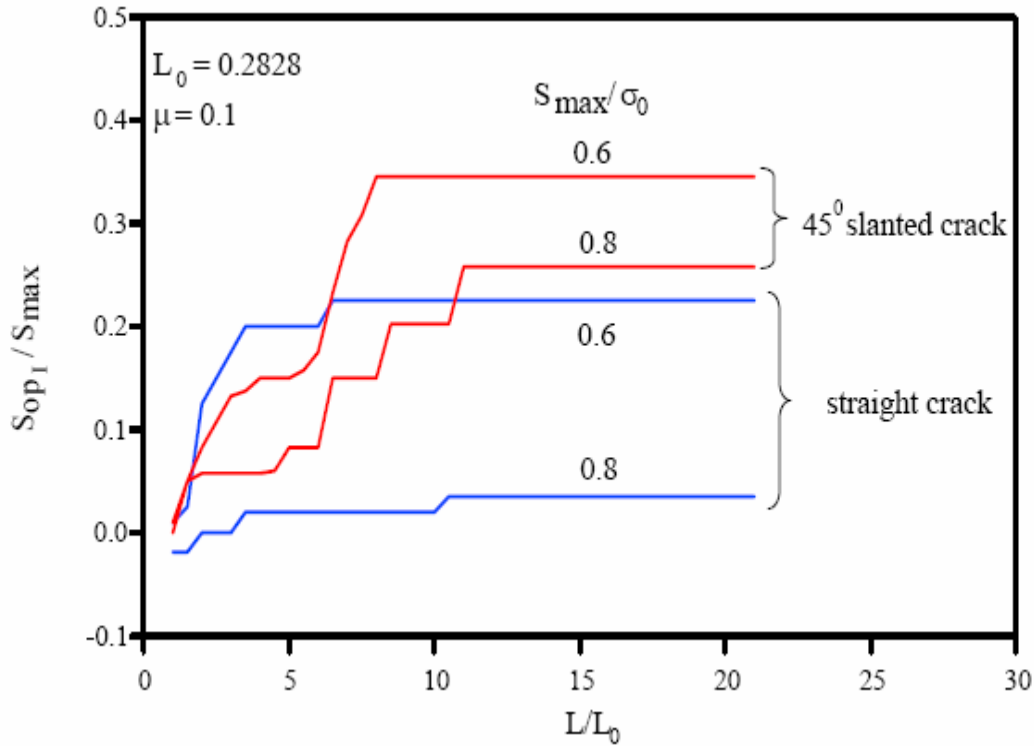


Figure 30. Effect of crack orientation on stable Mode I opening levels $R = -1$, plane stress. L_0 is the initial crack length (all lengths are in mm).

6.3.4 Effect of Crack Deflection

Another important factor influencing the closure behavior of a fatigue crack is crack path deflection. Figure 29 summarizes the stable Mode I opening levels for a 45° slanted crack, which is allowed to propagate along the initial orientation without deflection. A fatigue crack propagating in mixed mode, however, will tend to deflect in order to grow along the preferred plane or direction. It is, therefore, reasonable to expect that the 45° slanted crack considered in the previous sections will, at some point, deflect from its initial orientation and start growing in pure Mode I. This section investigates the effect of such a deflection.

Note from Figure 29 that Mode I opening levels attain a steady state at different fatigue crack lengths depending on the maximum stress and R ratio. Further, for a given R ratio, the crack length required to achieve stable opening levels increases with increase in maximum stress. This phenomenon brings out the following two possible cases of crack deflection:

1. Occurrence of crack deflection after Mode I opening levels attain stabilization.

2. Occurrence of crack deflection before Mode I opening levels attain stabilization.

In order to investigate the above two cases, it is essential to establish a measure of minimum slanted crack length, denoted by L^* , required for stabilization. A logical definition of L^* is the transition crack length corresponding to the highest maximum stress, S_{\max}/σ_0 , used to simulate crack deflection. In deflected crack simulations, two stress levels were considered: $S_{\max}/\sigma_0 = 0.6$ and 0.8 . The transition crack length for $S_{\max}/\sigma_0 = 0.8$ is 3.1 . L^* is assigned this value. The normalized minimum transition length is given by $L^*/L_0 = 11$. Figures 31 and 32 show Mode I opening levels as a function of crack length.

Consider Figure 31 which depicts the case of deflection after stabilization (Geometry 2 in Figure 27). First, note the steep decrease in the Mode I opening levels immediately after deflection. Comparison of Figure 31 with Figure 30 reveals that the final opening level values of the deflected fatigue crack are very close to the opening levels of a pure Mode I straight crack subjected to the same maximum stress. This implies that once the length of the straight portion becomes very large, the deflected crack behaves as a pure Mode I straight crack, and the slanted portion of the crack will no longer play any role in determining the Mode I opening levels. It is not clear from Figure 31, however, if the stable opening level values have been reached for the straight portion of the crack.

A similar trend is seen in Figure 32, which depicts the case of deflection before stabilization (Geometry 3 in Figure 27). Crack deflection results in an immediate drop in the Mode I opening levels. With further increase in the length of the straight portion, opening levels rise steadily and attain stable values. These stable opening level values are in close agreement with the stable opening levels of the pure Mode I straight crack (refer to Figure 30). Thus, it appears that the deflection of a crack before or after stabilization of Mode I opening levels will not affect the final opening level values. Notice that the crack growth rate will accelerate after crack deflection since Mode I opening levels drop steeply in both the cases of crack deflection. Crack growth acceleration, however, will be higher in the case of deflection after stabilization since the crack experiences higher effective stress intensity for this case.

In addition, note that in this case, the crack continues to experience lower Mode I opening stresses (hence higher effective stress intensity) for almost all crack lengths. This implies that the crack growth rates will be the highest for Geometry 2 (deflection after stabilization) once the crack deflects towards the preferred plane of growth.

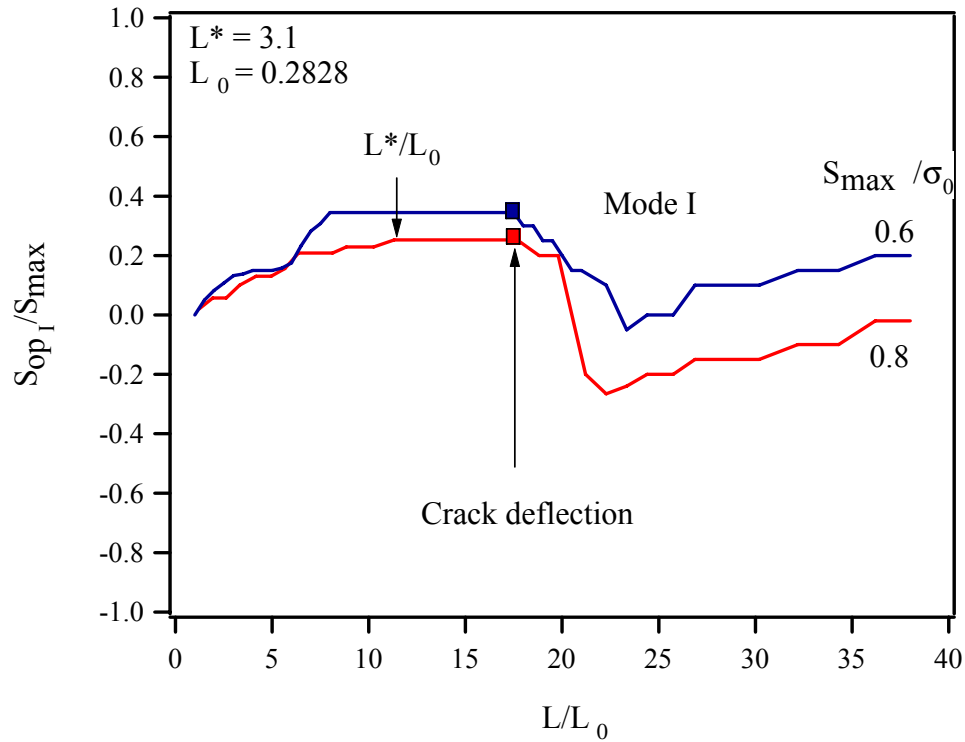


Figure 31. Mode I opening levels for a deflected crack. Deflection occurs after stabilization (all lengths are in mm).

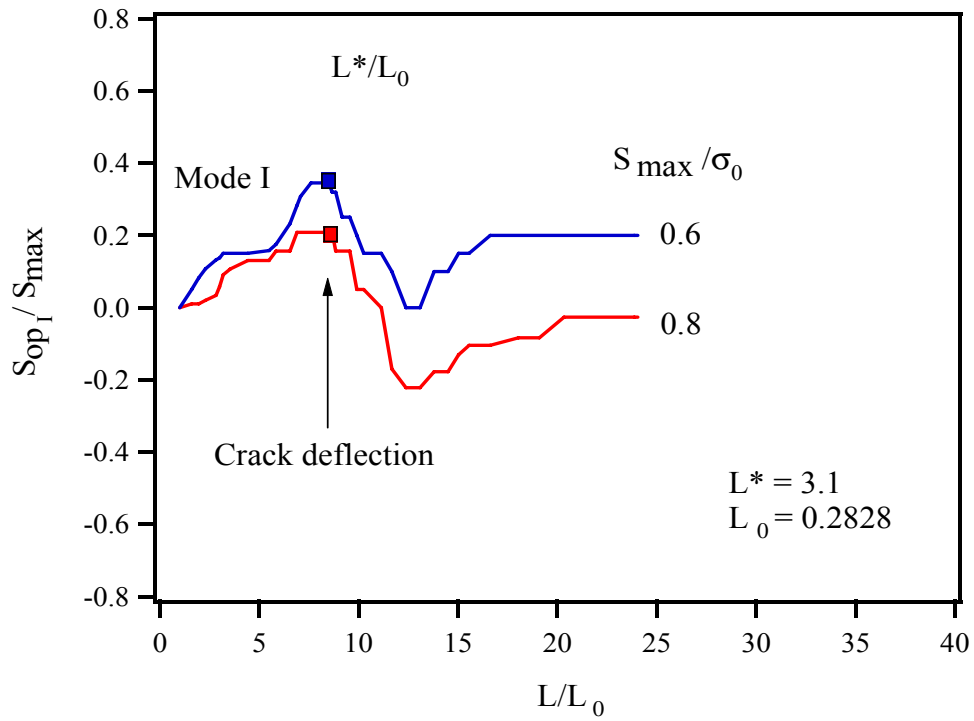


Figure 32. Mode I opening levels for a deflected crack. Deflection occurs before stabilization (all lengths are in mm).

6.3.5 Effect of Friction

It is clear from previous sections that closure behavior of a slanted fatigue crack is significantly affected by crack face interaction, which, in turn, is dependent on the extent of surface roughness of the crack faces. The roughness of the crack faces can be modeled at two levels: micro and macro. Cracks growing in near threshold regime in planar slip materials and coarse-grained materials are likely to have micro-level non-flat surfaces, and the growth behavior of such cracks is influenced by the contact interaction and relative sliding between faces. Micro-level roughness of crack faces can be modeled using a Gaussian or other type of distribution of asperity heights (e.g., ref [25, 26]). In this research, the roughness of the crack faces has been modeled at the macro-level using a Coulomb friction model. The coefficient of friction, μ , can be treated as a measure of roughness of the crack faces. It is then possible to investigate the effect of friction on crack closure by considering different values of μ .

Figure 33 shows the Mode I opening levels for a slanted crack subjected to maximum stress $S_{\max}/\sigma_0 = 0.8$ and two different values of friction coefficient μ : 0.1 and 0.4.

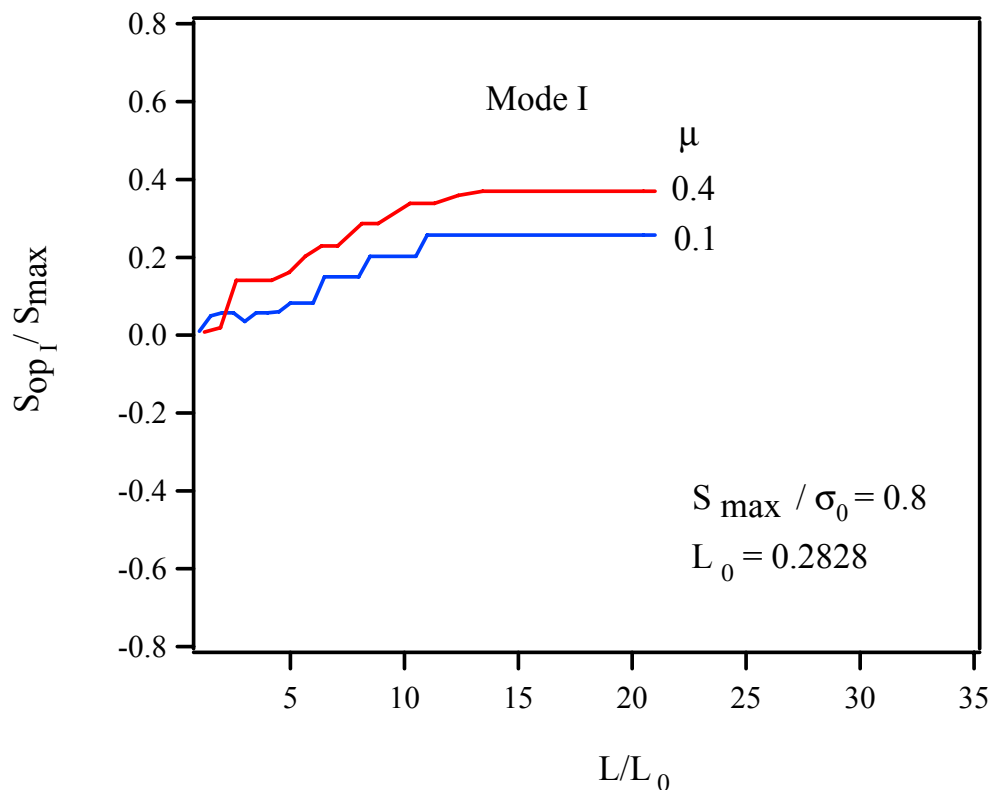


Figure 33. The effect of friction coefficient on opening levels for a 45° slanted crack, plane stress, $R = -1$. Results show that for lower friction coefficients, the crack opening levels are lower (all lengths are in mm).

For smaller crack lengths, an increase in μ has no significant effect on Mode I opening levels, but the final stable opening levels are higher for $\mu = 0.4$. Mode I opening is primarily dependent on the crack tip displacements and the residual deformation in the wake of the crack. Figure 33 suggests a secondary dependence of Mode I opening on friction between the crack faces. A similar dependence of Mode I opening stress on friction coefficient has been reported by Wei and James [46]. Thus, it is seen that increased friction will lead to an increase in Mode I opening levels.

6.4 Development and Improved Crack Growth Model

In the proposed Level 2b procedure, the effect of plastic deformation in the wake of the crack on fatigue crack growth rates is accounted for through modeling of PICC. The above comprehensive, elasto-plastic FE analyses carried out on straight and deflected through cracks with $DOB = 0$ (i.e., no through thickness stress gradients) serve to quantify crack closure effects in these geometries. These elasto-plastic FE simulations provide a measure of the crack opening level, S_{op} , for inclined and deflected cracks. The presence of significant plasticity at the crack tip leads to a premature closure of the crack, resulting in a retardation of the crack growth rate. The incorporation of crack closure in fatigue crack growth laws relies on effective stress intensity range as the driving force for crack growth, and a general law can be given by:

$$da / dN = C(\Delta K_{eff})^m \quad (8)$$

The effective stress intensity range ΔK_{eff} is given by equation (7) and is a function of several variables. In the above FE analyses, the effective stress intensity range has been quantified for inclined and deflected cracks through determination of the crack opening stress S_{op} . The FE results clearly demonstrate that the closure behavior of inclined/deflected cracks is significantly different than that of straight cracks. While only Mode I crack growth is typically observed in straight cracks, inclined or deflected cracks tend to grow in both Mode I and Mode II conditions. FE results reveal that Mode I crack opening levels of slanted cracks are significantly higher than the opening levels of straight cracks. Consequently, crack growth rates for non-planar cracks cannot be realistically estimated from calculations based on straight cracks.

It is also essential to consider the effect of the Mode II component on crack growth rates of slanted cracks. Depending on the R ratio, a slanted crack may exhibit the potential to propagate in Mode II while still being closed in Mode I. For negative R ratios, a slanted crack is likely to undergo complete slip in Mode II before opening in Mode I. In such cases, crack growth is possible in Mode II when the crack is closed in Mode I. For positive R ratios, however, crack opening in Mode I occurs before Mode II displacements can reach the crack tip. In this case, crack growth will essentially occur only after the crack opens in Mode I. The Appendix gives a full explanation of these phenomena.

Finally, it is clear that Mode I crack opening levels of inclined or deflected cracks depend not only on the residual plasticity in the wake but also on friction between the crack faces. This secondary dependence of Mode I crack opening level on friction was not apparent in previous FE

studies, since almost all of the previous models used symmetry and failed to include crack face interactions and the resulting frictional effects in their models.

In summary, a realistic crack growth law for non-planar fatigue cracks must account for closure effects due to plasticity and friction, as well as the effect of crack path deflection. The above elasto-plastic FE analyses do not account for constraint effects. As demonstrated by the studies of McClung and Sehitoglu [33], biaxial stress states can have significant impact on crack closure behavior. Those results indicated that opening stresses, in general, are highest for equibiaxial loading and lowest for pure shear loading in pure Mode I cracks.

Incorporation of both constraint effects and crack closure phenomena in the crack growth laws used in the Level 2b and Level 2c procedures will result in improvement in the accuracy of fatigue life predictive capabilities of these procedures.

6.5 Two-Dimensional Elasto-Plastic FE Analysis of Tank Car Stub Sill Model

This section summarizes the results of ongoing research in modeling fatigue crack propagation in structural steels used for tank car stub sills. The principal goal of such an investigation is to provide input and recommendations for fatigue crack growth modeling in steels used for tank cars. An elastic-plastic FE model was developed to simulate closure in surface cracks found in the stub sill. This section describes the FE model for the stub sill. Results for crack opening levels and effective stress intensity range are given. The Paris law is used to predict crack growth rate from the computed stress intensity range.

6.5.1 FE Model of Stub Sill Substructure Top Plate

Figure 34 shows an FE model of the top flange of the stub sill. A linear elastic FE element analysis of the top flange reveals that the maximum stress concentration occurs at the round corner of the weld toe (hot spot). See also Figure 10(a). An initial crack present at or near the hot spot is subjected to the hot spot stress and is likely to propagate under cyclically varying vertical coupler load. Figure 34 shows a likely path followed by such a fatigue crack near the hot spot. It is possible that a fatigue crack may start to grow towards the hot spot or away from it. It is also possible that the crack may grow in both directions. The crack growth direction depends on the SIFs at the two crack tips. Crack propagation will start at the crack tip with larger SIF.

The mesh was kept at a reasonable density in order to limit the computational burden. A coarse mesh, however, requires a much larger remote stress to ensure that crack tip plasticity can be easily captured and that a reliable estimate of crack opening levels is obtained. In the FE analyses reported below, a rather high level of remote stress $S_{\max}/\sigma_0 = 0.8$ was chosen, much higher than normal hot spot stress levels under vertical coupler loading.

It is emphasized that the objective of this comparative analysis is to evaluate the tendency of a fatigue crack to extend further around the corner from the hot spot versus its tendency to extend in the other direction towards the center of the sill. Predicted SIFs and crack growth rates are

unrealistically high compared to those likely to pertain to actual stub sills under operating conditions.

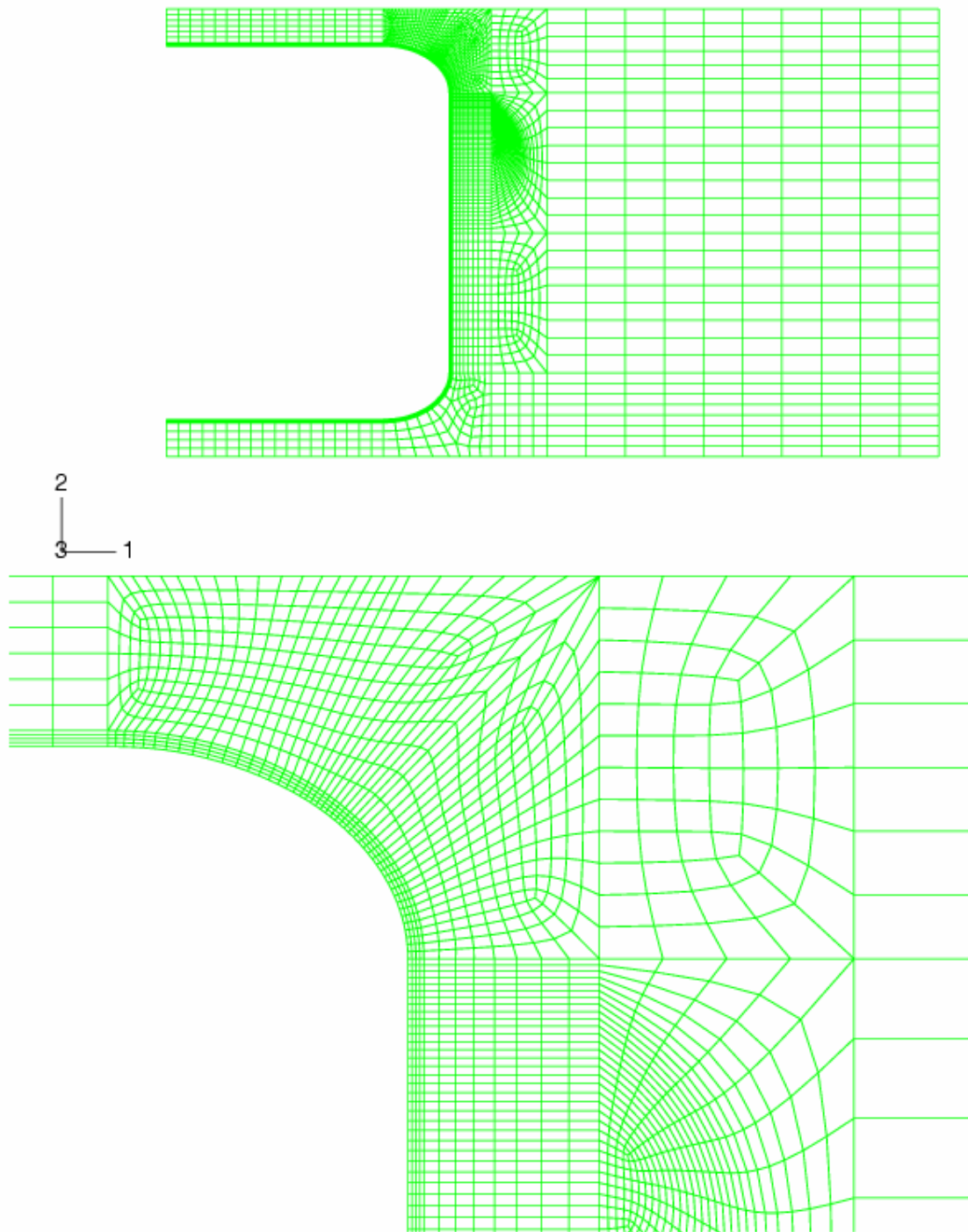


Figure 34. FE mesh for tank car stub sill (all lengths are in mm) A relatively coarse mesh has been used for faster computation, requiring a large remote stress $S_{\max}/\sigma_0 = 0.8$ to ensure that crack tip plasticity is captured accurately for reliable estimates of crack opening levels.

The following material properties were assumed in all FE simulations: initial yield strength $\sigma_0 = 480$ MPa, $E = 200$ GPa, hardening modulus $H = 0.01E$, and Poisson's ratio $\nu = 0.30$. The material follows a von Mises yield criterion with linear kinematic hardening to capture the Bauschinger effect associated with reversed yielding. Plane stress conditions were assumed. The sill flange geometry was subjected to completely reversed Mode I loading. An initial crack of size $L_0 = 5.0$ mm was introduced near the hot spot, and two cases were considered: (a) the crack was allowed to grow away from the hot spot by one element size per cycle and (b) the crack was allowed to grow by one element size per cycle towards the hot spot. Thus, a comparison was made between the crack growth rates for the two possible cases of crack propagation.

6.5.2 FE Results

Figure 35 shows the results of an elastic-plastic FE analysis for a crack growing away from the hot spot. Since significant plastic deformation occurs ahead of the crack tip, the J integral is a more suitable parameter to characterize the stress state ahead of the crack tip.

The J integral is computed at both moving and stationary crack tips for each crack length. Figure 35 shows the variation of J integral with fatigue crack length. The J values increase steadily with crack length at both the crack tips. The J integral at the moving crack tip, however, attains a steady state value for normalized crack lengths of $L/L_0 > 5.0$, while the J values at the stationary crack tip rise continuously.

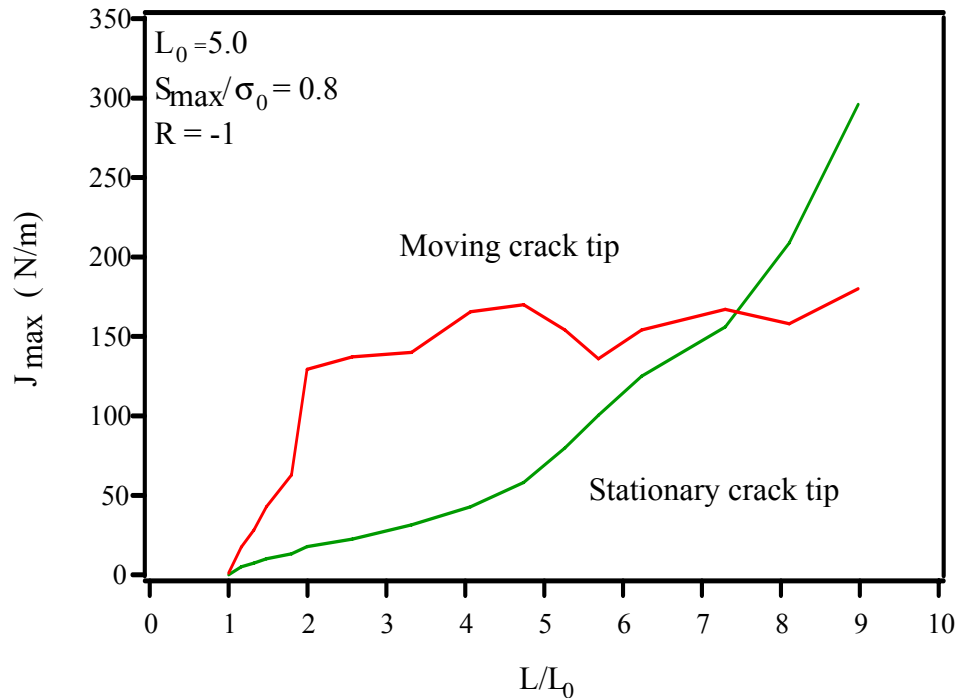


Figure 35. Variation of J integral at the stationary and moving crack tip as the fatigue crack grows away from the hot spot. All lengths are in mm. The J integral values correspond to a hypothetical stress level of $S_{\max}/\sigma_0 = 0/8$ and do not reflect actual values for fatigue cracks in tank car stub sills.

For most crack lengths, the J value at the moving crack tip is higher than the value at the stationary crack tip, which implies that the crack growth rate at the moving crack tip will be higher. But Figure 35 suggests that eventually the crack will grow at a faster rate towards the hot spot than away from it. As crack lengths are very large, J values are high enough to cause crack growth at both the crack tips but at different rates.

Determination of crack growth rates requires an assessment of the crack opening levels. Figure 36 shows the variation of Mode I crack opening levels for two different cracks: one growing towards the hot spot and the other growing away from it. The figure shows that the crack opening level for the crack growing towards the hot spot is much higher than the opening level for the crack which grows away from the hot spot. Further, the crack opening level for the crack growing away from the hot spot attains stability, while no such stable behavior is observed for the curved crack growing towards the hot spot. This is expected as the hot spot acts as a stress raiser, and the crack growing towards it continuously experiences increasing plasticity in its wake.

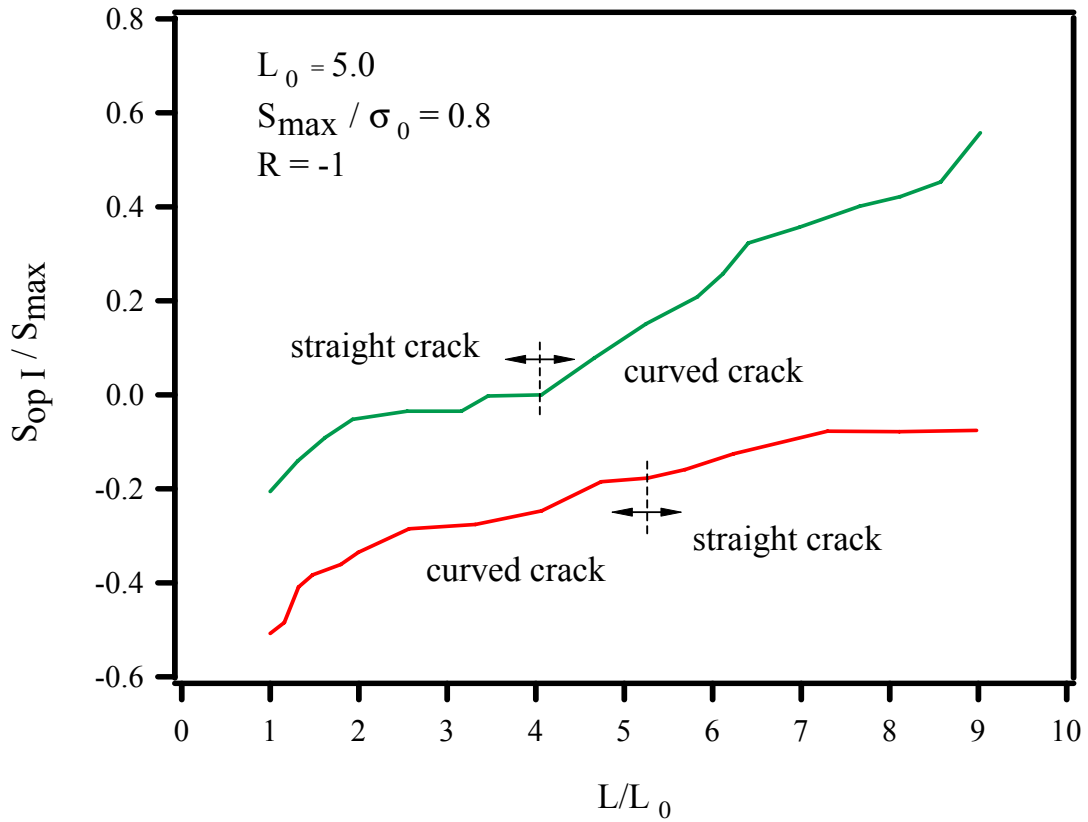


Figure 36. Mode I opening levels for (a) crack growing towards and (b) crack growing away from the hot spot in the tank car stub sill model. All lengths are in mm.

Figure 37 shows the variation of K_{\max} , K_{open} , and ΔK_{eff} with crack length as the crack grows toward the hot spot. Notice that the effective stress intensity range initially increases, reaches a maximum, and then starts to decrease. This implies that the crack will initially accelerate, attain a peak rate, and then continue to decelerate. This trend is reflected in Figure 38, which shows lower crack growth rates for the crack growing towards the hot spot and lower rates for the crack growing away from the hot spot. Thus, it is seen that although the crack will start to grow in both directions (towards and away from the hot spot), it will grow at a higher rate away from the hot spot than towards it.

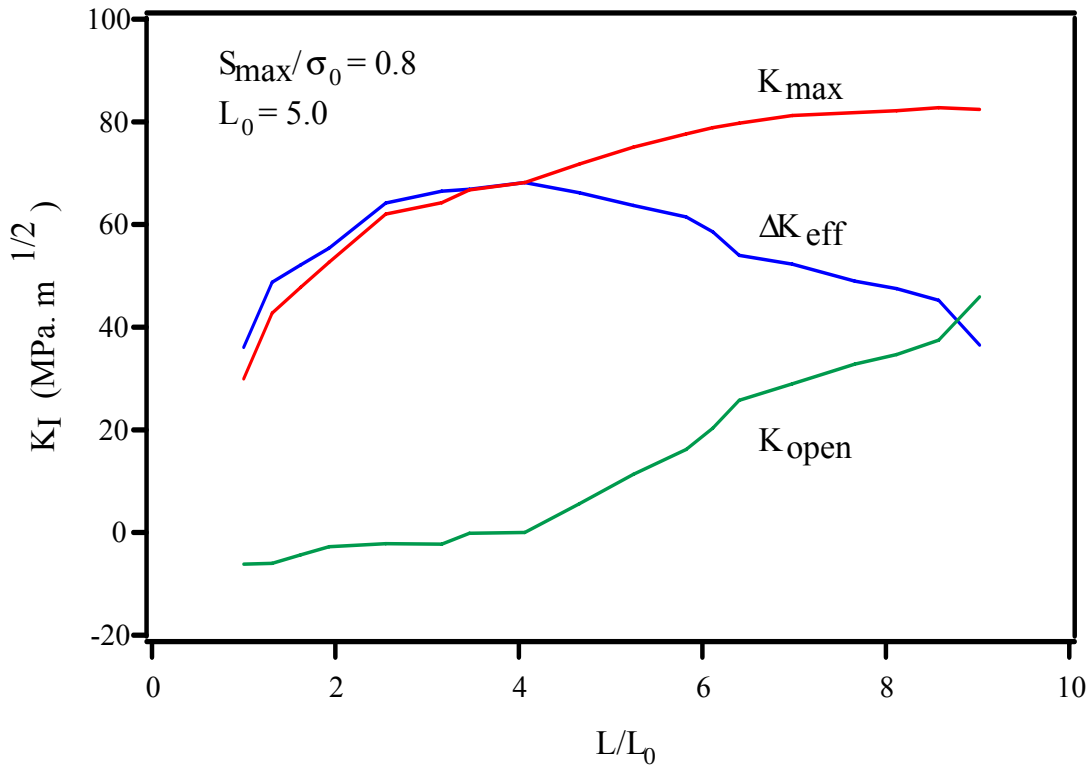


Figure 37. FE estimates of effective SIF for fatigue crack growing towards the hot spot in the stub sill model. The estimates are significantly higher than the values expected for actual tank car stub sill cracks. This is due to the large remotely applied stress $S_{\max}/\sigma_0 = 0.8$. All lengths are in mm.

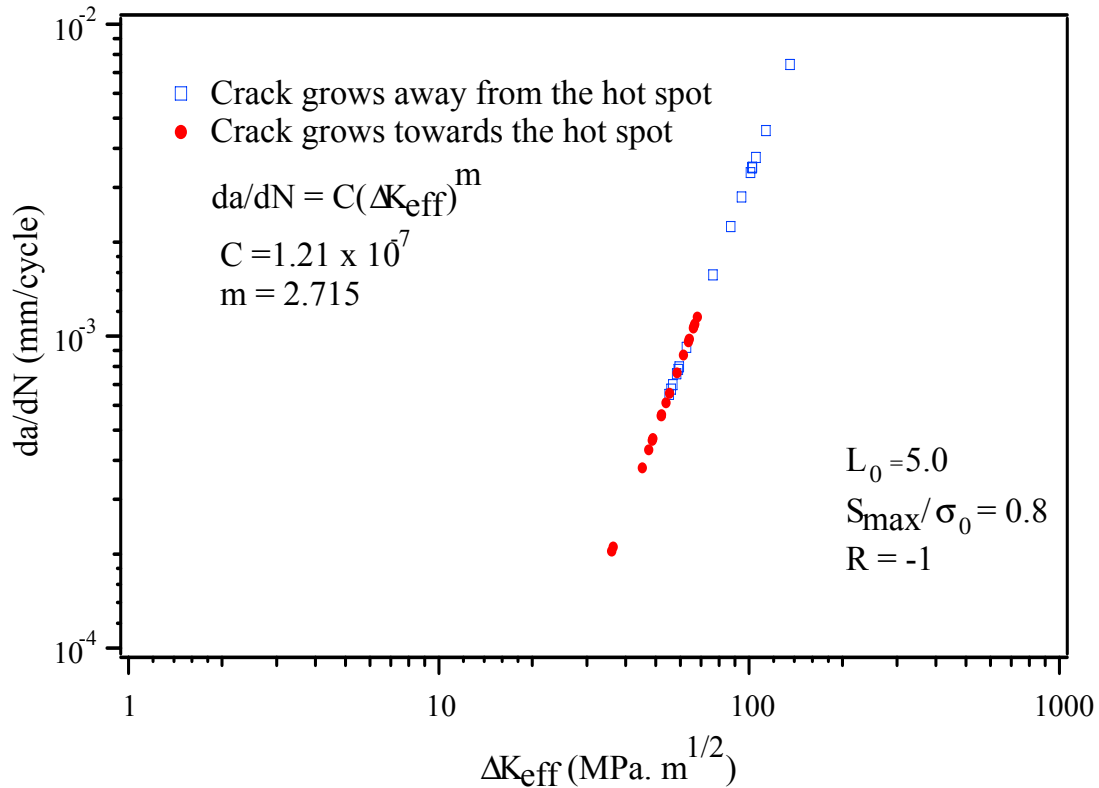


Figure 38. Computed estimates of crack growth rates for (a) crack growing towards and (b) crack growing away from the hot spot in the stub sill model. The selected Paris Law constants C and m correspond to commercial steel. The crack growth rates predicted here do not reflect actual crack propagation rates in tank car stub sills. All lengths are in mm.

Figure 39 shows the comparison of fatigue life of the stub sill for the two possible cases of crack propagation. The figure shows that the fatigue life of the stub sill is reduced by half when the crack propagates away from the hot spot than when it propagates towards it. This follows from Figures 37 and 38. The crack is subjected to lower stress intensity when it propagates towards the hot spot. In addition, the crack growth rate is higher when the crack grows away from the hot spot. Since SIF values are very large for the lengths considered here, the maximum life is about one-tenth of a million cycles, which is lower than the expected life in regular machine components.

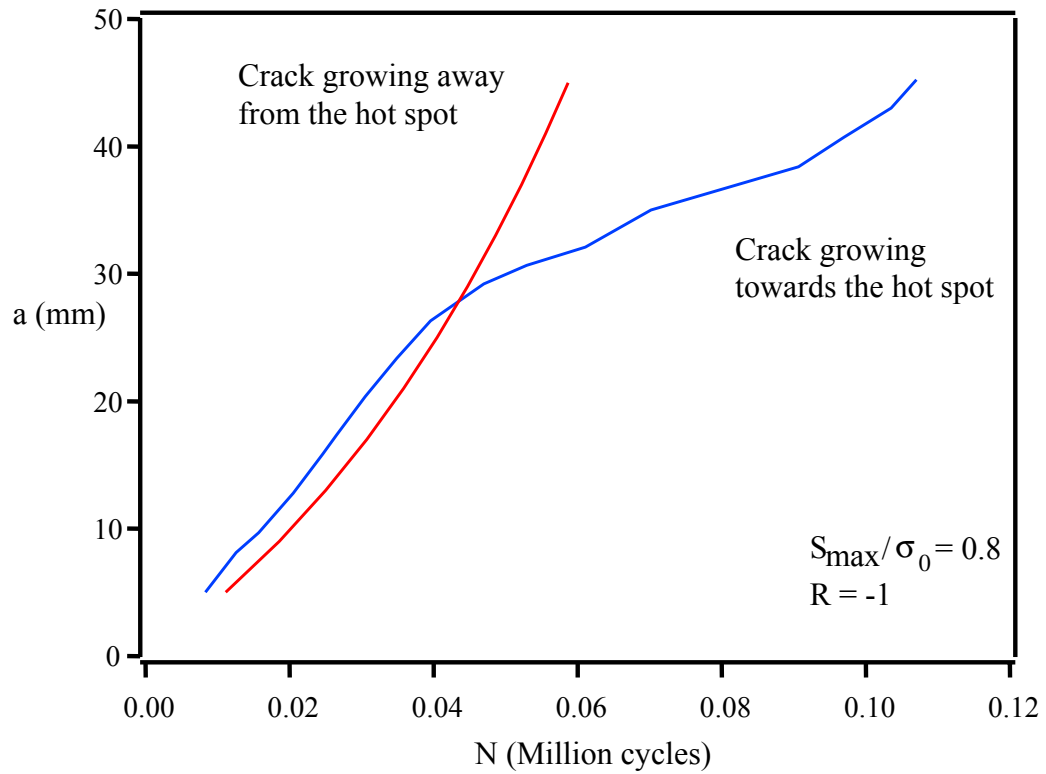


Figure 39. Life prediction for the stub sill as a function of crack length. The above life prediction provides a comparison between the crack growth rate for a crack growing away from the hot spot and for a crack growing towards the hot spot. The above values of crack length (a) and number of cycles (N) do not correspond to predicted values for actual fatigue cracks in tank car stub sills.

7. Summary and Conclusions

The objective of this project has been to investigate, and develop if appropriate, suggested modifications and improvements to the current DTA procedure for prediction of fatigue life of stub sill tank cars, with the ultimate goal of establishing safe inspection intervals.

As a result of the work reported here, it is recommended that consideration be given to establishing a new multi-level procedure for establishing safe inspection intervals in which tank car builders/owners can trade off the cost of more frequent inspections against the time and expense of conducting more accurate engineering evaluations of fatigue life associated with specific stub sill tank car designs. Section 4.2 discusses a possible multi-level evaluation procedure.

Two areas of improvement were selected for study and evaluation as being of the highest potential for inclusion in the proposed new multi-level evaluation procedure:

1. *Improvements in the structural modeling of the cracked stub sill, involving explicit modeling of embedded cracks.*

It was found that the shape of a growing surface crack is insensitive to the initial size and shape of the crack and depends significantly only upon the DOB, a parameter describing the stress distribution in the stub sill top plate. This fact makes it possible to more accurately characterize the local stress regimes that drive crack growth, by utilizing a small and manageable number of structural (FE) analyses of the stub sill tank car, with (surface and through) cracks explicitly modeled.

Sample fatigue life calculations using this first improvement alone resulted in a 67 percent increase in predicted fatigue life over that predicted by DTA.

2. *Improvement in the basic Paris Law for crack growth, taking crack closure and plasticity effects into account.*

As an integral part of this effort, fundamental investigations were undertaken of the crack closure and growth characteristics of non-planar (slanted, deflected, and curved) cracks that could initiate and propagate in the sill top plate because of the typical location of the stress hot spot under vertical coupler loading (see Figure 2).

Mode I crack opening stress levels are substantially higher for slanted cracks than for straight cracks normal to the remote stress, implying much slower crack growth rates for the slanted cracks. Crack opening levels are also higher for $R = 0$ than for $R = -1$ fatigue loading.

Initially slanted cracks which deflect to reorient themselves normal to the remote stress initially grow more rapidly immediately after deflecting, but then they stabilize and grow at the same rate as a straight crack in pure Mode I loading.

Cracks located near the hot spot in the stub sill top plate tend to grow more rapidly away from the hot spot (towards the straight segment of the footprint) because of higher crack opening stress levels for cracks growing toward the hot spot.

The understanding of non-planar crack growth gained in this study provides support for the exclusive consideration of planar cracks in both the current DTA procedure and the proposed new multi-level procedure.

It is recommended that a modified Paris Law be adopted that incorporates crack opening stress, perhaps as a function of stress biaxiality, in an effective $SIF \Delta K_{eff}$.

The Level 2a procedure (Improvement 1 above), proposed herein, is believed to be practically viable at the present time. It has been shown that the load redistribution effect is significant and that it may well be worth taking into account even at the expense of additional analyses, since it significantly increases predicted fatigue life. Constraint and crack closure effects can be taken into account in a modified Paris Law for immediate application (Level 2b) without considering crack deflection or curvature. Additional fatigue and fracture testing of tank car steels might be undertaken in the future to establish applicable fracture toughness values.

8. References

1. Research and Special Programs Administration, "Detection and Repair of Cracks, Pits, Corrosion, Lining Flaws, Thermal Protection Flaws, and Other Defects of Tank Car Tanks: Docket HM-201," Federal Register, vol. 52, No. 235, 1987, p. 46510.
2. National Transportation Safety Board, "Inspection and Testing of Railroad Tank Cars," Special Investigation Report NTSB/SIR-92/05, 1992.
3. Research and Special Programs Administration, "Detection and Repair of Cracks, Pits, Corrosion, Lining Flaws, Thermal Protection Flaws, and Other Defects of Tank Car Tanks: Final Rule," Federal Register, vol. 60, September 1995, pp. 49048-49083.
4. Newman, Jr., J.C., and Raju, I.S., "An Empirical Stress-Intensity Factor Equation for the Surface Crack," Engineering Fracture Mechanics, vol. 15, No. 1-2, 1981, pp. 185-192.
5. Newman, Jr., J.C., and Raju, I.S., "Prediction of Fatigue Crack Growth Patterns and Lives in Three-Dimensional Cracked Bodies," Advances in Fracture Research (Fracture 84), Sixth International Conference on Fracture, vol. 3, 1984, pp. 1597-1608.
6. McClung, R.C., "Closure and Growth of Mode I Cracks in Biaxial Fatigue," Fatigue and Fracture in Engineering Materials and Structures, vol. 12, No. 5, 1989, pp. 447-460.
7. Kibey, S., Sehitoglu, H., and Pecknold, D.A., "Modeling of Fatigue Crack Closure in Inclined and Deflected Cracks," International Journal of Fracture, vol. 129, No. 3, October 2004, p. 279-308.
8. Cardinal, J.W., McKeighan, P.C., and Hudak, S.J., "Damage Tolerance Analysis of Tank Car Stub Sill Cracking," SwRI Project No. 06-6965, November 1998.
9. Forman, R.G., et al., "Fatigue Crack Growth Computer Program NASGRO," version 3.00, JSC-22267B, NASA-JSC, July 1996.
10. Elber, W., "Damage Tolerance in Aircraft Structures," ASTM STP 486, 1971, pp. 230-242.
11. Bell, P.D., and Wolfman, A., "Mathematical Modeling of Crack Growth Interaction Effects," ASTM STP 595, 1976, pp. 157-171.
12. de Koning, A.U., "A Simple Crack Closure Model for Prediction of Fatigue Crack Growth Rates Under Variable-Amplitude Loading," ASTM STP 743, 1981, pp. 63-85.
13. Dugdale, D.S., "Yielding of Thin Sheets Containing Slits," Journal of Mechanics and Physics of Solids, vol. 8, 1960, pp. 100-104.
14. Baudin, G., and Robert, M., "Crack Growth Life-Time Prediction Under Aeronautical Type Loading," Proceedings of the 5th European Conference of Fracture, Lisbon, Spain, 1984, pp. 779-792.
15. Aliaga, D., Davy, A., and Schaff, H., "A Simple Crack Closure Model for Predicting Fatigue Crack Growth Under Flight Simulation Loading," ASTM STP 982, 1987, pp. 491-504.
16. Newman, Jr., J.C., "A Crack-Closure Model for Predicting Fatigue Crack Growth Under Aircraft Spectrum Loading," ASTM STP 748, pp. 55-84.
17. Newman, Jr., J.C., "A Crack-Opening Stress Equation for Fatigue Crack Growth," International Journal of Fracture, Vol. 24, 1984, R131-R135.
18. Newman, Jr., J.C., "Application of a Closure Model to Predict Crack Growth in Three Engine Discs Materials," International Journal of Fracture, vol. 80, 1996, pp. 193-218.
19. Harter, J.A., AFGROW Users Guide and Technical Manual, AFRL-VA-WP-TR-1999-3016, 1999.

20. Harter, J.A., "Comparison of Contemporary FCG Life Prediction Tools," *International Journal of Fatigue*, vol. 21, 1999, S181-S185.
21. NASGRO Reference Manual, JSC-22267B, NASA, March 2000.
22. Chang, J.B., and Engle, R.M., "Improved Damage-Tolerance Analysis Methodology," *Journal of Aircraft*, vol. 21, 1984, pp. 722-730.
23. Suresh, S., and Ritchie, R., "A Geometric Model for Fatigue Crack Closure Induced by Fracture Surface Roughness," *Metallurgical Transactions A*, vol. 13A, 1982, pp. 1627-1631.
24. Llorca, J., "Roughness Induced Fatigue Crack Closure: A Numerical Study," *Fatigue and Fracture of Engineering Materials and Structures*, vol. 15, no. 7, 1992, pp. 655-669.
25. Sehitoglu, H., and Garcia, A., "Contact of Crack Surfaces during Fatigue: Part 1. Formulation of the Model," *Metallurgical and Materials Transactions A*, vol. 28A, 1997, pp. 2263-2275.
26. Sehitoglu, H., and Garcia, A., "Contact of Crack Surfaces during Fatigue: Part 2. Simulations," *Metallurgical and Materials Transactions A*, vol. 28A, 1997, pp. 2277-2289.
27. Tschegg, E.K., "Sliding Mode Crack Closure and Mode III Fatigue Crack Growth in Mild Steel," *Acta Metallurgica*, vol. 31, No. 9, 1983, pp. 1323-1330.
28. Carlson, R.L., and Beevers, C.J., "A Mixed Mode Fatigue Crack Closure Model," *Engineering Fracture Mechanics*, vol. 22, No. 4, pp. 651-660, 1985.
29. Tong, J., Brown, M.W., and Yates, J.R., "A Model for Sliding Mode Crack Closure. Part I: Theory for Pure Mode II Loading," *Engineering Fracture Mechanics*, vol. 52, No. 4, 1995, pp. 599-611.
30. Tong, J., Brown, M.W., and Yates, J.R., "A Model for Sliding Mode Crack Closure. Part II: Mixed Mode I and II Loading and Application," *Engineering Fracture Mechanics*, vol. 52, No. 4, 1995, pp. 613-623.
31. Lalor, P., and Sehitoglu, H., "Crack Closure Outside Small Scale Yielding Regime," *ASTM STP 982*, 1988, pp. 342-360.
32. McClung, R.C., and Sehitoglu, H., "Finite Element Analysis of Fatigue Crack Closure 1. Basic Modeling Issues," *Engineering Fracture Mechanics*, vol. 33, No. 2, 1989, pp. 237-252.
33. McClung, R.C., and Sehitoglu, H., "Finite Element Analysis of Fatigue Crack Closure 2. Numerical Results," *Engineering Fracture Mechanics*, vol. 33, No. 2, 1989, pp. 253-272.
34. Gall, K., Sehitoglu, H., and Kadioglu, Y., "FEM Study of Fatigue Crack Closure Under Double Slip," *Acta Materialia*, vol. 44, No. 10, 1996, pp. 3955-3965.
35. ABAQUS/Standard User's Manual, version 6.1, HKS, 2000.
36. Sehitoglu, H., and Sun, W., "Modeling of Plane Strain Fatigue Crack Closure," *ASME Journal of Engineering Materials and Technology*, vol. 113, 1990, pp. 31-40.
37. Sehitoglu, H., and Sun, W., "Residual Stress Fields during Fatigue Crack Growth," *Fatigue and Fracture of Engineering Materials and Structures*, vol. 15, No. 2, 1992, pp. 31-40.
38. Smith, M.C., and Smith, R.A., "Towards an Understanding of Mode II Fatigue Crack Growth," *ASTM STP 924*, 1988, pp. 260-280.
39. Newman, Jr., J.C., "A Finite-Element Analysis of Fatigue Crack Closure," *ASTM STP 590*, 1976, pp. 280-301.
40. Shiratori, M., Miyoshi, T., Miyamoto, H., and Mori, T., "A Computer Simulation of Fatigue Crack Propagation Based on the Crack Closure Concept," *Adv. In Research on the Strength and Fracture of Materials (Fracture 1977)*, Fourth International Fracture Conference, Waterloo, Canada, 1977, Pergamon, vol. 2B, pp. 1091-1098.

41. Fuhring, H., and Seeger, T., "Dugdale Closure Analysis of Fatigue Cracks Under Constant Amplitude Loading," *Engineering Fracture Mechanics*, vol. 11, 1979, pp. 99-122.
42. Budiansky, B., and Hutchinson, J.W., "Analysis of Closure in Fatigue Crack Growth," *Journal of Applied Mechanics*, Trans. ASME, vol. 45, 1978, pp. 267-276.
43. Newman, Jr., J.C., "A Crack-Closure Model for Predicting Fatigue Crack Growth Under Aircraft Spectrum Loading," *ASTM STP 748*, 1981, pp. 55-84.
44. Sehitoglu, H., "Crack Opening and Closure in Fatigue," *Engineering Fracture Mechanics*, vol. 21, No. 2, 1985, pp. 329-339.
45. Ibrahim, F.K., Thompson, J.C., and Topper, T.H., "A Study of the Effect of Mechanical Variables on Fatigue Crack Closure and Propagation," *International Journal of Fatigue*, vol. 8, No. 3, 1986, pp. 135-142.
46. Wei, L., and James, M.N., "Fatigue Crack Closure of Inclined and Kinked Cracks," *International Journal of Fracture*, vol. 116, 2002, pp. 25-50.
47. Parry, M.R., Syngellakis, S., and Sinclair, I., "Numerical Modeling of Combined Roughness and Plasticity Induced Crack Closure Effects in Fatigue," *Material Science and Engineering*, A291, 2000, pp. 224-234.

Appendix A.

Detailed FE Study on Plasticity and Crack Closure Effects for Through Cracks

In recent years, much emphasis has been placed on FE modeling to investigate closure in fatigue cracks. The previous research at UIUC on fatigue crack closure carried out by Sehitoglu et al. used a specialized code, which was initially developed by Lalor and Sehitoglu [25], subsequently modified by Sehitoglu and McClung [26, 27], and further modified by Kadioglu, Sehitoglu, and Gall [28]. This elastic-plastic FE model assumes crack plane symmetry and therefore cannot be extended to model crack deflection and closure arising out of it.

The current research examines crack closure in slanted and deflected cracks. The objective is to gain more insight into the effect of non-planar crack geometry on premature crack face contact and its consequences on crack growth rates. Slanted and deflected cracks are allowed to propagate under local mixed-mode conditions when subjected to remote Mode I cyclic loading. The resulting closure is due to a combination of PICC and sliding occurring due to the tangential sliding between crack faces as the crack propagates. Consequently, the effects of crack geometry, friction, and contact interaction between crack faces, stress level, and R ratio on crack opening levels is investigated.

A two-dimensional elastic-plastic FE model has been developed using the commercially available package ABAQUS [29] to analyze fatigue crack closure in cracks which deviate from their original path. The phenomenon of closure in such cracks will involve not only the plasticity-induced crack closure mechanism but also the relative sliding between the crack faces and the frictional effects arising out of such relative sliding. Thus, it becomes essential to incorporate the effect of both plasticity and frictional nonlinearities on closure behavior of a fatigue crack. Fatigue cracks, in general, can start growing in a particular direction and then deflect to grow in a different direction. Such cracks have been termed as deflected cracks in this research. It is also possible that some fatigue cracks may grow at an angle relative to the remote load. This report uses the term slanted cracks or inclined cracks to describe these cracks. Figure A-1 illustrates a slanted and a deflected crack, which are subjected to Mode I remote loading but exhibit local mixed-mode behavior.

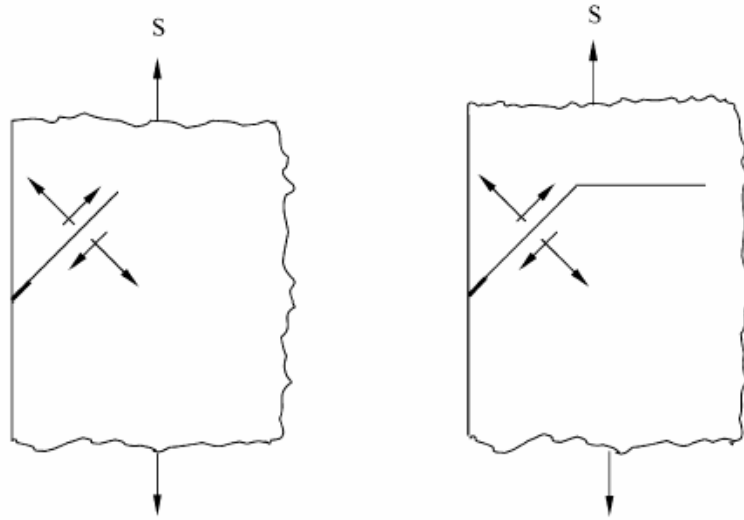


Figure A-1. (a) Slanted crack and (b) deflected crack.

The material is modeled to follow a bilinear stress-strain relationship. It exhibits linear elasticity below its initial yield strength $\sigma_0 = 480$ MPa. The young's modulus is assumed to be $E = 200$ GPa, and Poisson's ratio is assumed to be $\nu = 0.30$. The material follows a Von Mises yield criterion with linear kinematic hardening to capture Bauschinger effect associated with reversed yielding. The hardening modulus H is assumed to be constant equal to $0.01E$, which is typical of low hardening steels and several aluminum alloys. Plane stress conditions have been assumed. Closure results for straight cracks under plane strain conditions have been reported elsewhere [30, 31]. Hence, plane strain conditions are not considered here in any of the FE simulations.

The extent of closure occurring in fatigue cracks can be quantified with ΔK_{eff} , and the dependence of ΔK_{eff} on various parameters can be expressed as:

$$\Delta K_{eff} = f\left(\frac{S_{max}}{\sigma_0}, R, \frac{H}{E}, \frac{\bar{\sigma}}{\sigma_H}, \mu, a, \text{Geometry}, \text{Microstructure}, \text{constraint}\right) \quad (7)$$

This study investigates the effect of applied stress S_{max} / σ_0 on the closure behavior of both slanted and deflected fatigue cracks. The term geometry in equation (2) implies both geometry of the specimen (SENT, CT, etc.) and the geometry of the crack (crack orientation and crack path). This study specifically addresses the latter (i.e., the effect of crack orientation and crack path on crack closure). This is achieved by investigating the crack closure behavior of slanted and deflected cracks with certain predetermined orientations. The R-ratio effect is investigated by considering two different R ratios: $R = 0$ and $R = -1$. Further, the effect of friction on crack closure is incorporated in the analysis by accounting for friction between the crack faces in the FE model.

A.1 FE Results and Discussion (from IJF paper) [7]

The following sections present the results for crack opening behavior based on various FE analyses. The effect of following parameters on stable crack opening levels are considered: applied stress level S_{max} / σ_0 , load ratio R, crack orientation relative to the applied loading θ , crack path deflection, and friction between crack faces. Mode I and Mode II crack opening levels for SENT specimens with edge cracks subjected to constant amplitude fatigue loading are examined. Before describing the details of mesh development, crack advance scheme, mesh refinement, and contact modeling, this section outlines the specimen geometries investigated in this research. As mentioned before, an important objective of this research is to examine the effect of crack orientation and crack path on PICC. To this end, the following specimen geometries were considered:

- *Geometry 1*: A SENT specimen with an initial edge crack inclined at an angle of 45° to the direction of applied loading in Mode I. The fatigue crack is allowed to propagate along the 45° direction without deviating from its path. This geometry facilitates determination of stable opening levels for a fatigue crack oriented at 45° (Figure A-2.(a)).
- *Geometry 2*: A SENT specimen with an edge crack inclined at an angle of 45° to the direction of applied loading, which is initially allowed to propagate in the 45° direction long enough to attain stable opening levels, and subsequently allowed to deflect and grow perpendicular to the Mode I loading (Figure A-2.(b)). In other words, Geometry 2 depicts the case of crack deflection after stabilization. The length of the slanted part of the crack exceeds the minimum required crack length to attain stabilization (denoted by L^*).
- *Geometry 3*: A SENT specimen with an edge crack inclined at an angle of 45° to the direction of applied loading, which is initially allowed to propagate in the 45° direction. The crack, however, is allowed to deflect and grow perpendicular to the applied loading before stable opening levels are attained (Figure A-2.(c)). This is then the case of deflection before stabilization. In this case, the length of the slanted part of the crack is less than L^* .

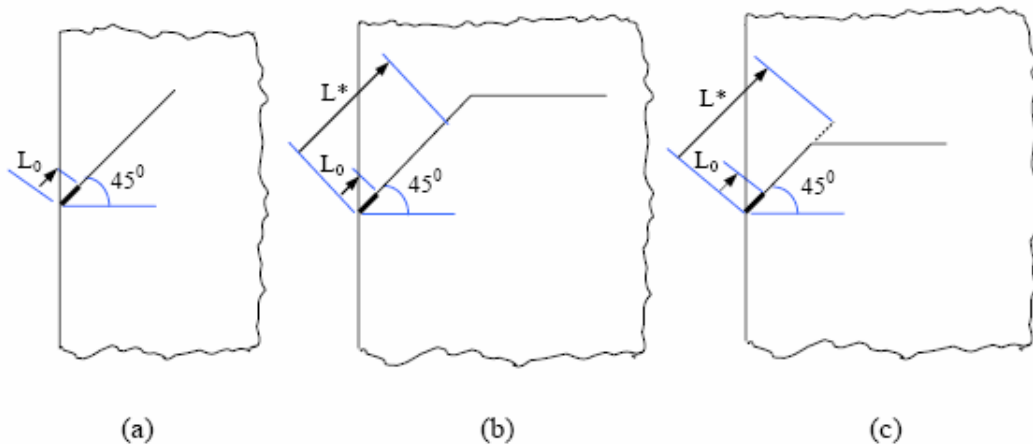


Figure A.2. (a) Geometry 1: slanted crack; (b) Geometry 2: crack deflection after stabilization; (c) Geometry 3: crack deflection before stabilization. (L^* denotes the stabilization crack length.)

While Geometry 1 helps to determine the effect of crack orientation on Mode I and Mode II opening levels, Geometries 2 and 3 provide insight into the effect of crack path on crack opening levels.

A.2 Crack Face Interaction in a Fatigue Cycle

Before discussing the results of the FE simulations, it is pertinent to discuss the important events related to crack closure occurring in a fatigue cycle. Figure A-3 shows a schematic of a fatigue cycle. At point A, the crack is subjected to maximum load and experiences maximum crack opening displacement. As the specimen is unloaded, during the first increment of unloading, crack tip advances by one or more elements and crack extension is allowed to occur. With further unloading, crack opening displacements gradually reduce until the second (as well as first) node behind the crack tip closes. This event marks the beginning of crack closure and is denoted as B in Figure A-3. The applied load at B is the crack closure level denoted by S_{cl} . As the specimen is further unloaded, the crack gradually starts to close. With increasing compressive load, the crack faces undergo reversed slip (i.e., the upper crack face slides to the left relative to the lower crack face ($\Delta U_{II} < 0$) [38]). At minimum load (point C) in the cycle, the crack faces experience maximum reversed slip.

When the load is increased from minimum, a state of complete stick ($\Delta U_{II} = 0$) [38] is observed until the load corresponding to point D is reached. The load range between D to E represents a state of partial slip where slip exits over a part of the crack flanks and has not reached the crack tip yet. Point E represents the load at which slip reaches the crack tip for the first time and complete slip initiates. This load is defined at the Mode II opening level in the fatigue cycle.

From point E onwards, the crack starts to open in Mode I, and point F denotes the load at which compressive stresses behind the crack tip change to tensile and the complete crack opens in Mode I. This load is defined as Mode I crack opening level. Figure A-3 depicts the case of slip

before opening in Mode I (i.e., slip propagates to the crack tip before the crack opens completely in Mode I). Figure A-4 shows the situation in which the crack completely opens in Mode I before the crack faces experience Mode II shear offset (equivalent to positive slip) [38]. This is the case of opening before shear offset. In this case, Mode II opening level is equal to the Mode I opening level. Both of these cases have been observed in the crack geometries investigated in this research.

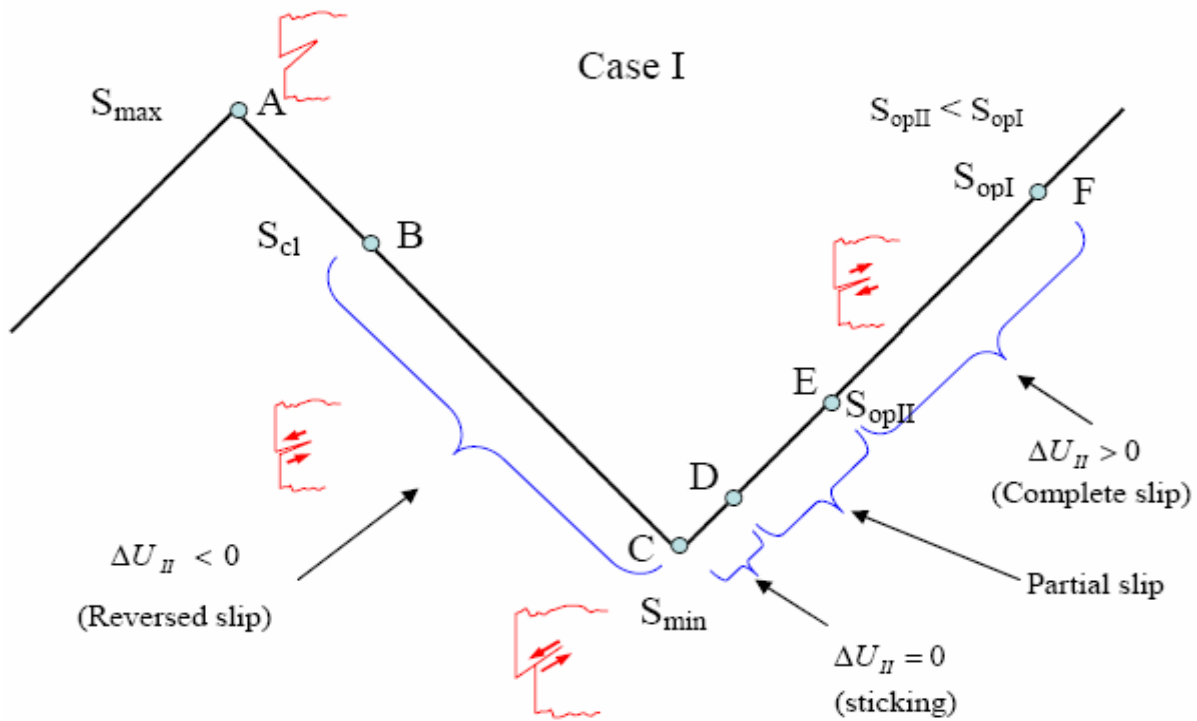


Figure A-3. Case I—Crack face interaction in a fatigue cycle: Crack faces slip in Mode II before opening in Mode I.

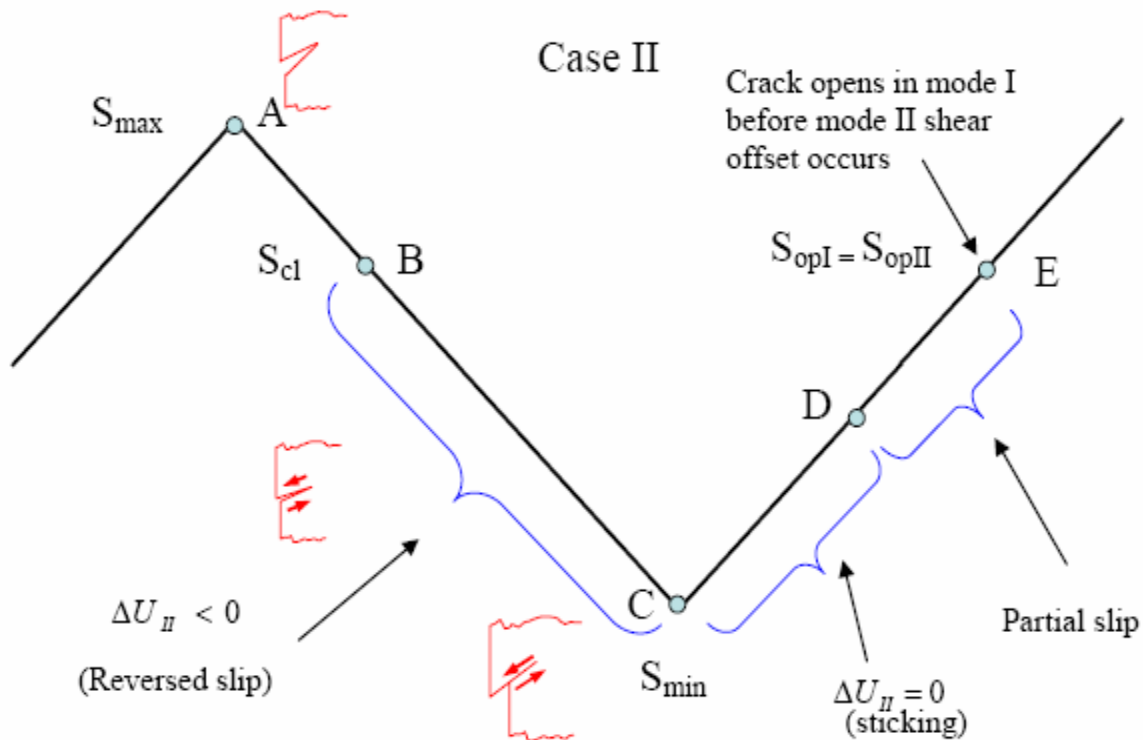


Figure A-4. Case II–Crack face interaction in a fatigue cycle: Crack faces open in Mode I before shear offset in Mode II occurs.

A.3 Effect of Applied Stress Level S_{max}/σ_0 and R Ratio on Crack Opening Levels

To examine the effect of maximum stress on Mode I and Mode II opening levels, a SENT specimen with an edge crack oriented at $\theta = 45^\circ$ relative to load direction (Geometry 1) was subjected to constant amplitude fatigue loading with four different stress levels S_{max}/σ_0 : 0.6, 0.7, 0.8, and 0.9. The dependence of opening levels on R ratio was examined by considering two different values of R: 0 and -1. Figure A-5 and Figure A-6 show the Mode I and Mode II crack opening levels, respectively, normalized by maximum applied stress in the cycle, as a function of normalized crack length. Consider first the Mode I opening levels shown in Figure A-5. Normalized opening stress significantly decreases with increasing maximum stress for both $R = 0$ and $R = -1$. This trend in the stable opening levels has been seen in all numerical and analytical models available in literature. These include the early efforts of Newman [39], Shiratori et al. [40], Fuhring and Seeger [41], and Budiansky and Hutchinson [42]. The later works of Newman [17, 18, 43], Sehitoglu [44], Ibrahim et al. [45], Lalor and Sehitoglu [31], and McClung and Sehitoglu [32, 33] confirmed this phenomenon. Such dependence of stable opening levels on maximum stress is not obvious. Higher applied stress implies higher inelastic deformation in the wake of the crack and should then result in increased closure—an argument not supported by the results. McClung and Sehitoglu [32, 33] explained this apparent anomaly by comparing the crack opening displacements of the fatigue crack with that of a stationary crack of the same length subjected to the same maximum stress. This comparison gives a first estimate of residual deformation. The fatigue crack opening is seen as a competition between residual deformation and the ideal crack opening displacement at maximum load. Using this argument,

McClung and Sehitoglu [32, 33] were able to clarify this apparently anomalous behavior. Figure A-5 reflects a trend consistent with the above explanation.

Figure A-6 shows the Mode II opening levels for a 45° slanted crack. First, note a strong dependence of Mode II opening levels on the load ratio R. Mode II opening levels continuously increase for R = 0 until steady state is attained. On the other hand, for R = -1, the Mode II opening levels initially increase for small crack lengths, reach a maximum, and then continuously drop before stabilizing.

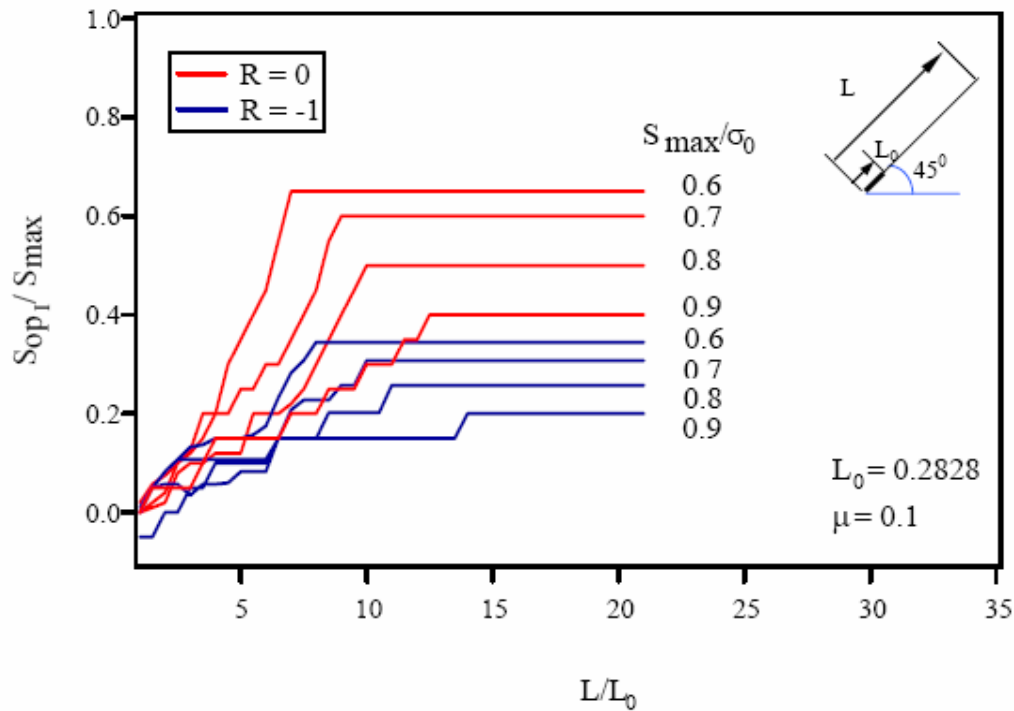


Figure A-5. Normalized Mode I opening levels for a 45° slanted fatigue crack for two different R ratios, plane stress. All lengths are in mm.

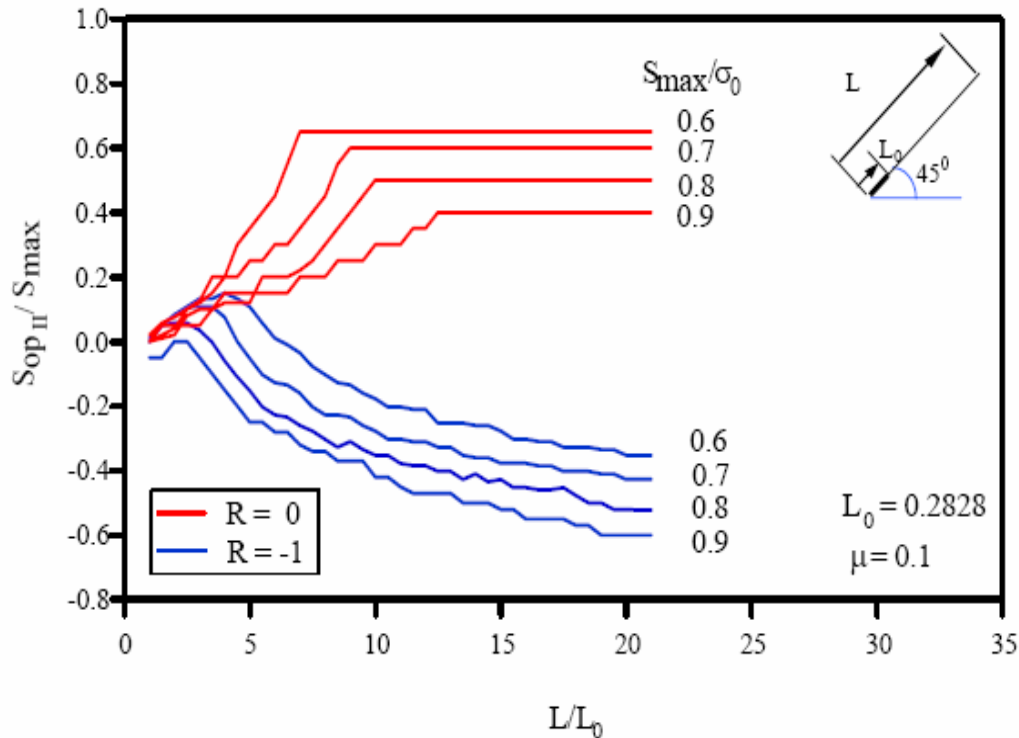


Figure A-6. Normalized Mode II opening levels for a 45° slanted fatigue crack, plane stress. For $R = 0$, Mode II opening levels coincide with Mode I opening levels (Case II, Figure A-4). For $R = -1$, Mode II sliding occurs before Mode I opening (Case I, Figure A-3). All lengths are in mm.

This difference in the nature of the curves for the two load ratios can be explained by a careful examination of the crack face interaction as the crack propagates. For $R = 0$, the crack faces open in Mode I before slip reaches the crack tip at any given length of the fatigue crack. The applied Mode I load is able to overcome the residual plasticity and open the crack in Mode I before the slip state can change from partial slip to complete slip. The crack faces experience shear offset in Mode II after Mode I opening occurs. This opening before shear offset phenomenon implies that Mode II opening level values are equal to Mode I opening level values for a given crack length. Hence, the Mode II opening level curves for $R = 0$ in Figure A-6 are identical to the Mode I opening level curves in Figure A-5. However, Mode I and Mode II opening level curves are not identical for $R = -1$. This can be explained as follows: during the first few cycles, the crack face interaction for $R = -1$ is as depicted in Figure A-4, where crack opens in Mode I before slip reaches the crack tip. This is the case of opening before shear offset during which Mode II opening levels are equal to Mode I opening levels and a monotonic rise in the Mode II opening levels is observed. The Mode I (and hence Mode II) opening levels that are essentially low as crack lengths are not large enough to cause substantial forward plastic deformation. Thus, in the case of opening before shear offset phenomenon, Mode II opening levels are essentially dictated by Mode I opening levels. For larger crack lengths, however, slip reaches the crack tip before the crack opens in Mode I. This is the case of slip before opening in Mode I (Figure A-3). Consequently, Mode I and Mode II opening levels are no longer equal. With increasing crack length, the event of complete slip initiates at decreasing loads in a fatigue

cycle, leading to a continuous decrease in the Mode II opening loads until a steady state is reached.

Another interesting feature of Figure A-6 is that stable normalized Mode II opening level values decrease with increase in maximum stress S_{\max}/σ_0 . This trend can be explained on the basis of Coulomb's friction model. The event of complete slip can be seen as a competition between (1) the shear stresses transmitted across the contacting crack faces (which depend on the applied maximum stress), causing the crack faces to slide relative to each other, and (2) the frictional resistance opposing the relative motion which is proportional to the contact pressure distribution along the crack flanks. Figure A-7 shows the contact pressure distribution behind the crack tip at minimum load for two stress levels, $S_{\max}/\sigma_0 = 0.6$ and 0.8 . The normalized contact pressure distribution and hence the frictional resistance do not differ significantly for the two stress levels. Consequently, in accordance with Coulomb's model, shear stress distribution along the crack flank for the two stress levels should be almost identical. Figure A-8 confirms this where shear stresses along the crack faces, normalized by the yield stress in shear, are plotted for the two stress levels. These two shear stress distributions correspond to the instant in the fatigue cycle when complete forward slip initiates. Although the shear stress distributions are almost identical, the normalized remote stress values, S/S_{\max} , producing these distributions are significantly different (-0.35 and -0.48). This implies that the Mode II crack opening level will be lower at higher maximum stress.

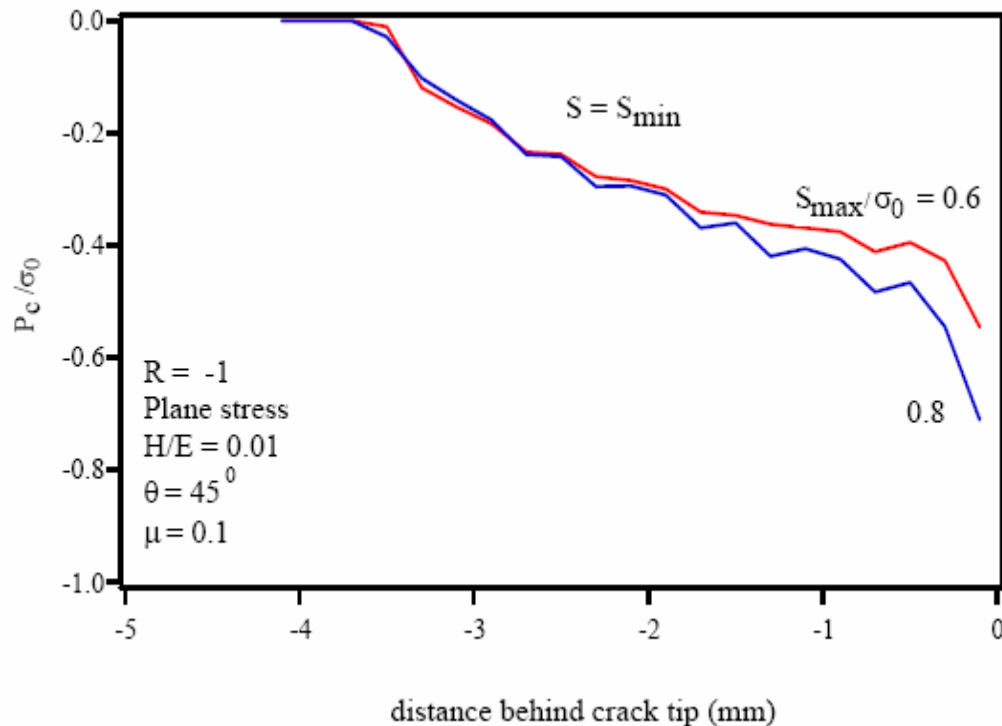


Figure A-7. Normalized contact pressure distribution at minimum load in a 45° slanted crack. Pressure distributions (and hence the resistance to slip) are almost equal for different applied maximum stress levels: 0.6 and 0.8. All lengths are in mm.

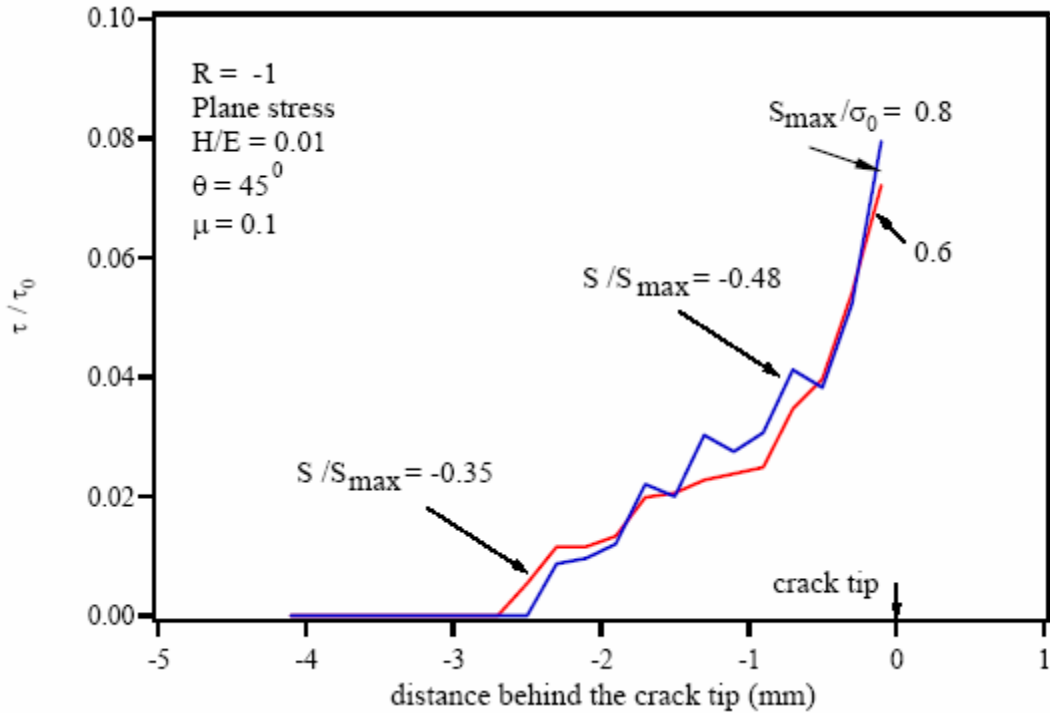


Figure A-8. Shear stress distributions along the contacting crack flanks of a 45° slanted crack plotted at remote stress corresponding to Mode II opening level (complete slip) for $S_{\max}/\sigma_0 = 0.6$ and 0.8 . Although the shear stress distributions are almost identical, the remote stress, S/S_{\max} , producing these distributions is significantly different (-0.35 and -0.48). All lengths are in mm.

A.4 Effect of Crack Orientation

Figure A-9 shows the crack opening levels for two crack orientations: 45° inclined fatigue crack and a straight crack growing in pure Mode I. It is seen that the stable crack opening level for a 45° slanted crack is significantly higher than that for a straight crack subjected to the same maximum stress. Further, note that the difference in the stable opening level of the two crack geometries increases with increase in maximum stress. Clearly, Figure A-9 suggests that an increase in the crack angle will lead to an increase in the Mode I crack opening level. Similar findings have been reported recently by researchers working on inclined cracks. Wei and James [46] estimated Mode I crack opening levels for crack angles ranging from 0° to 60° for $R = 0.05$. Their results are in agreement with the trend shown in Figure A-9. Parry et al. [47] reported a similar dependence of Mode I opening levels on crack angle, although their research focused on both PICC and RICC.

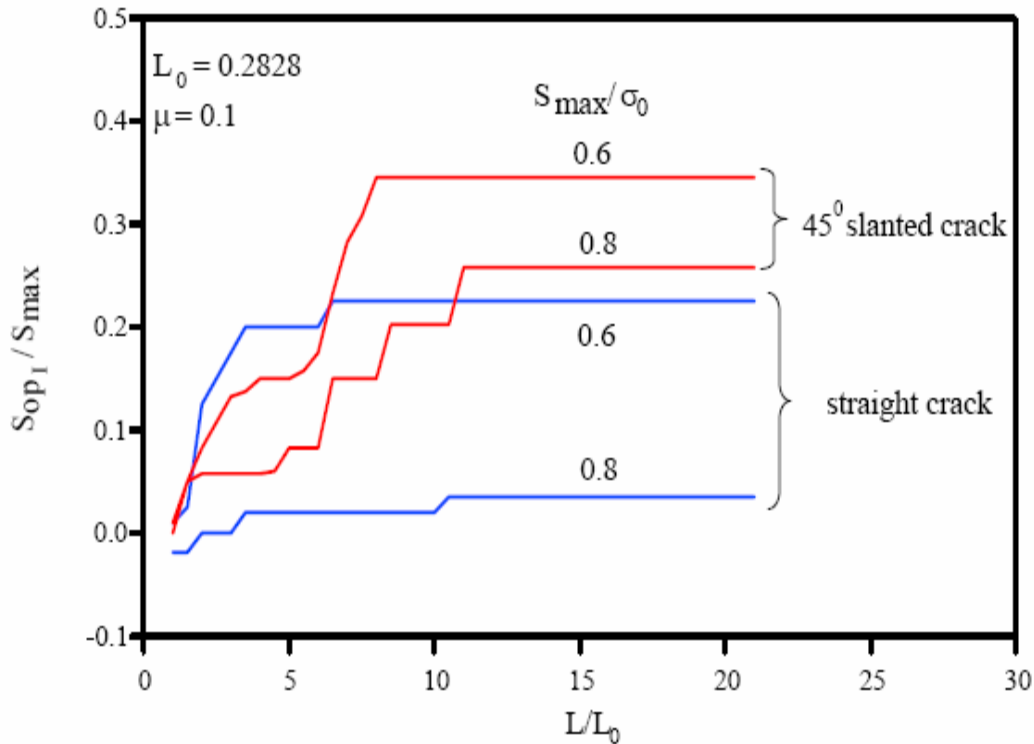


Figure A-9. Effect of crack orientation on stable Mode I opening levels $R = -1$, plane stress. L_0 is the initial crack length. All lengths are in mm.

A.5 Stress-Strain History

Figure A-10 shows the numerically (FE) simulated stress-strain history at a material point along the 45° inclined crack path as the crack tip approaches it and passes that location. The chosen material point corresponds to a node located at $x/L_0 = y/L_0 = 20$. The plotted stress and strain components are normal to the crack faces and correspond to $R = -1$, and maximum remote stress is $S_{max}/\sigma_0 = 0.8$. Initially, when the crack tip is far from the material point (x, y) , the behavior of elastic strain accumulation is not seen. As the crack tip approaches the material point, plastic strain accumulates (the hysteresis loop traverses along x-axis to the right). Maximum plastic strain is attained when the crack tip is located at the chosen material point (x, y) and is as high as 1.5 percent to 2 percent. Once the crack tip passes the material point, strain relaxation occurs, and the strain values drop to about 0.25 percent. Notice that once the crack tip passes the material point, no further accumulation of strain will occur. In Figure A-10, the residual strain in the wake is about 0.25 percent. The figure also shows the load points at which the crack opens in Mode I and Mode II (when the crack tip coincides with the material point). The crack undergoes complete slip in Mode II even though the normal stress σ_n is compressive. When the crack completely opens in Mode I, the normal stress behind the crack tip is tensile. However, the normal stress is compressive at the crack tip. Further, significant hardening does not occur as the material is cyclically loaded beyond yield. This is expected since the hardening modulus of the material is quite low ($H = 0.01E$). This figure also shows that mean stress relaxation does not occur with this (linear hardening) constitutive model. As pointed out by McClung and Sehitoglu

[32,33], this phenomenon of absence of stress relaxation has significant influence on the crack advance scheme. If the specimen is subjected to two full cycles of loading before advancing the crack by one or more elements, local stress redistribution will occur. For linear hardening, however, mean stress will not relax, and the stress-strain response will become stable, resulting in stable opening levels. The simplicity and stability of the stress-strain behavior in a bilinear model makes it an attractive choice for constitutive modeling.

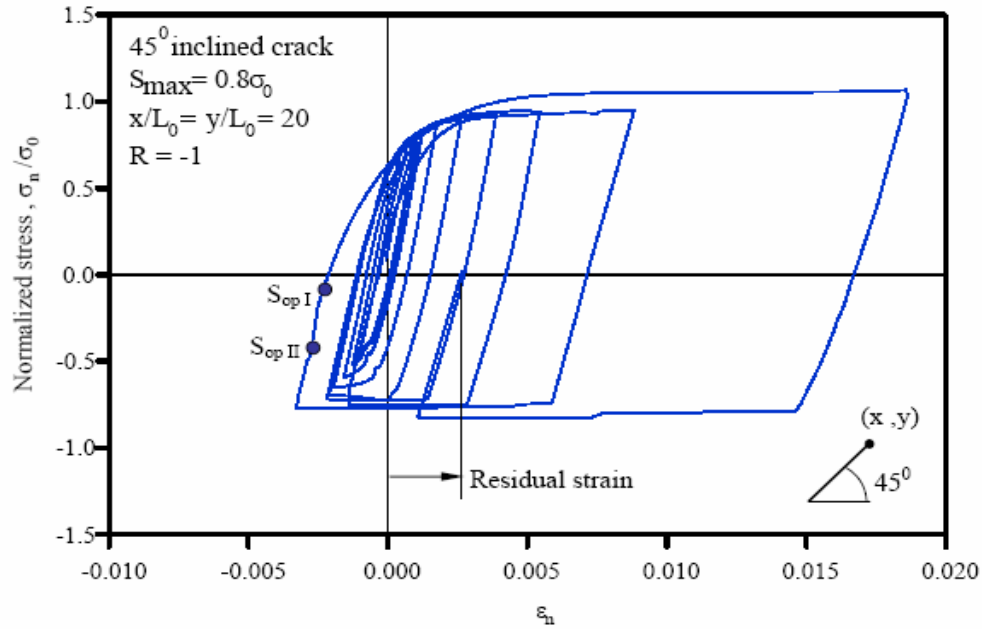


Figure A-10. Normal stress-normal strain history at a material point (x, y) along the inclined fatigue crack as the crack tip approaches the point and passes it. Plane stress, linear hardening with $H/E = 0.01$.

A.6 Effect on Crack Deflection

Another important factor influencing the closure behavior of a fatigue crack is crack path deflection. Figure A-5 summarizes the stable Mode I opening levels for a 45° slanted crack that is allowed to propagate along the initial orientation without deflection. A fatigue crack propagating in mixed mode, however, will tend to deflect in order to grow along the preferred plane or direction. It is therefore reasonable to expect that the 45° slanted crack considered in the previous sections will, at some point, deflect from its initial orientation and start growing in pure Mode I. This section investigates the effect of such a deflection.

Figure A-5 shows that Mode I opening levels attain a steady state at different fatigue crack lengths depending on the maximum stress and R ratio. Further, for a given R ratio, the crack length required to achieve stable opening levels increases with increase in maximum stress. This phenomenon brings out the following two possible cases of crack deflection:

1. Occurrence of crack deflection after Mode I opening levels attain stabilization.

2. Occurrence of crack deflection before Mode I opening levels attain stabilization.

To investigate the above two cases, it is essential to establish a measure of minimum slanted crack length, denoted by L^* , required for stabilization. A logical definition of L^* is the transition crack length corresponding to the highest maximum stress, S_{\max}/σ_0 used to simulate crack deflection. In deflected crack simulations, two stress levels were considered: $S_{\max}/\sigma_0 = 0.6$ and 0.8. The transition crack length for $S_{\max}/\sigma_0 = 0.8$ is 3.1 and is assigned to L^* . The normalized minimum transition length is given by $L^*/L_0 = 11$. Figures A-11 and A-12 show Mode I and Mode II opening levels as a function of crack length. Consider Figure A-11, which depicts the case of deflection after stabilization (Geometry 2 in Figure A-2). First, a steep decrease occurs in the Mode I opening levels immediately after deflection, while there is a gradual rise in Mode II opening levels occurring at the same time. The increase in Mode II opening levels is primarily due to increased resistance to slip offered by the straight portion of the fatigue crack. The Mode I opening level decreases until it equals Mode II S_{op} . The point of equalization of Mode I and Mode II opening levels represents the crack length at which the phenomenon of crack face interaction changes from slip before opening to opening before shear offset. In other words, for smaller lengths of the straight crack, the entire crack slips before opening in Mode I. When the length of the straight portion becomes comparable to the inclined portion of the fatigue crack, frictional resistance is too high to permit complete slip. Hence the crack opens completely in Mode I before Mode II shear offset occurs.

Comparison of Figure A-11 (and Figure A-12) with Figure A-9 reveals that the final opening levels values of the deflected fatigue crack are very close to the opening levels of a pure Mode I straight crack subjected to the same maximum stress. This implies that once the length of the straight portion becomes very large, the deflected crack behaves as a pure Mode I straight crack, and the slanted portion of the crack will no longer play any role in determining the Mode I opening levels. For such a crack, the Mode II component will be nonexistent. However, it is not clear from Figure A-11 if the stable opening level values have been reached for the straight portion of the crack.

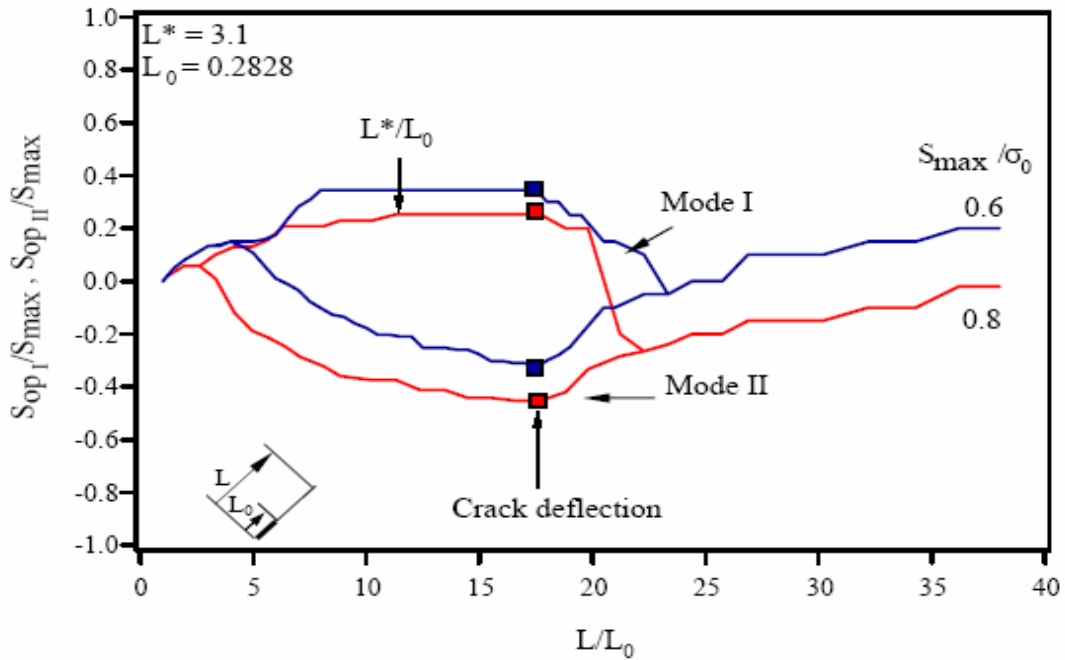


Figure A-11. Mode I and Mode II opening levels for a deflected crack. Deflection occurs after stabilization. All lengths are in mm.

A similar trend is seen in Figure A-12, which depicts the case of deflection before stabilization (Geometry 3 in Figure A-2). Crack deflection results in an immediate drop in the Mode I opening levels and an increase in the Mode II opening levels until the two opening level values become equal. As pointed out earlier, this equality represents a change in the crack face interaction from slip before opening to opening before shear offset. With further increase in the length of the straight portion, opening levels rise steadily and attain stable values. These stable opening level values are in close agreement with the stable opening levels of pure Mode I straight crack (refer to Figure A-9). Thus, it appears that deflection of crack before or after stabilization of Mode I opening levels will not affect the final opening level values. Notice that crack growth rate will accelerate after crack deflection since Mode I opening levels drop steeply in both the cases of crack deflection. Crack growth acceleration, however, will be higher in case of deflection after stabilization since the crack experiences higher effective stress intensity for this case. In addition, in this case, the crack continues to experience lower Mode I opening stresses (hence higher effective stress intensity) for almost all crack lengths. This implies that the crack growth rates will be the highest for Geometry 2 (deflection after stabilization) once the crack deflects toward the preferred plane of growth.

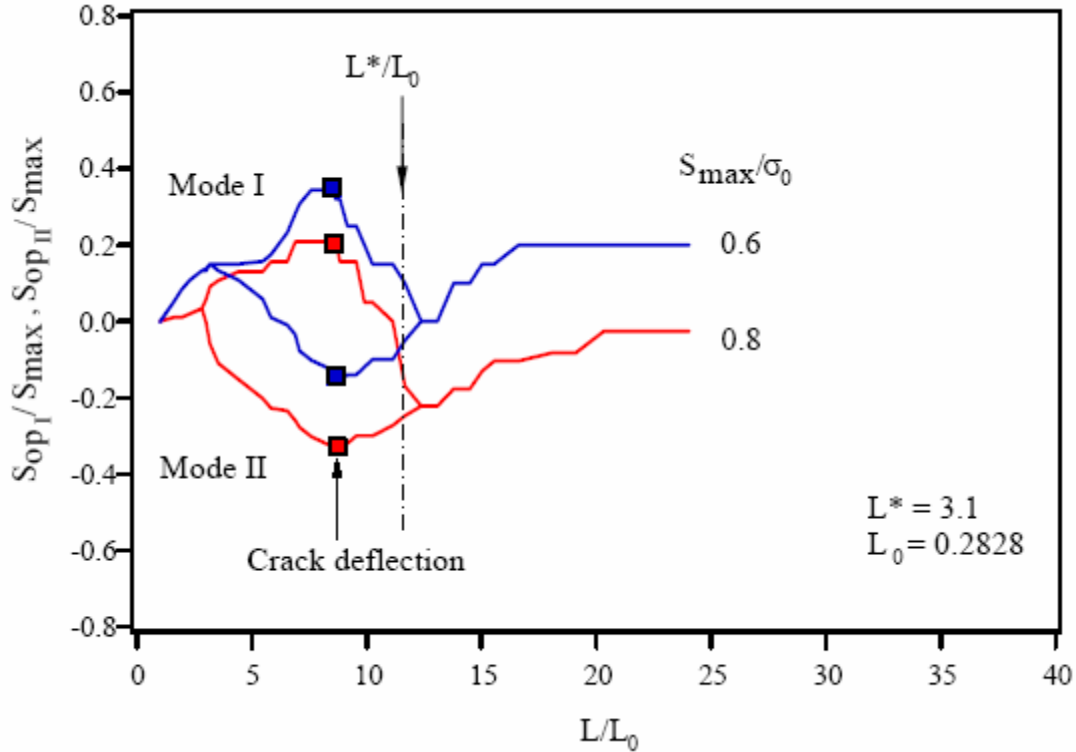


Figure A-12. Mode I and Mode II opening levels for a deflected crack. Deflection occurs before stabilization. All lengths are in mm.

A.7 Effect of Friction

It is clear from previous sections that closure behavior of a slanted fatigue crack is significantly affected by crack face interaction, which in turn is dependent on the extent of surface roughness of the crack faces. The roughness of the crack faces can be modeled at two levels: micro and macro. Cracks growing in near threshold regime in planar slip materials and coarse-grained materials are likely to have micro-level non-flat surfaces, and the growth behavior of such cracks is influenced by the contact interaction and relative sliding between faces. Micro-level roughness of crack faces can be done using Gaussian or other types of distribution of asperity heights (e.g., ref [25,26]). In this research, the roughness of the crack faces has been modeled at macro-level using Coulomb's friction model. The coefficient of friction, μ , can be treated as a preliminary measure of roughness of crack faces. It is then possible to investigate the effect of friction on crack closure by considering different values of μ . Figure A-13 shows the Mode I and Mode II opening levels for slanted cracks subjected to maximum stress $S_{\max}/\sigma_0 = 0.8$ and two different values of friction coefficient μ : 0.1 and 0.4.

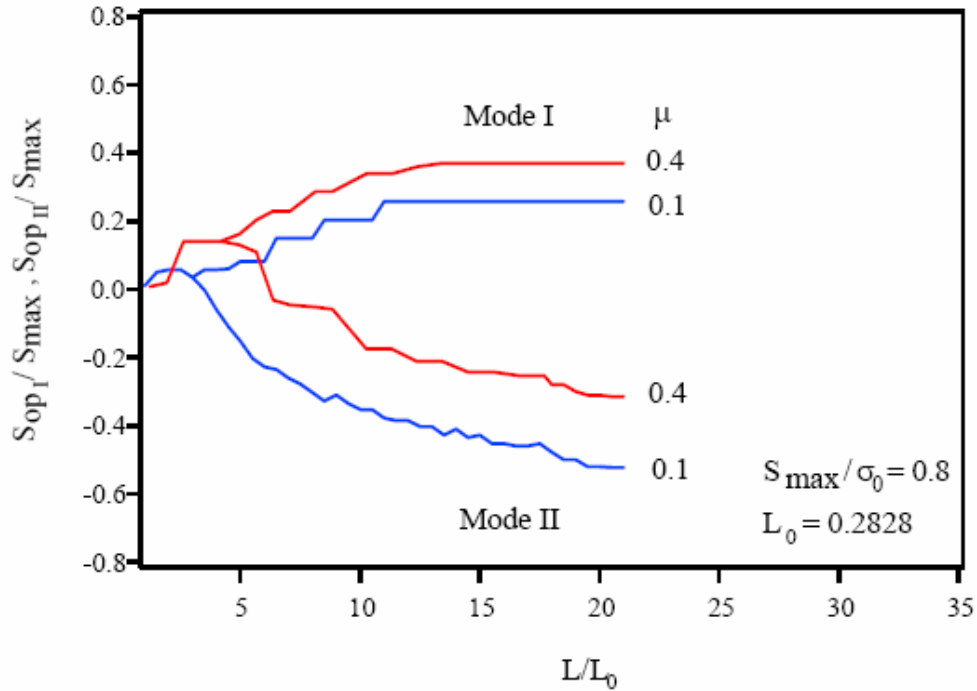


Figure A-13. The effect of friction coefficient on opening levels for a 45° slanted crack, plane stress, $R = -1$. Results show that for lower friction coefficients, the crack opening levels are lower. All lengths are in mm.

For smaller crack lengths, increase in μ has no significant effect on either Mode I or Mode II opening level. However, for $\mu = 0.4$, separation of the Mode I and Mode II S_{op} curves occurs at a larger crack length value. The final stable opening levels are higher for $\mu = 0.4$. The increase in Mode II opening levels is rather expected: increased friction will offer greater resistance to relative sliding between the crack faces, thus requiring higher applied stress to produce complete slip along the crack flanks. Mode I opening, on the other hand, is primarily dependent on the crack tip displacements and the residual deformation in the wake of the crack. Figure A-13 suggests a secondary dependence of Mode I opening on friction between the crack faces. Similar dependence of Mode I opening stress on friction coefficient has been reported by Wei and James [46]. Thus, it is seen that increased friction will lead to an increase in Mode I and Mode II opening levels.

Abbreviations and Acronyms

AAR	Association of American Railroads
CT	compact tension
DOB	degree of bending
DTA	damage tolerance analysis
FE	finite element
FRA	Federal Railroad Administration
NTSB	National Transportation Safety Board
OTR	over-the-road
PICC	plasticity induced crack closure
RICC	roughness induced crack closure
RPI	Rensselaer Polytechnic Institute
RSPA	Research and Special Programs Administration
SENT	single edge notch tension
SIF	stress intensity factor
SMCC	sliding mode crack closure
SwRI	Southwest Research Institute
UIUC	University of Illinois at Urbana-Champaign
VCD	vertical coupler down